OUKA
The University of Osaka
Institutional Knowledge Archive

Title	Structural Features and Design Frameworks for Pneumatic Soft Actuators with Tongue-like Variable Surface Shapes
Author(s)	水野, 海渡
Citation	大阪大学, 2026, 博士論文
Version Type	VoR
URL	https://doi.org/10.18910/105439
rights	
Note	

The University of Osaka Institutional Knowledge Archive : OUKA

https://ir.library.osaka-u.ac.jp/

The University of Osaka

Doctoral Dissertation

Structural Features and Design Frameworks for Pneumatic Soft Actuators with Tongue-like Variable Surface Shapes

Kaito Mizuno

January 2026

Graduate School of Engineering

The University of Osaka

Abstract

Pneumatic soft actuators (PSAs) with variable surface shapes represent a new class of soft actuators that overcome the limitations of conventional PSAs typically restricted to simple deformations such as bending, elongation, or contraction. This type of PSAs that can produce multiple and continuous surface configurations within a single structure achieve higher functional diversity, greatly expanding the capabilities of soft robotic systems. This study aims to identify the fundamental structural features of PSAs with variable surface shapes and to establish a design framework for them. Among the potential applications of such PSAs, one of the most promising is the development of tongue robots for *in vitro* mastication. The human tongue exhibits complex and diverse deformations during mastication. Reproducing these complex tongue motions demands PSAs with variable surface shapes. Conventional forward-problem-based design approaches, in which actuators are constructed by empirically modifying existing structures, rely heavily on the designer's intuition and the tuning of parameters by trial-and-error. Consequently, achieving reproducible PSA designs for multiple and complex deformations is difficult. In contrast, a inverse-problem-based design framework defines the desired surface deformation as the target and inversely derives both the actuator's structure and control inputs necessary to realize it. This approach enables efficient and reproducible design of PSAs with variable surface shapes for *in vitro* mastication simulators, capable of reproducing the complex and dynamically varying tongue-like surface shapes . This dissertation establishes a computational inverse-problem-based design methodology for PSAs with variable surface shapes and applies it to the development of a tongue robot. The proposed framework integrates analytical modeling, finite element analysis (FEA), and Bayesian optimization to inversely determine both a single actuator structure and multiple internal pressure patterns from given target shapes. This unified and computationally efficient process allows exploration high-dimensional design spaces without reliance on empirical parameter tuning. The study begins by constructing a tongue simulator using a single-chamber PSA to clarify limitations of forward-problem-based approach and requirements of actuation and sensing. Next, an analytical model-based optimization method is developed for a pneumatic soft actuator with arrayed chambers (PSA-AC), enabling design of internal pressure patterns to reproduce multiple tongue-like target shapes as a partial inverse-problem-based design approach. Finally, to further enhance the expressive capability of PSAs with variable surface shapes and to enable the inverse-problem-based design of both structure and internal pressure, we propose the PSA-LM. The PSA-LM features a computationally tractable structure that can be geometrically approximated using stacked triangles. A geometric design algorithm is introduced to derive a single membrane structure from target shapes, whereas FEA combined with Bayesian optimization determines optimal pressure patterns under the derived structure. Overall, this research establishes the structural features of PSAs with variable surface shapes and provides a foundation for their systematic design, offering both theoretical and practical advances toward realistic tongue robots for *in vitro* mastication and future soft robotic systems with adaptive morphing capabilities.

Acknowledgments

First and foremost, I would like to express my deepest gratitude to my supervisor, Professor Mitsuru Higashimori, for his tremendous guidance throughout the preparation of this dissertation. From the earliest stages of my research, he respected my interests and consistently provided enthusiastic advice, encouragement, and unwavering support. During the five years I devoted to research under his supervision, I gained invaluable experiences that will remain a lasting foundation in my life going forward.

I am also deeply grateful to Professor Keisuke Morishima and Professor Masato Ishikawa of The University of Osaka for their guidance as sub-advisors of this dissertation. The valuable comments and discussions I received from them advanced the content of this work.

Furthermore, I would like to express my sincere appreciation to Associate Professor Hisashi Ishihara of The University of Osaka, who likewise served as a sub-advisor. Through the guidance I received during our collaborative research when I was a National Institute of Technology student, I gained essential knowledge of research methodology and soft robotics, which formed an indispensable basis for the progress of this study.

I would also like to thank Professor Kazuhiro Hori of Niigata University and the members of the Division of Comprehensive Prosthodontics, Niigata University Graduate School of Medical and Dental Sciences, for their support in our collaborative research. Through our discussions and interactions, they provided valuable insights and opinions that substantiated the medical, dental, and clinical perspectives relevant to the applications of this dissertation.

In addition, I am deeply grateful to Assistant Professor Kazuki Higashi, Dr. Akihide Shibata, and all staff members of the Higashimori Laboratory for their advice on research matters and administrative support.

I also wish to thank the doctoral students, Ms. Hinano Ichikura and Mr. Yuto Miyazaki, as well as all student members of the Higashimori laboratory. Daily discussions and interactions with them were of great help in advancing this research.

I would also like to express my deep gratitude to Lecturer Takumi Kawasetsu of Kyoto University, who provided the opportunity that led to my collaborative research with Associate Professor Ishihara and offered generous support, particularly through extracurricular activities.

Lastly, I would like to express my heartfelt gratitude to my father Hirohisa, mother Akiko, sister Kanon, and to Mirei Seida for understanding my research activities and supporting me continuously. Their presence has been an immense source of strength throughout the completion of this dissertation.

Contents

List of Figures **v**

List of Tables **xi**

Nomenclature **xiii**

1 Introduction **1**
1.1 Background and Motivation 1
1.2 Objective 4
1.3 Dissertation Outline 5
1.4 Related Works 6
1.4.1 Actuators with Variable Surface Shapes 6
1.4.2 Inverse-problem-based Design Method for PSAs 7
1.4.3 *In Vivo* Observation of the Human Tongue 9
1.4.4 Conventional Tongue Robots 10
1.4.5 Implementing Sensing Capability for Soft actuators 11

2 Development of a Single Chamber Pneumatic Soft Actuator with Visuo–tactile Sensing **13**
2.1 Introduction 13
2.2 Proposed PSA 14
2.3 Shape Sensing Method 16
2.4 Basic Experiment 18
2.4.1 Setup for Shape Sensing Experiment 18
2.4.2 Result of Shape Sensing Experiment 18
2.4.3 Setup for Internal-Contact Pressure Characterisation Experiments 19
2.4.4 Results of Internal-Contact Pressure Characterisation Experiments 19
2.5 Sensing and Manipulation of Deformable Objects 20
2.5.1 Surface Shaping for a Deformable Object 21
2.5.2 Estimation of Viscoelasticity 24
2.6 Conclusion 26

3 Pressure Design Method for a Pneumatic Soft Actuator with Arrayed Chambers **27**
3.1 Introduction . . . 27
3.2 Modeling of PSA-AC . . . 28
3.2.1 Chamber Inner Wall Unit . . . 29
3.2.2 Chamber Surface Unit . . . 30
3.2.3 Fitting of the Surface Unit Characteristic Function. . . . 31
3.2.4 Model Considering Contact Forces . . . 32
3.3 Solving For The Internal Pressure Pattern . . . 32
3.4 Experiment . . . 34
3.4.1 Prototyped PSA-AC and Measurement Methods for Surface Shapes 34
3.4.2 Preliminary Experiment . . . 36
3.4.3 Surface Shape Reproduction Experiment . . . 37
3.5 Conclusion . . . 43

4 Novel Pneumatic Soft Actuator Composed of Layered Membranes and Its Design for Structure and Pressure **45**
4.1 Introduction . . . 45
4.2 Design Process . . . 48
4.3 Basic Behavior of Layered Membranes . . . 48
4.4 Structural Design Method . . . 50
4.4.1 Overview of Structural Design . . . 50
4.4.2 First Bottom Line Determination . . . 52
4.4.3 Other Bottom Line Determination . . . 55
4.4.4 Triangle Height Determination . . . 56
4.4.5 Layer Folding . . . 57
4.4.6 Layer Integration . . . 58
4.5 Internal Pressure Design . . . 59
4.5.1 Overview of Pressure Design . . . 59
4.5.2 Initial Internal Pressure Pattern Calculation . . . 60
4.5.3 Bayesian Optimization . . . 61
4.6 PSA-LM Fabrication . . . 62
4.7 Experiment . . . 62
4.7.1 Overview of the Experiment . . . 62
4.7.2 Result of Structural Design for Five Shapes . . . 62
4.7.3 Result of the Internal Pressure Design for Five Shapes . . . 63
4.8 Reproduction of Tongue-like Shapes and Comparison with PSA-AC . . . 68
4.9 Conclusion . . . 73

5 Conclusion **77**
5.1 Summary . . . 77
5.2 Future Works . . . 78

A Pressure Design for PSA-AC Considering Contact Forces **81**
A.1 Introduction 81
A.2 PSA-AC Surface Shape Model with Contact Pressure 81
A.2.1 Modeling of PSA-AC with Contact Pressure 81
A.2.2 Chamber Inner Wall Unit 81
A.2.3 Chamber Surface Unit 83
A.3 Solving Chamber Internal Pressure Pattern 83
A.4 Experiments 83
A.4.1 Experimental Setup 84
A.4.2 Object Tilting Task 84
A.4.3 Actual Internal Pressure Patterns 85
A.4.4 Experimental Results 86
A.5 Conclusion 86

B Estimate Ogden model paremeters **89**

References **91**

Achievements **101**

List of Figures

1.1 Comparison of conventional and novel PSAs with variable surface shape. 2

1.2 Flexible soft organs and details of the varying shape acquired by the human tongue when executing different functions. 3

1.3 Comparison between tongue robot design approaches. 4

1.4 Positioning of this study and related works as PSA. (a–c) Inverse-problem-based design approaches have mainly been applied to PSAs that produce simple deformations such as bending or twisting[51,52,56]. (d–f) Tongue-type PSAs have generally been designed through foward-problem-based approaches, most lacking sensing capabilities and often adapting conventional structures[37,41,43] such as PneuNets. (g, h) Recently, PSA-ACs capable of realizing variable surfaces have attracted attention; they are typically designed through foward-problem-based approaches[47,50]. (i, j) Although inverse-problem-based design approaches have begun to be applied to PSAs with variable surface shapes, no example has yet achieved both large deformation and multiple target shapes simultaneously[62,63]. This study aims to bridge the remaining gap between these research areas. 8

2.1 Basic concept of the PSA, which provides both surface shape sensing and actuation capabilities. 14

2.2 Proposed balloon type PSA. (a) Appearance of the PSA. (b) Cross-sectional view of the PSA. (c) Arrangement of the proposed PSA and camera. 15

2.3 Pneumatic system for proposed PSA. The system consists of a pressure control valve and its self-made control circuit. 16

2.4 Algorithm of the shape sensing process. 17

2.5 Pinhole camera model for surface shape sensing. 17

2.6 Rigid objects to be measured. (a) Convex shapes with a downward protrusion from the 15 (mm) height plane. (b) Flat shapes, as if the radius of the convex part were increased to infinity. 19

2.7 Measurement results. (a) RMSE between the rigid object and measured actuator shapes. (b) Individual measurement result of the flat shape. (c) Individual measurement result of the $R = 40$ (mm) shape. (d) Individual measurement result of the $R = 25$ (mm) shape. (e) Individual measurement result of the $R = 15$ (mm) shape. 20
2.8 Actuator contact pressure characteristics. (a) Contact pressure distribution on the palate of the actuator. (b) Relationship between P_{bi} and P_{bc}. 21
2.9 Overview of experiments on shape manipulation and sensing by the proposed PSA. (a) Shaping manipulation and viscoelastic parameter sensing. (b) Four types of clay used as deformable objects. 21
2.10 Input pressure patterns for shaping. (a) Single-press is defined as a single pressurization operation. (b) Multi-press is defined as multiple repetitions of 1 seconds of pressurization and 1.5 seconds of release. 22
2.11 Changing the shape of a deformable object using single-press shaping. (a) Shape change seen from top and bottom view. (b) Comparing the initial and final shapes of a deformable body. 23
2.12 Surface shaping results. (a) The results of single-press shaping. (b) The results of multi-press shaping. 23
2.13 Viscoelasticity estimation result. (a) Displacement response and the result of the viscoelastic parameter measurement. (b) Measurement results of the spring constants k_1, k_2. (c) Measurement results of the viscosity coefficients η_1, η_2. 25

3.1 Basic concept. (a) Pneumatic soft actuator with arrayed chambers. Pressurizing each chamber changes the surface shape of the actuator. (b) Various target shapes are reproduced by changing the internal pressure patterns. 28
3.2 Configuration of the surface shape model. The model consists of the surface and inner wall units. 29
3.3 Dimensions of each chamber. These are the same for all chambers except for the pressure values. 29
3.4 Proposal surface shape model. (a) Chamber inner wall unit. (b) Chamber surface unit. 30
3.5 Dimensionless approximation κ of h_j for dimensionless quantities ν and ζ. 32
3.6 Deviation between the target surface shape and the proposed model. Obtain the minimum distance between the target surface shape and $\boldsymbol{q}_{w,i}, \boldsymbol{q}_{s,j}$ as the deviation and implement mathematical optimization for minimization. 34
3.7 Prototyped PSA-AC. (a) Appearance of the PSA-AC. (b) Dimensions of each chamber. These are the same for all chambers except for the pressure values. 35

3.8 Experimental setup for measuring the surface shape of the PSA-AC. The surface shape is obtained by horizontally scanning laser displacement sensor with a linear slider. 35

3.9 Preliminary experimental result. (a) Applied internal pressure pattern and PSA-AC surface shape across ten pressurised trials. The light blue bars represent the pressure values applied to each chamber. The red dots and shaded pink regions indicate the mean values of the measured shape and twice the standard deviations (2σ), respectively. (b) Appearance of the actual PSA-AC. 36

3.10 Experimental results of the ellipsoidal shape. (a) Appearance of the actual PSA-AC. (b) Applied internal pressure pattern determined by optimization and comparison of surface shapes. (c) Applied proportional internal pressure pattern and comparison of surface shapes. 39

3.11 Experimental results of the concave shape. (a) Appearance of the actual PSA-AC. (b) Applied internal pressure pattern determined by optimization and comparison of surface shapes. (c) Applied proportional internal pressure pattern and comparison of surface shapes. 40

3.12 Experimental results of the one-sided convex shape. (a) Appearance of the actual PSA-AC. (b) Applied internal pressure pattern determined by optimization and comparison of surface shapes. (c) Applied proportional internal pressure pattern and comparison of surface shapes. 41

3.13 Experimental results of the crevasse shape. (a) Appearance of the actual PSA-AC. (b) Applied internal pressure pattern determined by optimization and comparison of surface shapes. (c) Applied proportional internal pressure pattern and comparison of surface shapes. 42

4.1 Basic concept of the structural feature. (a) Redefining the minimum element of the structure from a rectangular chamber to a membrane. (b) The PSA-LM proposed in this study is a type of soft actuator that can change its shape and easily approximate simple geometric shapes. 46

4.2 Basic concept. (a) PSA-AC design method can only design pressure and uses a uniform structure and target shapes. (b) PSA-LM uses only target shapes and can design both pressure and a unique structure. 47

4.3 Overview of PSA-LM design. After the geometric structural design is complete, the internal pressure pattern design is performed using optimization and analysis models. 48

4.4 Bahavior of layerd membranes. Layered membranes exhibit different deformation behaviors depending on the endpoint connections and whether positive or negative pressure is applied. 49

4.5 Geometrial elements that indicate PSA-LM membrane. (a) Isosceles triangle elements representing the inflated membrane. (b) Line segments representing the folded membrane. 51

4.6 Structure design process. PSA-LM structure was geometrically designed using a triangular approximation of the target shape, folding, and integration. 53
4.7 Structural design examples. (a)(b) Target shapes. (c)(b) Target shapes expressed as stacks of isosceles triangles. (e)(f) Designed folded membrane structures. (g) Integrated membrane structure. (h)(i) Inflated shapes of the integrated membrane structure. 54
4.8 Bottom line determine process on jth layer. (a) Condition 1: Overlap inside the previous layer of the outer shape is prohibited. (b) Contidion 2: Protrusion outside the target shape is prohibited. 56
4.9 Membrane analysis model. The membrane shape is represented with arcs based on Laplace's law. 61
4.10 PSA-LM fabrication processes (a) Step 1: Curing the silicone rubber. (b) Step 2: Remove the chamber mold sheet. (c) Step 3: Seal the ends. . . . 63
4.11 Five target shapes with one to four peaks were selected. (a) Shape i-i. (b) Shape i-ii. (c) Shape i-iii. (d) Shape i-iv. (e) Shape i-v. 64
4.12 Target shapes expressed as triangles. (a) Shape i-i. (b) Shape i-ii. (c) Shape i-iii. (d) Shape i-iv. (e) Shape i-v. 65
4.13 Designed structure. (a) Line segments of folded membrane structure. (b) Actual PSA-LM structure. (c) Appearance of actual PSA-LM. 66
4.14 FEA results with $\boldsymbol{p}_{\text{init}}$ applied. (a) Shape i-i. (b) Shape i-ii. (c) Shape i-iii. (d) Shape i-iv. (e) Shape i-v. 67
4.15 FEA shapes and actual PSA-LM surface shapes when $\boldsymbol{p}_{\text{opt}}$ is applied. (a) Shape i-i. (b) Shape i-ii. (c) Shape i-iii. (d) Shape i-iv. (e) Shape i-v. . . 69
4.16 Appearance of the actual PSA-LM shape when $\boldsymbol{p}_{\text{opt}}$ is applied. (a) Shape i-i. (b) Shape i-ii. (c) Shape i-iii. (d) Shape i-iv. (e) Shape i-v. 70
4.17 Target shapes for the human tongue. (a) Shape ii-i: ellipsoidal shape. (b) Shape ii-ii: concave shape. (c) Shape ii-iii: one-sided convex shape. (d) Shape ii-iv: crevasse shape. (e-h) Shape ii-v, ii-vi, ii-vii , ii-viii: shapes with twice the maximum height of the previous four shapes. 71
4.18 Actuator structures and chamber/membrane indices for reproducing tongue-like shapes. (a) PSA-AC structure used in Chapter 3. (b) PSA-LM structure that automatically designed by the method in this chapter. . . 72
4.19 RMSEs of the methods in Chapter 3 and 4. 73
4.20 Comparison of target and FEA shapes. (a) Shape ii-i. (b) Shape ii-ii. (c) Shape ii-iii. (d) Shape ii-iv. (e) Shape ii-v. (f) Shape ii-vi. (g) Shape ii-vii. (h) Shape ii-viii. 74
4.21 Strain distribution of (a) PSA-AC and (b) PSA-LM in Shape ii-v. . . . 75

A.1 Configuration of the surface shape model. The model consists of the surface unit and the inner wall unit. The pressure distribution is applied to the model assuming contact with the objects. 82
A.2 Proposal surface shape model. (a) Chamber inner wall displacement unit. (b) Chamber surface displacement unit. 82

A.3 Overview of the tilting task. 84
A.4 Dimensions of each chamber. These are the same for all chambers except for the pressure values. 84
A.5 Experimental setup. (a) Pneumatic system for the actuator drive. (b) Object to be manipulated. 85
A.6 The target shape and applied pressure distribution for the tilting task. . 85
A.7 Pressure conditions and model shapes. (a) Without contact pressure consideration. (b) With contact pressure consideration. 86
A.8 Experimental results. (a) Without contact pressure consideration. (b) With contact pressure consideration. 87

B.1 Ogden model plot for DragonSkin 10 NV. 90

List of Tables

3.1 Parameters of the surface unit characteristic function 32

4.1 Initial internal pressure pattern $\boldsymbol{p}_{\text{init}}$ values. 68
4.2 Optimized internal pressure pattern $\boldsymbol{p}_{\text{opt}}$ values. 68
4.3 Internal pressure values for PSA-AC. 72
4.4 Internal pressure values for PSA-LM. 72

Nomenclature

α	Correction factor for visuo tactile sensor
η_1	Viscosity coefficients of the Burgers model
η_2	Viscosity coefficients of the Burgers model
F	Focal length on the pinhole camera model
H	Height of the silicone rubber membrane from the optical center
k_1	Spring constants of the Burgers model
k_2	Spring constants of the Burgers model
P_{bc}	Contact pressure of silicone rubber membrane
P_{bi}	Internal pressure of silicone rubber membrane
R_i	Radius of the i th black PLA resin ring embedded for visuo tactile sensor
r_i	Radius of i th ring embedded for visuo tactile sensor
z_i	z-displacement of the i th ring
β	The displacement correction factor of the PSA-AC model
$\boldsymbol{F}_{w,i}$	Virtual forces applied to linear elastic elements of PSA-AC chamber inner wall unit
$\boldsymbol{p}$	Internal pressure vector for PSA-AC chambers
$\boldsymbol{P}_c$	Contact pressure distribution on PSA-AC
$\boldsymbol{q}_{s,j}$	Position vector of the j th surface node in the PSA-AC model
$\boldsymbol{q}_{s0,j}$	The position of the j th surface node of the PSA-AC model before adding $F_{s,j}$
$\boldsymbol{q}_{w,i}$	Position vector of the i th inner wall node in the PSA-AC model

NOMENCLATURE

$\boldsymbol{q}_{w0,i}$	The position of the i th inner wall node of the PSA-AC model before deformation
E	Young's modulus of elasticity for the silicone rubber
$F_{s,j}$	Virtual forces applied to linear elastic elements of PSA-AC chamber surface unit
$H(q_{sx0,i})$	Height in the target shape at initial horizontal position of PSA-AC surface node
$h_j^{'}$	Approximated displacement of the surface node in the direction parallel to $F_{s,j}$ in the PSA-AC chamber surface unit
h_j	Displacement of the surface node in the direction parallel to $F_{s,j}$ in the PSA-AC chamber surface unit
$H_{\max}$	Maximum height in the target shape
k_s	Spring constant of linear elastic elements in PSA-AC chamber surface unit
k_w	Spring constant of linear elastic elements in PSA-AC chamber inner wall unit
l_d	Chamber depth length of PSA-AC
l_s	Distance between the PSA-AC chamber inner walls
l_w	Distance from the bottom edge of the PSA-AC chamber to the center of the chamber's surface
$P_{\max}$	Maximum internal line pressure value of PSA-AC
P_{prop}	Internal line pressure of PSA-AC determined in proportion to the height of the target shape
P_i	Internal linear pressure of the i th PSA-AC chamber
t_s	Thickness of the PSA-AC chamber surface
t_w	Thickness of the PSA-AC chamber's inner walls
$g(\zeta, \nu)$	Surface unit characteristic function in the PSA-AC model
κ	Non-dimensionalized Displacement of the surface node in the direction parallel to $F_{s,j}$ in the PSA-AC chamber surface unit
ν	Non-dimensionalized pre-stretched length of the linear elastic element before deformation in the PSA-AC chamber surface unit

ξ	Non-dimensionalized length of the linear elastic element after deformation in the PSA-AC chamber surface unit
ζ	Non-dimensionalized internal pressure in the PSA-AC chamber surface unit
a_{mn}	Parameters of the surface unit characteristic function $g(\zeta, \nu)$
$\boldsymbol{\Theta}$	Error between the PSA-AC model and the target surface shape
$\boldsymbol{\theta}_{\text{model}}$	PSA-AC model outline point cloud
$\boldsymbol{\theta}_{\text{target}}$	Point cloud corresponding to each PSA-AC model node in the target shape
$\boldsymbol{q}_{\text{target,k}}$	Coordinates of the point corresponding to the k th PSA-AC model node in the target shape point cloud
S	Sum of squares of $\boldsymbol{\Theta}$
$\boldsymbol{I}$	Unit matrix
$\boldsymbol{J}$	Jacobi matrix of $\boldsymbol{\Theta}$
δ	Damping factor of LM method
f	Scaling factor of LM method
$\boldsymbol{m}_{\text{center},i,j,k}$	Position vector of the vertex of $\boldsymbol{m}_{i,j,k}$
$\boldsymbol{m}_{\text{left},i,j,k}$	Position vector of the point on the left side of the bottom line of $\boldsymbol{m}_{i,j,k}$
$\boldsymbol{m}_{\text{right},i,j,k}$	Position vector of the point on the right side of the bottom line of $\boldsymbol{m}_{i,j,k}$
$\boldsymbol{q}_{concave,n}$	n th concave point on the target shape
$\boldsymbol{q}_{cross,i,k}$	Intersection point between the perpendicular line extending from the midpoint of the k th bottom line and target shape i
$\hat{\boldsymbol{m}}_{\text{center},i,j,k}$	Position vector of the center point in the line segment of $\hat{\boldsymbol{m}}_{i,j,k}$
$\hat{\boldsymbol{m}}_{\text{left},i,j,k}$	Position vector of the left point in the line segment of $\hat{\boldsymbol{m}}_{i,j,k}$
$\hat{\boldsymbol{m}}_{\text{right},i,j,k}$	Position vector of the right point in the line segment of $\hat{\boldsymbol{m}}_{i,j,k}$
$\hat{\mathcal{M}}_{\text{int}}$	Integrated folded membrane shape of PSA-LM
$\hat{\mathcal{M}}_i$	Folded membrane shape of PSA-LM for target shape i
$\hat{\mathcal{R}}_{i,j}$	Set of points arranged on the same straight line by folding $\mathcal{R}_{i,j}$
$\hat{m}_{\text{int},j,k}$	k th line segment on j th layer on PSA-LM integrated folded membrane structure

NOMENCLATURE

$\hat{\boldsymbol{m}}_{i,j,k}$	k th line segment on j th layer for target shape i on PSA-LM folded membrane structure
$\mathcal{M}_{\text{int}}$	Integrated inflated membrane shape of PSA-LM
$\mathcal{M}_i$	Inflated membrane shape of PSA-LM for target shape i
$\mathcal{Q}_{\text{FEA}}$	Inflated PSA-LM shape on FEA
$\mathcal{Q}_i$	Target shape for PSA-LM
$\mathcal{R}_{i,j}$	Polygon representing the outer shape of the j th layer in PSA-LM inflated membrane shape for the target shape i
$\boldsymbol{m}_{\text{int},j,k}$	k th triangle element on j th layer on PSA-LM integrated inflated membrane structure
$\boldsymbol{m}_{i,j,k}$	k th isosceles triangular elements on j th layer for target shape i on PSA-LM inflated membrane structure
$h_{i,j,k}$	Height of the trianglular element$\boldsymbol{m}_{i,j,k}$
$hq_{i,n}$	Distance between the bottom line and $\boldsymbol{q}_{cross,i,k}$
$l_{i,j,k}$	Bottom line length of the trianglular element$\boldsymbol{m}_{i,j,k}$
t_m	Membrane thickness in PSA-LM
$\boldsymbol{p}_{\text{init}}$	Initial internal pressure pattern for PSA-LM
$\boldsymbol{p}_{\text{opt}}$	Optimized internal pressure pattern for PSA-LM
γ_i	Material constants in the Ogden model
λ	Stretch ratio
μ_i	Material constants in the Ogden model
ϕ	Angle of the arc in the membrane analysis model
ρ_0	Half the initial membrane width
ρ_1	Radius of the arc in the membrane analysis model
σ	Nonlinear stress of elastic membrane
τ_0	Initial membrane thickness
τ_1	Membrane thickness after elongation
υ	Center displacement of the membrane analysis model
ε_0	Prestretch ratio of the membrane
ε_1	Elongation ratio of the membrane

Chapter 1

Introduction

1.1 Background and Motivation

Identifying structural features that enable active generation of complex and diverse surface shapes and developing soft actuators that exploit the deformability of soft materials has great potential to advance soft robotics. Soft actuators are typically composed of flexible, stretchable materials such as silicone rubber and gels[1–4]. Among them, pneumatic soft actuators (PSAs) which are driven by compressed air, have become the mainstream in current soft robotics due to their ease of implementation, low cost, and responsiveness[5–7]. Representative examples include PneuNets[8,9] and artificial muscles[10–13] which generally share certain common structural characteristics achieve simple active deformations such as bending, twisting, elongation, or contraction as well as passive deformation through external contact, as shown in the left side of Fig. 1.1. These PSAs have enabled applications ranging from grippers for fragile objects to wearable devices and medical tools. However, soft materials inherently possess nearly infinite degrees of freedom. Through refined structural design and input control, they have the potential to generate far more complex and diverse surface shapes, as shown in the right side of Fig. 1.1. Clarifying the basic structure that enables active deformation from a single initial state into diverse surface shapes would lead to a new class of PSAs with variable surface shapes, capable of advanced and complex deformation while preserving softness. This is expected to further expand the applications of soft robotics.

One of the most promising applications of PSAs with variable surface shapes is the development of *in vitro* soft organ simulators. Biological organs such as the tongue, stomach, and esophagus are composed of flexible tissues, including muscles, and perform various functions such as transporting and mixing food and liquids through complex deformations[14–25] as shown in Fig. 1.2. Soft robots are well suited for *in vitro* organ simulators because of their flexibility. This approach enables controlled experimental environments and noninvasive observations that are difficult to achieve *in vivo*, thereby facilitating the study of biological functions. Indeed, soft robots have already been applied to reproducing organs such as the stomach and esophagus[26–31].

Among these organs, reproducing the tongue *in vitro* is particularly challenging,

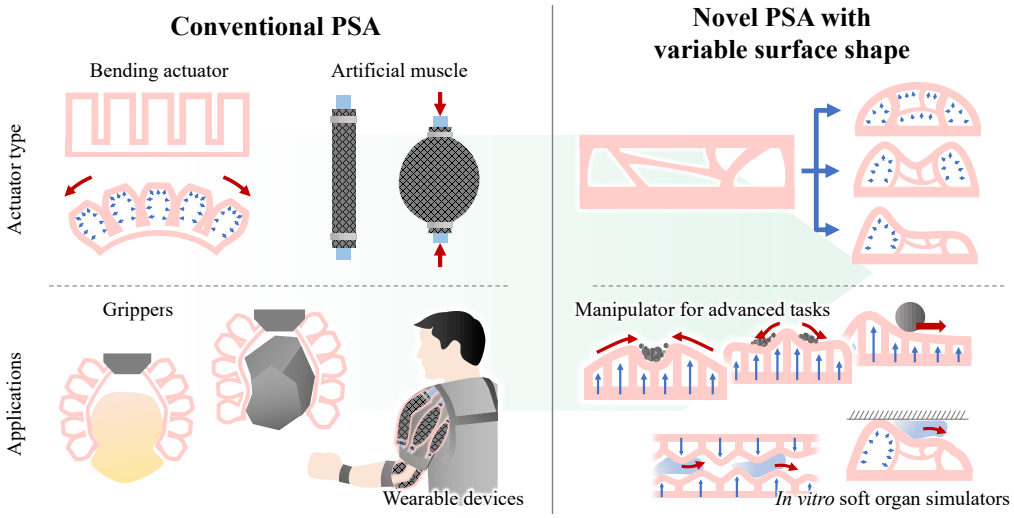


Figure 1.1: Comparison of conventional and novel PSAs with variable surface shape.

making the establishment of an appropriate design methodology highly desirable. The tongue performs a wide range of functions, including mastication, swallowing, and articulation, and its surface deformations more complex and diverse than those of other organs. During mastication, for example, the tongue executes intricate motions such as breaking, mixing, compressing, and transporting food through its shape changes. Understanding the mechanisms of mastication has considerable social significance in aging societies, particularly for oral rehabilitation and the development of nursing care foods. Masticatory behavior varies depending on food properties and individual habits, resulting in diverse of tongue shapes. Therefore, to develop tongue robots capable of reproducing individualized tongue motions, an efficient design process is required to explore optimal structural parameters and control inputs. For PSAs with variable surface shapes, which serve as the core of this process, establishing a suitable design methodology is essential.

Previous studies on PSAs can be broadly classified into two design approaches . The first is the foward-problem-based design approach, in which actuators are developed by adjusting and combining existing structures and technologies for specific applications. In this approach, known mechanisms and techniques are used as design inputs, which are then empirically modified and tuned through trial and error. In the context of tongue robots, this corresponds to constructing PSAs by combining existing structures such as PneuNets, tuning their parameters, and adjusting control inputs while observing the resulting motions to reproduce target tongue behaviors[32–50] as shown in the lower part of Fig. 1.3. Although this method allows relatively straightforward construction, the resulting performance is often suboptimal and heavuly dependent on the original structure as well as the designer's experience and intuition.

The second approach is the inverse-problem-based design methodology, in which

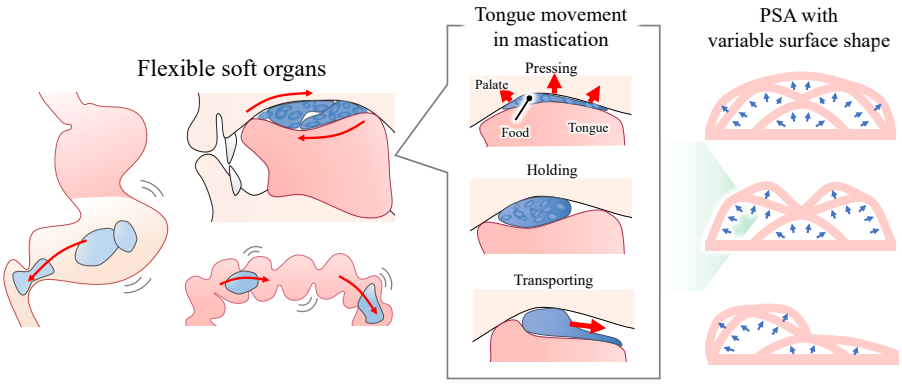


Figure 1.2: Flexible soft organs and details of the varying shape acquired by the human tongue when executing different functions.

desired states—such as actuator shape or motion—are predefined as targets, and the necessary structural and control parameters are inversely derived to achieve them. For tongue robots, this corresponds to computationally deriving PSA structures and control inputs capable of reproducing target tongue behaviors, using measured human tongue shape and motion data as design inputs as shown in the upper part of Fig. 1.3. In recent years, inverse-problem-based design approaches have been actively studied in bending-type PSAs for robotic grippers particularly[51–60]. This trend has been facilitated by advances in finite element analysis (FEA), increased computational power, and sophisticated optimization methods. Several studies have attempted to apply inverse-problem-based design to PSAs with variable surface shapes[61–63]. However, these results remain limited, as the actuators are often reproduce only a single surface shape or exhibit relatively small deformations. For PSAs with variable surface shapes, complex curved surfaces must be generated as outputs. Directly applying conventional inverse-problem-based methods results in extremely high computational costs, making iterative optimization inefficient. Furthermore, PSAs with variable surface shapes lack established structural design guidelines, and related techniques have not yet reached sufficient maturity. In particular, the structural principles required to generate multiple surface shapes with large deformations using a single PSA have not been clearly established, and the systematic organization of design variables remains underdeveloped.

In the development of tongue robots for *in vitro* mastication, the inverse-problem-based design approach can serve as a theoretical framework for optimal design, reflecting both intended applications and individual variations. However, due to the challenges outlined above, this approach has not yet become widespread. Conventional tongue robots were mainly designed using a foward-problem-based approach Representative examples include systems that combine rigid mechanisms such as robotic cylinders[36] or wire-driven actuators with flexible skins[32,37], adaptations of PSAs originally developed for robotic grippers[39–43], and bioinspired designs replicating the muscle arrangement of the human tongue[46]. Morever, while many foward-problem-based studies have fo-

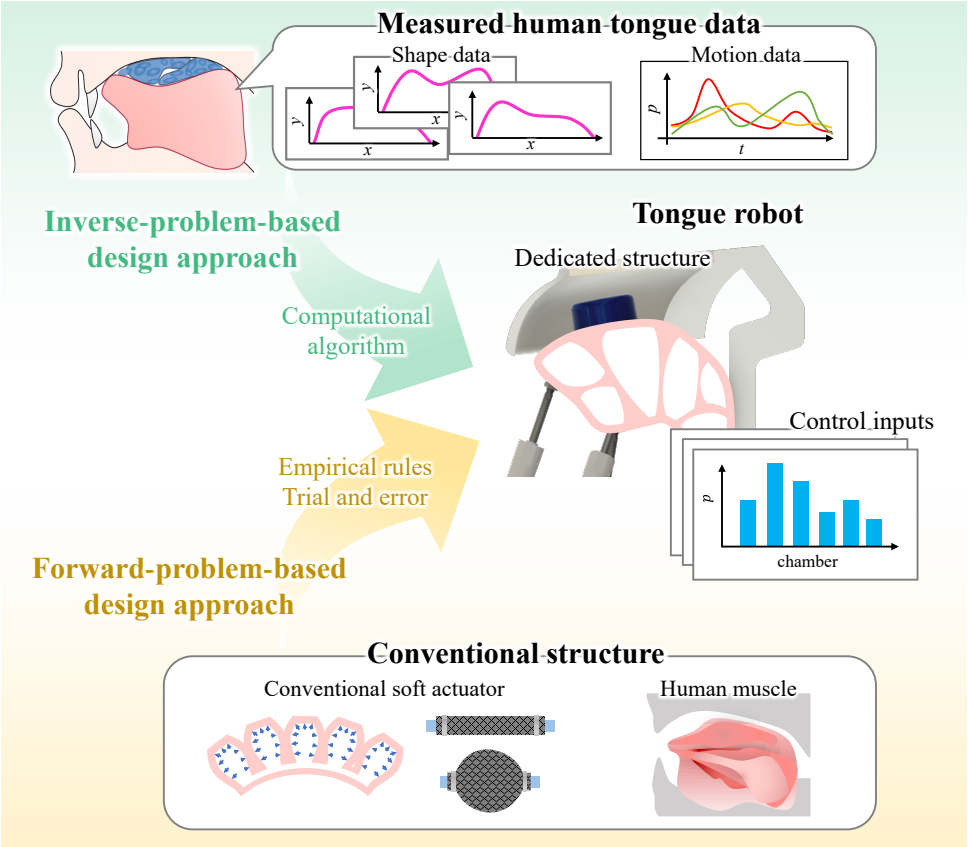


Figure 1.3: Comparison between tongue robot design approaches.

cused on actuation capabilities, the implementation of sensing functions necessary for manipulation remains underdeveloped.

Therefore, to realize PSAs with variable surface shapes and apply them to tongue robots, it is essential to develop actuator structures that can efficiently generate the desired surface shapes while remaining computationally tractable, and construct a inverse-problem-based design algorithm capable of determining both the structure and internal pressure patterns required to reproduce target shapes under its structural constraints.

1.2 Objective

The objective of this dissertation is to identify a novel actuator structure that enables the realization of a PSA with variable surface shapes and to establish a computational inverse-problem-based design methodology applicable to such actuators. The tongue robot for *in vitro* mastication is considered a representative application in which the characteristics of this type of PSA can be most effectively utilized, and the research is conducted with this application in mind. First, based on the conventional

foward-problem-based approach, the requirements for tongue robots are clarified, and the limitations of this approach are identified. At the same time, sensing capabilities—previously insufficiently in tongue robots—are newly introduced. Furthermore, to establish a inverse-problem-based design approach for PSAs with variable surface shape, a fundamental structure capable of reproducing multiple target shapes within a single actuator is proposed. Under this structural framework, inverse design algorithms are developed for both the actuator's geometry and the internal pressure patterns required to reproduce the target shapes.

1.3 Dissertation Outline

This dissertation is organized as follows:

Chapter 1 summarizes the research background and motivation situates this study within the context of related work.

Chapter 2 discusses a tongue robot for *in vitro* mastication simulator consists of single-chamber PSA equipped with visuo-tactile sensor. This PSA is designed by forward-problem-based approach. Flexible objects, assumed to represent food boluses, are manipulated to simulate shaping during mastication. In addition, the implementation of sensing functions—previously insufficient in conventional tongue robots—is examined. By embedding visuo-tactile sensors, a configuration that achieves both actuation and sensing is proposed. Through this system, the effectiveness of sensing capabilities is demonstrated, and the essential requirements and practical applications of tongue robots are clarified. These investigations highlighted the limitations of single-chamber PSA—which can achieve only simple active deformations—and of forward-problem-based design approaches.

Chapter 3 represents the first stage of the inverse-problem-based design methodology for PSAs with variable surface shapes, focusing on the design of internal pressure patterns for a pneumatic soft actuator with arrayed chambers (PSA-AC) . The PSA-AC employs a uniform structure obtained through forward-problem-based design, while its internal pressure patterns are determined using an inverse-problem-based design approach. An analytical model is constructed by linking linear elastic elements to represent the relationship between internal pressure and surface deformation. Using this model, an optimization-based method is proposed to determine internal pressure patterns from given target shapes, thereby establishing a partial inverse-problem-based design approach. Experiments are conducted using actual PSA-ACs to reproduce representative tongue-like target shapes. These experiments verify the effectiveness of the proposed method and clarify the limitations of the partial inverse-problem-based approach, in which only pressure patterns are designed under a fixed structure.

Chapter 4 introduces a novel pneumatic soft actuator composed of layered membranes (PSA-LM), designed to provide a foundation for applying the inverse-problem-based design methodology to both structure and pressure. The PSA-LM structure can be easily approximated geometrically, facilitating the application of computational design methods. Leveraging this property, an algorithm is introduced to design both the

inflated and folded membrane structures directly from target shapes through a geometric process. Furthermore, a method is presented that determines the optimal internal pressure pattern by combining analytical modeling, finite element analysis (FEA), and Bayesian optimization for the designed structures. Through these methods, a complete inverse-problem-based design framework is realized, enabling simultaneous structural and pressure pattern design of PSAs with variable surface shapes.

Chapter 5 presents the conclusions of this dissertation and outlines directions for future work.

1.4 Related Works

1.4.1 Actuators with Variable Surface Shapes

Actuators capable of generating variable surface shapes have been actively studied for applications such as three-dimentional displays and haptic feedback systems. Jang et al. developed an actuator enclosing PVC gel and a dielectric liquid, in which surface shape changes are achieved by applying high voltage, causing the dielectric liquid to expand, contract, and move[64]. Wang et al. introduced a sheet-type actuator composed of stacked conductive polymer and ion-conductive films, demonstrating that its surface shape can be varied according to the applied voltage pattern[65]. Bai et al. proposed a sheet-type actuator consisting of a flexible composite membrane with serpentine conductive patterns; by applying an electric current through the pattern in a magnetic field, the actuator can deform its surface shape[66]. Ni et al. developed a flexible actuator by embedding a fine liquid-metal microchannel network within a thin elastomer substrate. This actuator can be deformed from a flat plane into arbitrary three-dimensional shapes by driving the liquid metal using electric current and magnetic fields[67]. Despite these advances, such actuators face limitations for practical use, as they require specialized materials and large scale driving systems capable of producing high voltages or strong magnetic fields.

Other actuators have been proposed that arrange linear actuators in a matrix configuration, driving them individually up and down to generate voxel-like surface shapes. Matthew et al. achieved surface shape variation by arranging linear PSAs in an array, applying this mechanism to haptic presentation and object manipulation[68]. Iwata et al. arranged screw-driven linear actuators to realize a three-dimensional display device by deforming the surface shape of a connected projection screen[69]. These actuators offer a high degree of freedom in surface shape representation due to their large number of channels. However, improving shape resolution requires a vast number of actuators, which increases structural complexity and reduces flexibility.

Many previously developed PSAs with variable surface shapes achieve deformation by arranging multiple bubbles and controlling their inflation. Mollaee et al. proposed a bubble-array PSA designed for use inside a prosthetic socket[70], with the purpose of reducing the user load by adaptively changing the inner surface shape according to the condition of the residual limb. Mosadegh et al. introduced a PSA composed of an array

of 32 bubbles, capable of changing its surface shape and transporting objects across its surface by switching inflation patterns[71]. These PSAs offer high flexibility and can achieve relatively large deformations due to their fundamental working principle. However, because each bubble inflates independently, the continuity of the generated surface shape tends to be low.

Several PSAs capable of generating complex and smooth surface shapes have also been developed. Pikul et al. created a membrane-type PSA with a displacement constraint layer made of nonwoven fabric, capable of reproducing a single complex shape resembling a plant or rock[63]. Sakuma et al. developed a PSA capable of reproducing asymmetric three-dimensional shapes using a multilayer inflatable structure formed by bonding thin films together[72]. The displacement constraint layer is made of nonwoven fabric and designed based on a target shape. Ding et al. and Li-Ke et al. proposed pneumatically driven three-dimentional objects in which embedded rigid components are used to control surface shape[61,62]. However, the former designs can express only a single shape, while the latter are incapable of large deformation and both suffer from significantly reduced flexibility due to the embedded rigid parts. To date, no actuator has been realized that combines the flexibility required for tongue robots with the ability to generate multiple smooth, large-deformation, complex surface shapes.

1.4.2 Inverse-problem-based Design Method for PSAs

In recent years, numerous inverse-problem-based computational design methods for PSAs have been proposed[4]. The most common case involves deriving the design parameters of a bending actuator required to achieve a specified target curvature[51–54] as shown in the upper left side of Fig. 1.4. In these studies, the error between actuator deformation and the target posture is evaluated using FEA, and the results are combined with computational algorithms such as genetic algorithms or numerical optimization to derive optimal design parameters. Dong et al. and Pu et al. focused on PSAs consisting of flexible tubes and external shells, developing FEA-based automatic design methods for shell geometry and internal pressure to reproduce target curvature[55,56]. Loïc et al. described internal chamber shapes using Bézier curves and proposed a design method in which both chamber geometry and internal pressure are optimized through a combination of a CNN-based FEA surrogate model and a genetic algorithm[57]. Other methods have been developed to determine optimal structures for achieving target shapes through topology optimization, taking into account surrounding environments and interacting objects[58–60]. Most of these studies have focused on actuators whose deformation states can be relatively easily described in terms of curvature or angle.

By contrast, the application of inverse-problem-based design approaches to PSAs with variable surface shapes shown in the upper right side of Fig. 1.4, remains limited, primarily because their deformation states are complex to describe. Ding et al. developed a method that determines the shape of embedded constraint components and internal pressure inputs by evaluating the pressurized three-dimentional shape using FEA and performing nonlinear optimization so that the resulting shape matches the target[61,62]. Pikul et al. proposed a design method that inversely calculates the

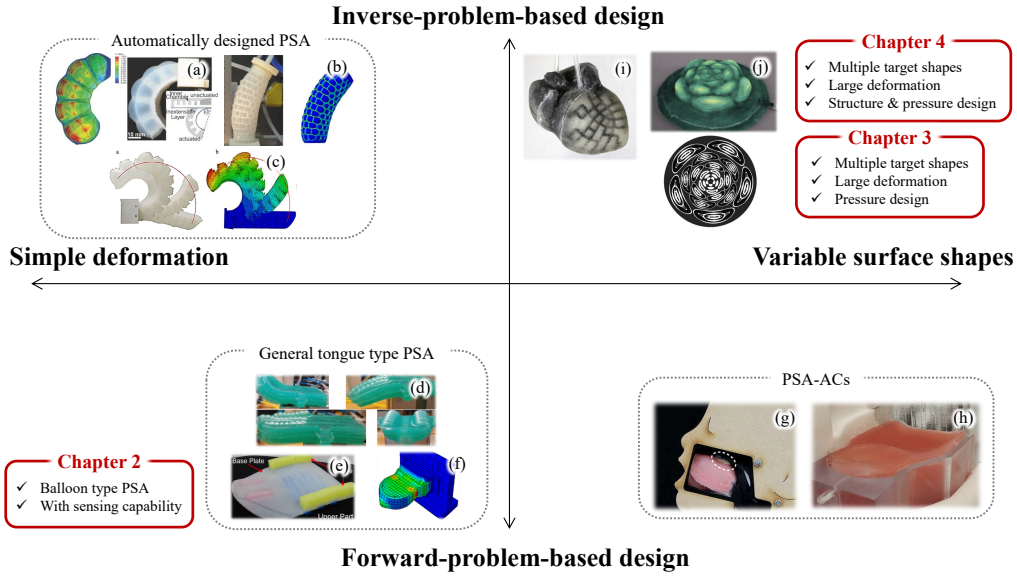


Figure 1.4: Positioning of this study and related works as PSA. (a–c) Inverse-problem-based design approaches have mainly been applied to PSAs that produce simple deformations such as bending or twisting[51,52,56]. (d–f) Tongue-type PSAs have generally been designed through foward-problem-based approaches, most lacking sensing capabilities and often adapting conventional structures[37,41,43] such as PneuNets. (g, h) Recently, PSA-ACs capable of realizing variable surfaces have attracted attention; they are typically designed through foward-problem-based approaches[47,50]. (i, j) Although inverse-problem-based design approaches have begun to be applied to PSAs with variable surface shapes, no example has yet achieved both large deformation and multiple target shapes simultaneously[62,63]. This study aims to bridge the remaining gap between these research areas.

required strain distribution from a target shape and designs shape constraint mesh layer and internal pressure according to the obtained strain ratio[63]. In these studies, PSAs capable of reproducing complex curved surfaces are designed by deriving the geometry of embedded constraint components from the target shape through a inverse-problem-based approach. However, these methods cannot design actuators capable of large deformation or multiple target shapes. The current design process for PSAs with variable surface shapes that can express multiple configurations, such as those required for tongue robots, remains limited to verifying deformations through FEA and making empirical adjustments[40,48].

Metamaterials represent one of the fields where automatic design methods have been most actively applied[73,74]. This is because the fundamental unit elements of metamaterials are clearly defined and computationally tractable. Similarly, in the case of PSAs with variable shapes, if their minimum structural elements can be systematically defined, it is expected that inverse-problem-based automatic design approaches could also be effectively applied.

1.4.3 *In Vivo* Observation of the Human Tongue

Mastication and swallowing are dynamic processes that occur within the closed space of the oral cavity, making direct observation difficult. Consequently, previous studies have employed a variety of experimental methods and *in vivo* measurement techniques to investigate these phenomena. Malek et al. visually observed tongue motion during mastication through gaps between teeth, with the cooperation of patients who had missing teeth[14]. Their study revealed that the tongue plays multiple roles throughout mastication. For example, it forms a concavity to hold the food bolus, quickly shifts the bolus to one side to place food on the teeth, and coordinates with cheek movements to sort food boluses of different sizes. These findings clearly indicate that reproducing a wide variety of tongue-like surface shapes is essential for an *in vitro* mastication simulator. Palmer et al. quantitatively investigated the temporal and spatial relationships between tongue and jaw movements using videofluorography[15]. Five lead markers were attached to the tongue surface as radiopaque reference points, and their motion was tracked to analyze tongue kinematics during mastication. The results showed that tongue movements exhibited a certain degree of periodicity and gradually transitioned from primarily vertical motion to predominantly anterior-posterior motion as mastication progressed. Hori and Ono's research group developed a flexible sensor sheet for measuring tongue pressure[75] and used it to analyze tongue behavior during mastication and swallowing[16–21]. They further conducted combined measurements using this sensor sheet and electromagnetic articulography (EMA)[22], enabling simultaneous recording of tongue pressure and motion data[23,24]. Through multiple experiments with different subjects and target materials, they aimed to identify tongue motion patterns consistently observed across conditions. These methods provide the significant advantage of enabling direct and quantitative measurement of tongue movements during mastication. However, the presence of attached markers and sensors can cause discomfort or mechanical interference potentially affecting natural mastication behavior and limiting the number of measurement points. Imai et al. conducted noninvasive observations without X-ray imaging, employing ultrasonography to measure tongue shapes[25]. By observing cross-sectional profiles of the tongue dorsum, they revealed that mastication proceeds through two alternating phases: one in which uncrushed food is selected and guided between the teeth, and another in which crushed food is mixed with saliva to form a bolus. However, ultrasonography can only capture cross-sectional profiles and cannot obtain full three-dimensional shapes. Although these *in vivo* observations provide only fragmentary information, they hilighted the wide diversity of tongue motions and surface shapes. Considering the difficulty of applying such measurements to large numbers of subjects and the burden placed on patients, an mastication simulator that enables detailed *in vitro* observation of the tongue and foods behavior has a significant advantages.

1.4.4 Conventional Tongue Robots

Early tongue robots were primarily constructed by combining rigid mechanisms such as linear cylinders and linkage systems with an overlaid flexible skin. Kawamura et al. proposed a tongue robot that integrates multiple mechanisms, including a biaxial gimbal structure, hinge mechanisms for shape change, and a wire-driven continuum manipulator[32]. Fukui et al. developed the Waseda Talker series, which reproduces tongue surface shapes during speech by driving a flexible sheet with a linkage mechanism, aiming to generate artificial speech[33–35]. Osuka et al. proposed a method to reproduce both active and passive tongue deformations by combining a linkage mechanism driven by air cylinders with triangular elements filled with polymer gel[36]. However, these approaches lacked sufficient mechanical compliance and were inadequate for reproducing the inherent flexibility of the human tongue.

Subsequently, in pursuit of greater compliance, researchers increasingly explored the use of soft actuators composed of flexible materials as shown in the lower left side of Fig. 1.4. Shijo et al. developed a tendon-driven tongue actuator using a flexible sheet, designed for communication robots[37]. Endo et al. created a tongue type-actuator capable of both contraction and lateral bending[38] using thin McKibben artificial muscles[13]. Xuanming et al., Evan et al., and Selena et al. extended the widely used PneuNets[8,9] into flexible sheet-based configurations and successfully reproduced basic motions such as bending and twisting[39–43]. A study using actual biological tissues has also been reported[44]. Nevertheless, these tongue robots are essentially variants of bending actuators commonly used in robotic grippers, and their fundamental motions remain limited to simple bending and twisting. Moreover, issues such as the visible surface deformation caused by chamber expansion hinder the reproduction of the smooth surface shape required for tongue robots. Sawada et al. and Ishikawa et al. successfully reproduced several representative tongue shapes by arranging flexible contraction-type actuators, such as bellows-type PSAs and thin McKibben artificial muscles[13], to mimic the muscle structure of the human tongue[45,46]. Although these designs enable a certain degree of shape control and constructive understanding of tongue muscle movement, generating sufficient surface pressure required for mastication remains challenging.

In contrast, recent studies have proposed a novel approach that directly links chamber inflation to a transformation of the surface shape. A representative example is PSA-AC, shown in the lower right side of Fig. 1.4. PSA-ACs can simultaneously achieve smooth and dynamic surface shape changes while efficiently generating the contact pressures required for mastication and swallowing. Marco et al. developed an swallowing simulator equipped with a palate and a tongue-shaped PSA-AC consisting of two to three chambers, successfully reproducing and observing the swallowing process *in vitro*[47–49]. Dai et al. developed a compact tongue robot by combining a four-chamber PSA-AC with a bending-type PSA at the base, reproducing tongue behaviors observed in infants[50]. PSA-ACs have emerged as a leading design paradigm for tongue robots due to these advantages. However, in terms of design, while their overall dimensions are roughly modeled after the human tongue, the determination of structural parameters and control inputs still relies heavily on empirical knowledge and trial-and-error adjust-

ments rather than a systematic inverse-problem-based design process. As a result, the optimality of actuator design remains an unresolved issue.

1.4.5 Implementing Sensing Capability for Soft actuators

Implementing shape-sensing capabilities in PSAs with variable surface shapes is essential for applications such as flexible organ simulators and robotic manipulation. By obtaining information about the actuator's own shape, it becomes possible not only to improve motion accuracy but also to indirectly estimate object geometry and contact forces. Several studies have reported the integration of sensing capabilities into soft actuators. For example, actuators that sense their own deflection using embedded optical fibers have been developed[76]. However, the inclusion of optical fibers significantly reduces flexibility, making them unsuitable for PSAs that require large-area surface stretches. Bubble-type PSAs designed for haptic devices with tactile presentation maintain flexibility in the contact area while enabling contact sensing[77,78]. Nevertheless, these actuators are limited to detecting single points of contact or height and cannot measure the detailed shape of an object.

Visuo-tactile sensors are considered particularly suitable for shape sensing in soft actuators. These sensors indirectly estimate the shape and force distribution of an object by capturing deformation of the flexible contact layer using a camera. Common visuo-tactile sensors include FingerVision[79], which tracks dot markers with a camera; GelSight[80], which reads contact shapes from the unevenness of a reflective film; and Punyo[81,82], which employs a depth camera to directly measure thin-film deformation. By applying such sensing technologies to soft actuator, it is expected that both actuation and advanced shape sensing can be achieved while preserving the actuator's inherent flexibility.

Chapter 2

Development of a Single Chamber Pneumatic Soft Actuator with Visuo–tactile Sensing

2.1 Introduction

In this chapter, as a preliminary step toward realizing a pneumatic soft actuator (PSA) with variable surface shapes, we construct a single-chamber PSA with the simplest structure using a forward-problem-based approach and assess its fundamental capabilities. This actuator can actively generate only inflation, and any change in surface shape relies solely on passive deformation arising from interactions with external objects. Here, we evaluate the extent to which food compression achieved solely by such simple inflation can contribute to tongue motion analysis.

In addition, we discuss sensing capabilities with practical application scenarios in mind. During mastication, humans deform the food bolus by pressing the flexible tongue against the hard palate thereby compressing and flattening the bolus. This deformation process involves a complex manipulation challenge where the tongue must bring a deformable object into a desired state by continuously sensing its changing shape and skillfully adjusting its movements in real time. To reproduc such intraoral manipulation *in vitro*, a mastication simulator requires two essential capabilities: (1) actuation, to shape the target material, and (2) sensing, to detect the state of the material and provide feedback for shaping. Although many actuators have been developed using forward-problem-based approaches to reproduce the tongue's actuation capability, little progress has been made in implementing the sensing capacity.

In this chapter, we propose a single-chamber PSA equipped with a visuo-tactile sensor that enables both surface shape sensing and actuation. The concept of the proposed PSA is shown in Fig. 2.1. This actuator employs a mechanism in which an object is pressed against the palate by a pneumatically inflated balloon to induce deformation. Shape sensing is achieved using a visuo-tactile sensor with concentrically arranged ring patterns on the surface membrane of the balloons. By estimating the height of each

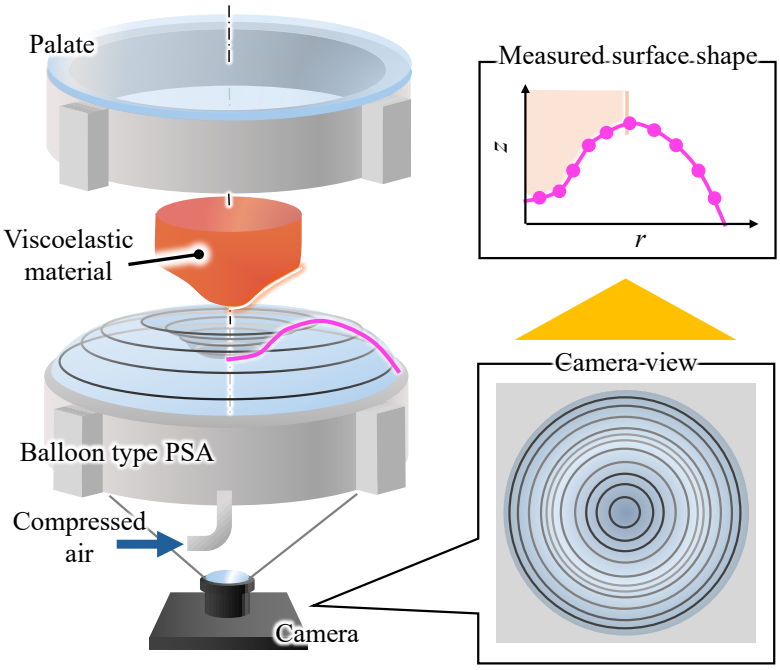
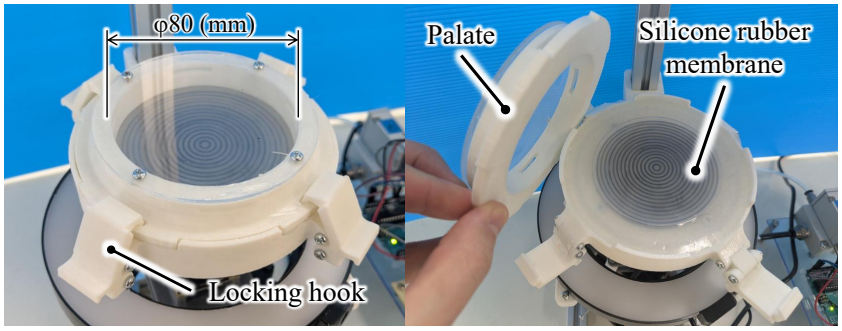


Figure 2.1: Basic concept of the PSA, which provides both surface shape sensing and actuation capabilities.

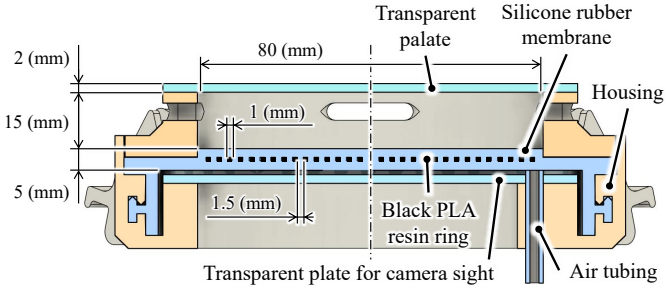
ring from camera view based on the pinhole camera model[83], the axisymmetric surface shape of the PSA can be discretely reconstructed in real time. In this study, a prototype of this PSA toward the tongue robot for *in vitro* mastication was developed. Shape sensing was performed on a rigid object and its measurement accuracy was evaluated. In addition, two application examples using this actuator were realized. First, differences in the shape change of a deformable body caused by two different input patterns were observed, verifying that the proposed PSA can be used for shaping manipulation. Then, a pressing motion was performed on four types of deformable objects, demonstrating that viscoelastic parameters can be estimated from time-series data of shape changes.

2.2 Proposed PSA

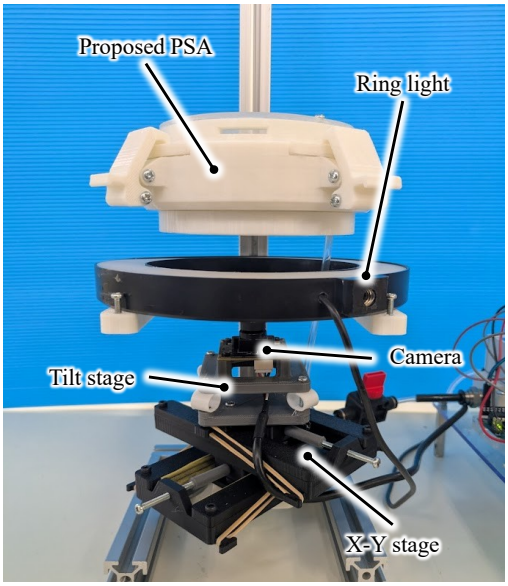
Fig. 2.2(a) shows the appearance of the proposed PSA, and Fig. 2.2(b) shows the cross-sectional view of the PSA. The actuator consists of a removable palate and a silicone rubber membrane that can be inflated with compressed air. The silicone rubber membrane was manufactured from silicone rubber (Dragon Skin 10 NV, Smooth-on, Inc., USA), which was cured via addition polymerization using platinum as a catalyst. 3D printed 15 black PLA resin rings (PLA Basic, Bambu lab, China) for the visuo-tactile sensor are concentrically arranged inside the 5 (mm) thick silicone rubber membrane. The width and thickness of the rings are 1 (mm). The distance between the rings is 1.5 (mm). The rings are rigid and will not deform significantly under pressure. When



(a)



(b)



(c)

Figure 2.2: Proposed balloon type PSA. (a) Appearance of the PSA. (b) Cross-sectional view of the PSA. (c) Arrangement of the proposed PSA and camera.

internal pressure is applied, the entire silicone rubber membrane is inflated owing to the elongation of the silicone rubber between the rings. The silicone rubber membrane

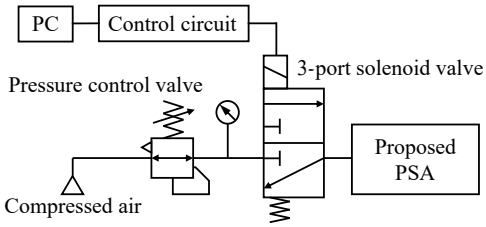


Figure 2.3: Pneumatic system for proposed PSA. The system consists of a pressure control valve and its self-made control circuit.

is attached to a PLA resin housing. A transparent plate is attached to the bottom of the housing to allow the back of the silicone rubber membrane to be observed. By observing the embedded rings through the bottom transparent plate, the deformation of the silicone rubber membrane can be observed without the object blocking the view. The bottom transparent plate is bonded to the housing with an acrylic modified silicone resin-based adhesive (Super X, CEMEDINE Co.,Ltd., Japan) to seal the chamber. The palate is attached to the housing with four locking hooks. The top plate is also transparent to enable the state of the object and the actuator to be observed from above.

Fig. 2.2(c) shows the arrangement of the proposed PSA and camera. The camera is mounted below the proposed PSA and records the deformation of the silicone rubber membrane from the bottom transparent plate. A fixed focus USB monocular camera module (USBFHD06H-FD100, Shenzhen Ailipu Technology Co.,Ltd, China) is used for this actuator. The camera is attached to the proposed actuator via a tilt stage and an X-Y stage and can be adjusted such that the center axis of the actuator and the optical axis of the camera coincide. The camera view is recorded at a resolution of 1080p and a frame rate of 30 (fps). An LED ring light (VE-2253, Etsumi Co.,Ltd., Japan) is positioned between the camera and proposed actuator to prevent the effects of optical disturbances caused by shadows.

The proposed PSA is driven by a pneumatic system shown in Fig. 2.3 consisting of a pressure control valve (GPR20006L, AirTAC, Taiwan), three-port solenoid valve (SYJ714R-5MZ-02, SMC Corp., Japan), and its self-made control circuit. The internal pressure applied to the PSA is maintained at a constant value by a pressure control valve. In addition, the pressurize time to the actuator can be adjusted by controlling the opening time of the three-port solenoid valve with commands from a PC.

2.3 Shape Sensing Method

For shape sensing, a concentric black ring pattern is captured from below by a monocular camera view as shown in Fig. 2.1. The axisymmetric shape of the silicone rubber membrane is measured using its estimated height from the radius of the ring in the camera view based on a pinhole camera model[83]. The silicone rubber membrane has

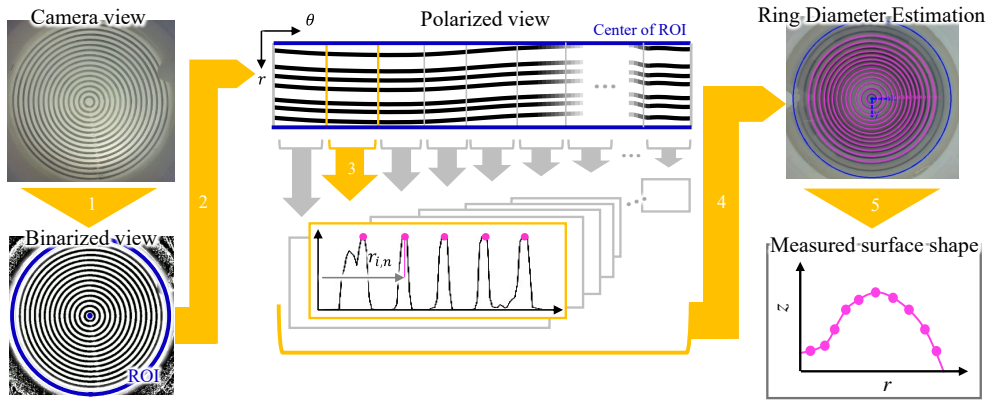


Figure 2.4: Algorithm of the shape sensing process.

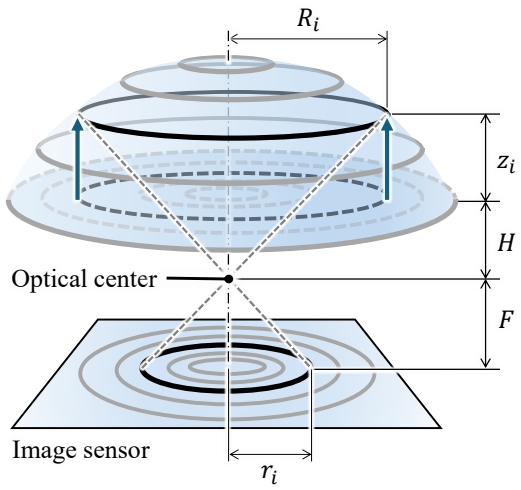


Figure 2.5: Pinhole camera model for surface shape sensing.

15 rings embedded in it, but the outer two rings are hidden by the housing during large inflations. The central ring has a large estimation error owing to its small radius and small number of pixels in the camera view. Therefore, in this case, 12 rings are used for the measurement, excluding the central ring and the two outer rings. Fig. 2.4 and the steps below show the details of the shape sensing process.

1. The camera view is binarized to emphasize the ring pattern. The `adaptiveThreshold` function in OpenCV[84] is used for binarization to minimise the influence of unintended brightness variations.

2. The polar coordinate transformation is applied within the ROI of the binarized view. This process transforms concentric patterns into parallel curves.

3. Curves aligned in a polarized view are detected, and the distance between the curves is calculated. The polarized view is divided into N sections along the θ direction. The pixel values of the divided sections are averaged along the θ direction, and peak detection is performed on them. For peak detection, the `find-peaks` function in Scipy[85] is used. The detected peak position $r_{i,n}$ (px) is the ith ring radius from the center in section n.

4. The radius r_i of i th ring is found by averaging the peak positions $r_{i,n}$ over all sections according to the following equation.

$$r_i = \frac{\sum_{n=1}^{N} r_{i,n}}{N} \tag{2.1}$$

5. Fig. 2.5 shows a camera model for surface shape sensing. Based on the pinhole camera model[83], the z-displacement of the ring z_i is estimated from the measured ring radius r_i using the following equation. Here, R_i (mm) is the radius of the black PLA resin ring, F (px) is the focal length on the pinhole camera model, H mm is the height of the silicone rubber membrane from the optical center.

$$z_i = \alpha \frac{R_i F}{r_i} - H \tag{2.2}$$

   α is a correction factor determined to make z_{i0}, the z-displacement when no internal pressure is applied, equal to zero.

2.4 Basic Experiment

2.4.1 Setup for Shape Sensing Experiment

To verify the shape sensing capability of the proposed PSA we measured the shape of the inflated silicone rubber membrane when it was pressed against seven different shapes of rigid objects. The rigid objects to be measured were convex shapes with a downward protrusion from the 15 (mm) height plane, as shown in Fig. 2.6(a). The distance between the vertex of the convex part and silicone rubber membrane was 5 (mm). The boundary between the convex part and flat plane was joined by fillets with $R = 10$ (mm). Six different shapes were prepared, with the radius of the convex part decreasing in 5 (mm) steps between $R = 40 - 15$ (mm), and these shapes were measured. A flat shape shown in Fig. 2.6(b) was also measured as a case where the radius of the convex part was increased to infinity. The internal pressure to the PSA during measurement was 30 (kPa).

2.4.2 Result of Shape Sensing Experiment

The measurement results are shown in Fig. 2.7. Fig. 2.7(a) shows the root-mean-square error (RMSE) between the rigid objects and measured actuator shapes. This graph

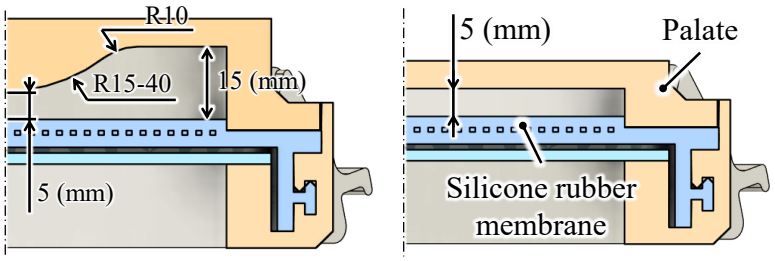


Figure 2.6: Rigid objects to be measured. (a) Convex shapes with a downward protrusion from the 15 (mm) height plane. (b) Flat shapes, as if the radius of the convex part were increased to infinity.

shows that the RMSE tended to increase as the radius of the convex part decreased. To check the individual measurement results, we compare the rigid object and measured actuator shapes in Fig. 2.7(b)-(e). The solid blue line is the rigid object shape and the magenta plot is the measured actuator shape. For the flat and $R = 40$ (mm) shapes shown in Fig. 2.7(b)-(e), the rigid object and measured actuator shapes matched, indicating that the object shape could be estimated with relatively high accuracy from the actuator shape. The RMSEs were also relatively small at around 0.6 (mm). In contrast a qualitative discrepancy between the rigid object and measured actuator shapes for the $R = 25$ and 15 (mm) is shown in Fig. 2.7(d),(e). The RMSEs were also relatively large, exceeding 2 (mm). This was probably owing to the high flexural rigidity of the silicone rubber membrane, which could not adhere to the large curvature of the rigid object. The measurement accuracy of shapes with large curvature could be improved by molding the silicone rubber membrane thinner.

2.4.3 Setup for Internal-Contact Pressure Characterisation Experiments

The relationship between the internal pressure of the PSA and contact pressure of the silicone rubber membrane was investigated to verify the load applied to the object. A pressure distribution sensor (I-SCAN40, NITTA, Inc., Japan) was attached to the palate to measure the contact pressure when internal pressure $P_{bi} = 5 - 45$ (kPa) was applied to the actuator. Fig. 2.8(a) shows an excerpt of the contact pressure distribution at $P_{bi} = 15$ (kPa). To calculate the load given to the object, we used the average value P_{bc} (kPa) of the 12 (mm)*12 (mm) area enclosed by the red square in Fig. 2.8(a).

2.4.4 Results of Internal-Contact Pressure Characterisation Experiments

Fig. 2.8(b) shows the relationship between the measured P_{bi} and P_{bc}. P_{bc} increased linearly with increasing P_{bi}. Previous studies have reported that mastication using the

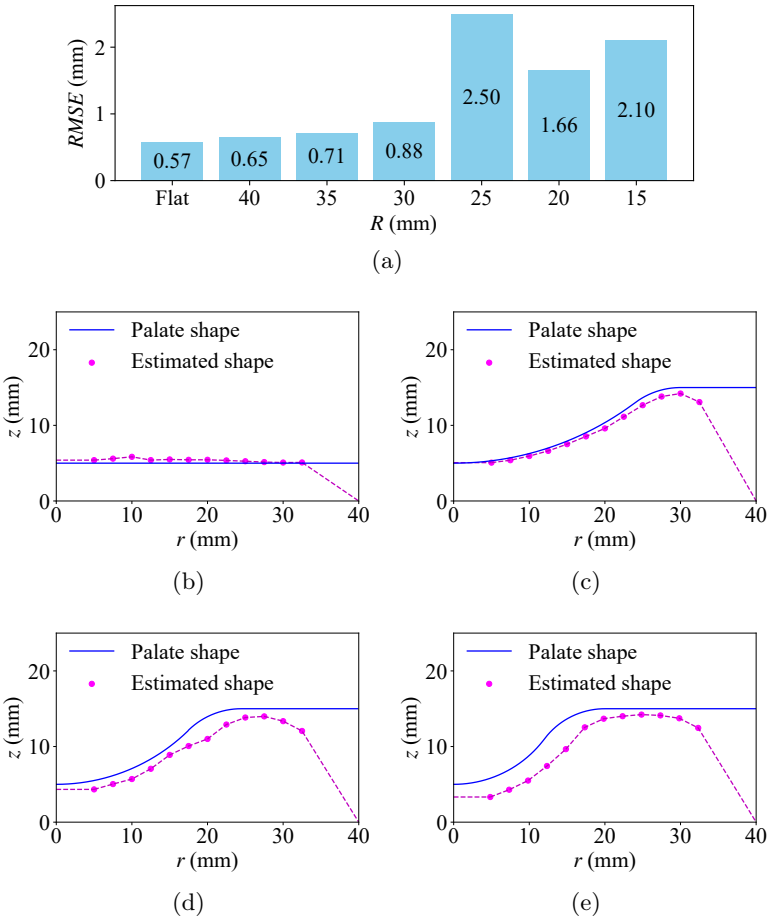
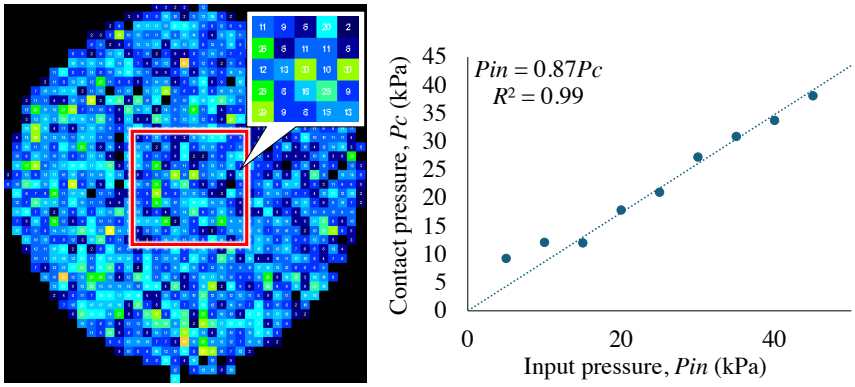


Figure 2.7: Measurement results. (a) RMSE between the rigid object and measured actuator shapes. (b) Individual measurement result of the flat shape. (c) Individual measurement result of the $R = 40$ (mm) shape. (d) Individual measurement result of the $R = 25$ (mm) shape. (e) Individual measurement result of the $R = 15$ (mm) shape.

tongue exerts a contact pressure of approximately 20–40 (kPa) on the food bolus[20,21]. Therefore, this actuator has a contact pressure range similar to that of the human tongue.

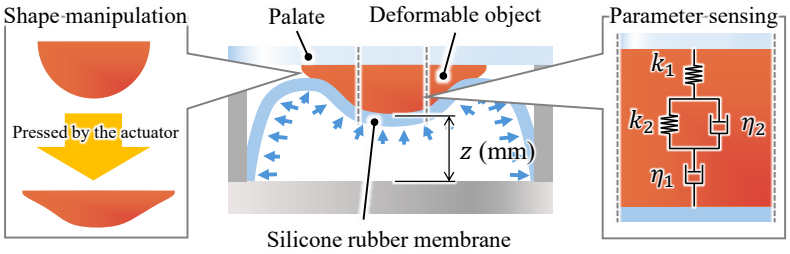
2.5 Sensing and Manipulation of Deformable Objects

Toward the realization of a tongue robot for *in vitro* mastication using the proposed PSA, the shaping manipulation and viscoelasticity evaluation for deformable objects were explored. First, differences in the shape change of a deformable body caused by two different input patterns were observed, verifying that the proposed PSA can be used for shape manipulation, as shown in the left part of Fig. 2.9(a). Then, a pressing motion was performed on deformable objects, demonstrating that viscoelastic

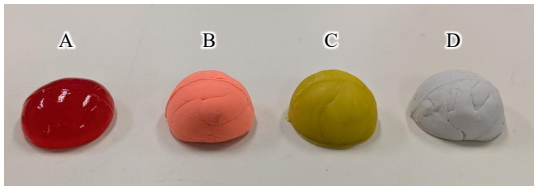


(a) (b)

Figure 2.8: Actuator contact pressure characteristics. (a) Contact pressure distribution on the palate of the actuator. (b) Relationship between P_{bi} and P_{bc}.



(a)



(b)

Figure 2.9: Overview of experiments on shape manipulation and sensing by the proposed PSA. (a) Shaping manipulation and viscoelastic parameter sensing. (b) Four types of clay used as deformable objects.

parameters can be estimated from time-series data of shape changes, as shown in the right part of Fig. 2.9(a). The four types of clay shown in Fig. 2.9(b) were used for these experiments.

2.5.1 Surface Shaping for a Deformable Object

As shown in the left part of Fig. 2.9(a), a deformable object was pressed and shaped by the inflated PSA. In this experiment, single-press was defined as a single pressurization

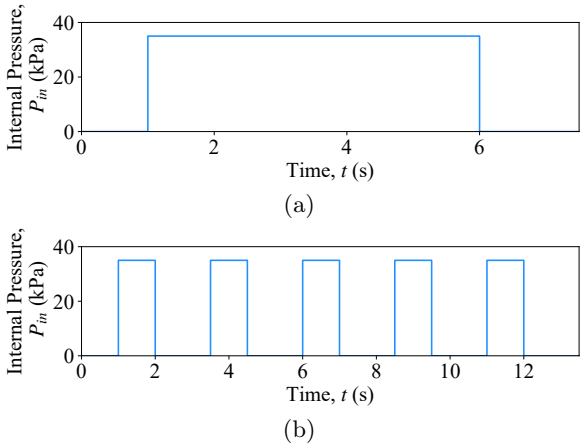


Figure 2.10: Input pressure patterns for shaping. (a) Single-press is defined as a single pressurization operation. (b) Multi-press is defined as multiple repetitions of 1 seconds of pressurization and 1.5 seconds of release.

operation of n s, and multi-press was defined as n repetitions of 1 second of pressurization and 1.5 seconds of release. The input internal pressure patterns for single-press and multi-press at $n = 5$ are shown in Fig. 2.10. The deformable object was pressed by each of these two types of push action, and the differences in the deformed shape owing to the push action were observed. The object was a clay B molded into a 15 (mm) hemisphere and placed such that the center of the hemisphere coincided with the central axis of the palate. Forming manipulations were preformed in the range of $n = (5, 10, 15, 20)$ for single-press and multi-press, respectively, with five trials each. The input internal pressure was set at 35 (kPa) to achieve a contact pressure P_c of 30 (kPa).

At the end of each trial, the final shape of the object was measured via proposed shape sensing method and compared between single-press and multi-press.

Fig. 2.11 shows the deformation of a deformable object. It could be seen from the top and bottom views in Fig. 2.11(a), the orange area expanded over time, indicating that the deformable object was being pressed. In addition, by comparing the initial and final shapes shown in Fig. 2.11(b), it could be confirmed that the shape was changed from a hemisphere to a flat convex shape.

Fig. 2.12 shows the shape of a deformable object measured by the proposed shape sensing method. The z displacement around $r = 25$ (mm) was 15 (mm) or more, which is expected because the silicone rubber membrane was in contact with the palate. Therefore, the area $r = 0 - 25$ (mm) of the measured shape was considered to represent the shape of the object, and this area was clipped and shown in Fig. 2.12. Fig. 2.12(a) shows the results of single-press shaping, and Fig. 2.12(b) shows the results of multi-press shaping. The final z displacement of the object at 20 seconds pressure in single-press was about 6 (mm), whereas the final z displacement at 20 pushes in multi-press was about 9 (mm), showing that multi-press was more effective than single-press in shaping the object to be more flattened. In the single-press shaping, the silicone rubber

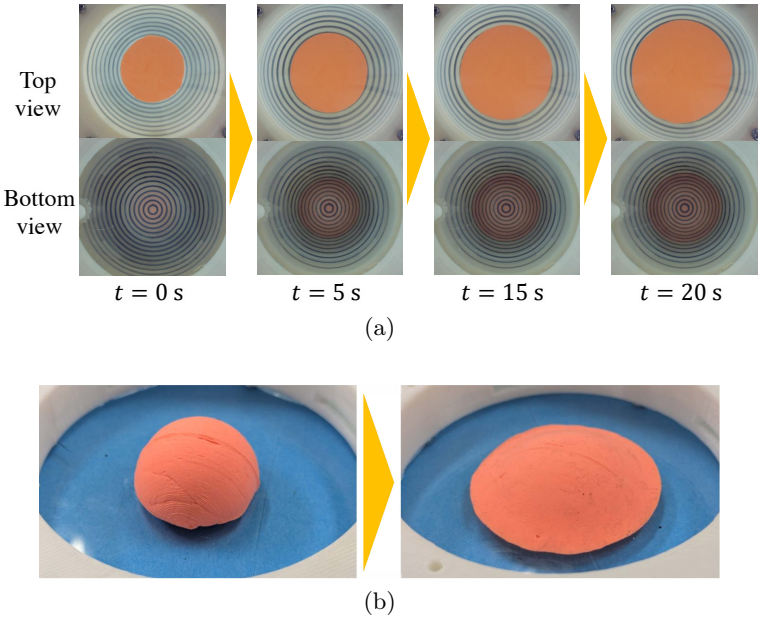


Figure 2.11: Changing the shape of a deformable object using single-press shaping. (a) Shape change seen from top and bottom view. (b) Comparing the initial and final shapes of a deformable body.

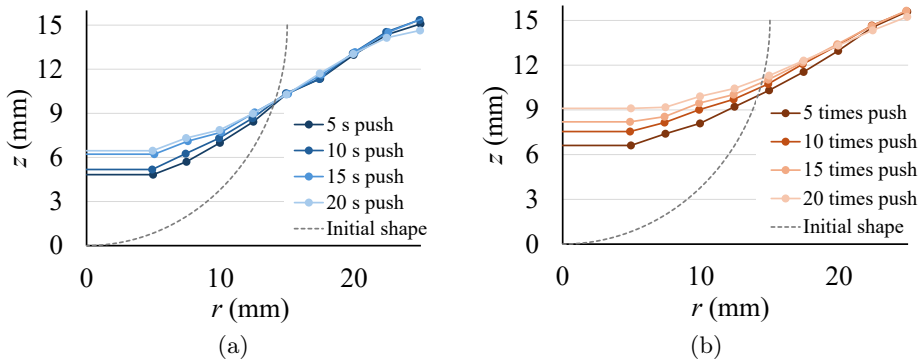


Figure 2.12: Surface shaping results. (a) The results of single-press shaping. (b) The results of multi-press shaping.

membrane fully expanded to cover the entire surface of the object, whereas in the multi-press shaping, the pressure was reduced before the silicone rubber membrane fully expanded. Therefore, in multi-press, the deformable object was expected to be deformed in a manner that it was pushed outwards, resulting in a flatter shape than in single-press. Although the total pressurize time was the same for the single-press and multi-press experiments, the final shapes was different. This result suggests that even with an actuation capability that allows only simple pressing, the deformation of the object can be manipulated to some extent by devising the input pattern.

2.5.2 Estimation of Viscoelasticity

As shown in the right part of Fig. 2.9(a), the proposed PSA was inflated for a certain period of time to press a deformable object, and the viscoelastic parameters were sensed from its displacement response. The initial shape of the object was a 15 (mm) radius hemisphere placed such that the center of the hemisphere coincided with the central axis of the palate. The distance between the palate and silicone rubber membrane was 15 (mm). Thus, the object was always in contact with the center of the silicone rubber membrane from the start of pressurization to unloading. Therefore, the displacement response $z(t)$ of the center of the silicone rubber membrane can be regarded as the deformation response of the deformable object under constant load.

In this experiment, the viscoelastic parameters of the Burgers model shown in the right part of Fig. 2.9(a) were sensed based on the displacement response of the most central black PLA resin ring embedded in the silicone rubber membrane. The four types of clay shown in Fig. 2.9(b) were used as deformable objects, and the measured viscoelastic parameters were compared. Assuming a constant contact pressure at the center of the silicone rubber membrane, the displacement response of the Burgers model is expressed by the equation below, where P_c is the contact pressure at the center of the silicone rubber membrane, k_1, k_2 are spring constants of the Burgers model, η_1, η_2 are the viscosity coefficients of the Burgers model, and R_1 is the radius of the black PLA resin ring at the center of the silicone rubber membrane. The pressurization pattern is 20 seconds single-press. The viscoelastic parameters k_1, k_2, η_1, η_2 are estimated using the Levenberg-Marquardt method[86–88] from the displacement response in the actual PSA and the following equation.

$$z(t) = P_c \pi R_1^2 \left(\frac{1}{k_1} + \frac{1}{k_2}(1 - e^{\frac{-k_2}{\eta_2}}) + \frac{1}{\eta_1} t \right) \tag{2.3}$$

Fig. 2.13(a) shows the displacement response and the result of the viscoelastic parameter measurement. The coloured dots corresponding to each clay are the average values from five displacement response measurements, the dotted lines are the theoretical values of displacement calculated using the measured viscoelastic parameters. In all displacement responses, an immediate displacement was observed at the start of pressurization, followed by an exponential increase in displacement and then a transition to a linearly increasing displacement creep phenomenon. This is a displacement response specific to the Bergers model. The measured displacement and theoretical responses are matched for all objects, confirming that the viscoelastic parameters can be correctly measured from the displacement response.

Fig. 2.13(b) shows the measurement results of the spring constants k_1, k_2. k_1 corresponds to the immediate displacement of each clay, with clay A having the smallest value and clay D having the largest value. k_2 exhibited generally the same trend as k_1, but the relationship was reversed in clays B and C. Fig. 2.13(c) shows the measurement results of the viscosity coefficients η_1, η_2. Clay D had a prominently large value of η_1, indicating its small creep displacement. Clay B had the largest value for η_2, indicat-

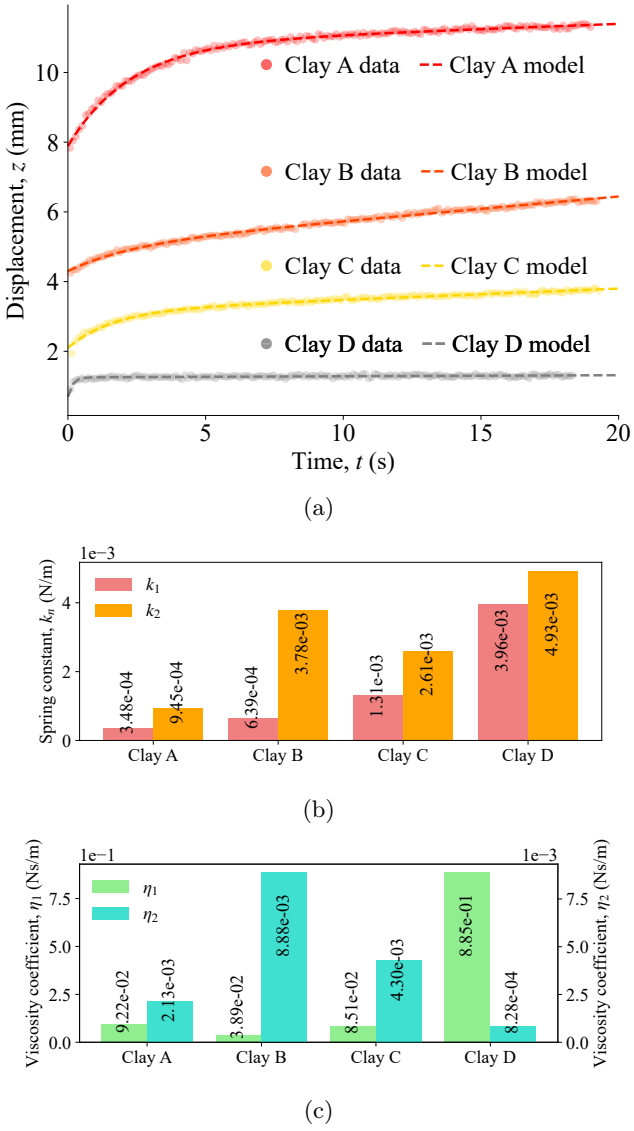


Figure 2.13: Viscoelasticity estimation result. (a) Displacement response and the result of the viscoelastic parameter measurement. (b) Measurement results of the spring constants k_1, k_2. (c) Measurement results of the viscosity coefficients η_1, η_2.

ing a long exponential increase in displacement. The measurement of the viscoelastic parameters confirmed that the different properties of the deformable object of interest can be quantitatively compared.

2.6 Conclusion

In this chapter, a single chamber PSA equipped with a visuo-tactile sensor was introduced as a forward-problem-based approach for developing a tongue robot for *in vitro* mastication, enabling both actuation and surface shape sensing.

- A PSA was developed with the capability of pressing a deformable object against the palate using a balloon inflated using air pressure. A concentric ring pattern obtained from the camera view was used to estimate the discrete surface shape of the PSA in real time.
- Shape sensing was performed on seven types of rigid objects, and we confirmed that the shape could be measured with an RMSE accuracy of less than 1 (mm), except for shapes with extremely large curvature.
- The capabilities of shaping manipulation and viscoelasticity evaluation for deformable objects were investigated. Two types of push actions were demonstrated on a deformable object, and the differences in the final shapes suggested that the proposed actuator can be utilized for forming manipulation. Pressing motions were performed on four types of deformable objects, showing that viscoelastic parameters can be estimated from time series data of shape changes.

These results identify and organize two key requirements for a tongue robot for *in vitro* mastication simulator: actuation and sensing. They also exemplify practical tongue robot applications. This study describes the implementation and design guidelines for realizing sensing functions, which have been insufficiently addressed by previous tongue actuators, while confirming that even a simple structure can achieve basic shaping manipulation.

However, in actual human mastication, not only compression patterns but also tongue shape changes play a crucial role. The simple single-chamber PSA used in this chapter provides only a limited range of achievable shapes. Constructing such actuators in a purely forward-problem-based design manner makes it difficult to reproduce the complex shaping manipulations performed by the human tongue. For the realization of a tongue robot for *in vitro* mastication, a significant challenge remains: developing novel actuator structures that enhance actuation capability and refining the corresponding design methodologies.

Chapter 3

Pressure Design Method for a Pneumatic Soft Actuator with Arrayed Chambers

3.1 Introduction

In this chapter, we consider the pneumatic soft actuator with arrayed chambers (PSA-AC), an actuator capable of producing highly deformable surface shapes as shown in Fig. 3.1(a). The PSA-AC has a structural feature in which rectangular chambers are arranged in an array, as shown in Fig. 3.1(b). By varying the internal pressure applied to each chamber, i.e., the internal pressure pattern, it can generate a wide range of surface shapes. This capability arises from the interaction between the expansion of chamber surfaces and the expansion, contraction, and bending of the inner walls separating the chambers. Consequently, PSA-AC can be said to possess structure that provide the potential to reproduce diverse surface shapes similar to those of the tongue. Although PSA-ACs have been partially adopted in existing tongue robots[47–50], their internal pressures are determined through trial-and-error, forward-problem-based approaches, and thus do not fully exploit the inherent surface shape generation capability of the PSA-AC structure. Moreover, increasing the number of chambers to enhance the diversity of representable surface shapes rapidly escalates the difficulty of forward-problem-based pressure design as the chamber count grows.

In this chapter, we examine an inverse-problem-based approach for designing internal pressure patterns to fully exploit the inherent variable surface shape capability of PSA-AC. Furthermore, through this approach, we evaluate the limits of the structural potential that PSA-AC possesses as a PSA with variable surface shapes. A new analytical model is introduced to describe the relationship between internal pressure patterns and surface shapes. Furthermore, a method is proposed to design an internal pressure pattern to reproduce the target surface shape. First, a discrete analytical model is constructed to represent the surface shape by focusing on the top end point of the inner wall of the PSA-AC and the center point of the chamber surface and connecting

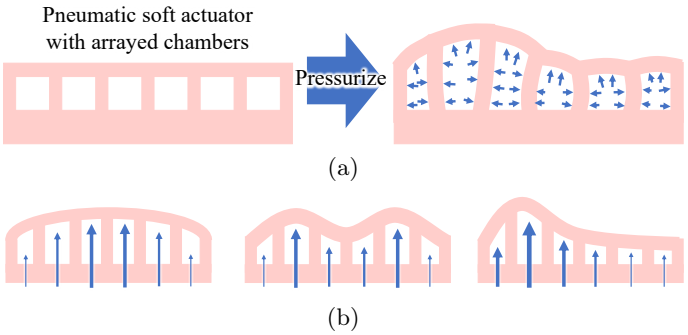


Figure 3.1: Basic concept. (a) Pneumatic soft actuator with arrayed chambers. Pressurizing each chamber changes the surface shape of the actuator. (b) Various target shapes are reproduced by changing the internal pressure patterns.

each point by elastic elements. Next, the mathematical optimization method uses this analytical model. This study presents a method for determining the internal pressure pattern to minimize the difference between the target surface and the model shapes using a nonlinear optimization method. Experiments were conducted to confirm the effectiveness of the proposed method. Four characteristic target surface shapes such as ellipsoidal, concave, one-sided convex, and crevasse are inputted to the 8-chamber PSA-AC, and the internal pressure pattern is determined for each shape. In addition, these internal pressure patterns are applied to the actual PSA-AC to demonstrate the reproducibility of the target surface shape.

3.2 Modeling of PSA-AC

Fig. 3.2 shows the PSA-AC surface shape model used in this study, and it is assumed that the structure consists of N chambers arranged horizontally. Furthermore, the PSA-AC surface shape model represents the two-dimensional surface shape in the vertical section of the center of the PSA-AC. The PSA-AC surface shape model consists of two units: the chamber inner wall unit, which expresses the coordinates of the upper end of the chamber inner wall elongated by the internal pressure, and the chamber surface unit, which expresses the coordinates of the center of each expanded chamber surface. Each unit consists of several elastic elements and nodes connecting them, which are displaced by applying virtual forces based on the linear pressure in the chamber to the nodes. The PSA-AC ends are fixed and the PSA-AC surface shape model consists of $N-1$ chamber inner wall models and N chamber surface models. The dimensions of each part shown in Fig. 3.3 are the same for all chambers. In the diagram, t_s is the thickness of the chamber surface, t_w is the thickness of the chamber's inner walls, l_s is the distance between the chamber inner walls and l_w is the distance from the bottom edge of the chamber to the center of the chamber's surface.

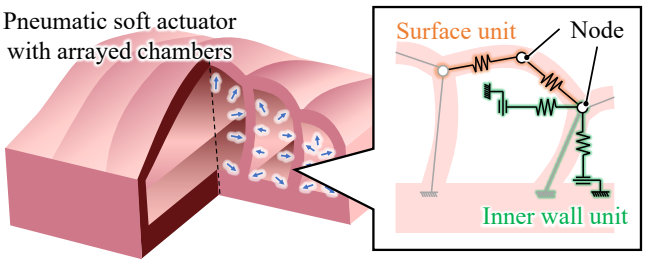


Figure 3.2: Configuration of the surface shape model. The model consists of the surface and inner wall units.

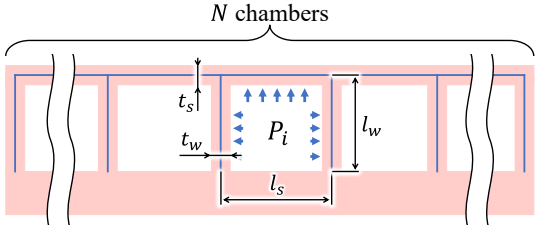


Figure 3.3: Dimensions of each chamber. These are the same for all chambers except for the pressure values.

3.2.1 Chamber Inner Wall Unit

Fig. 3.4(a) shows the inner wall unit of the chamber, which consists of horizontal and vertical linear elastic elements with elastic forces acting in the horizontal and vertical directions, respectively. The natural length $l_s/2$ and the spring constant k_s are the horizontal linear elastic element parameters. In contrast, the natural length l_w and the spring constant k_w are for the vertical linear elastic element. The linear elastic element of the spring constant k_s at the inner chamber wall unit is an approximate representation of the tension from the elastic membrane on the PSA-AC surface. By simplifying the interaction with the chamber surface membrane in this manner, it is possible to apply the mathematical optimization introduced in Section III. The spring constants k_s and k_w are obtained using the following equation:

$$\boldsymbol{k} = \begin{bmatrix} k_s \\ k_w \end{bmatrix} = El_d \begin{bmatrix} t_s \dfrac{2}{l_s} \\ \dfrac{t_s}{l_w} \end{bmatrix} \tag{3.1}$$

where l_d represents the chamber depth length of PSA-AC. E represents Young's modulus of elasticity for the flexible material and is calculated from the stress at 100 % elongation. The elongation is achieved via a uniaxial tensile test using the dumbbell-shaped test piece No. 1 specified in Japanese industrial standards (JIS) K6251. The virtual forces $F_{wx,i}$ and $F_{wy,i}$ applied to these linear elastic elements respectively are given by the

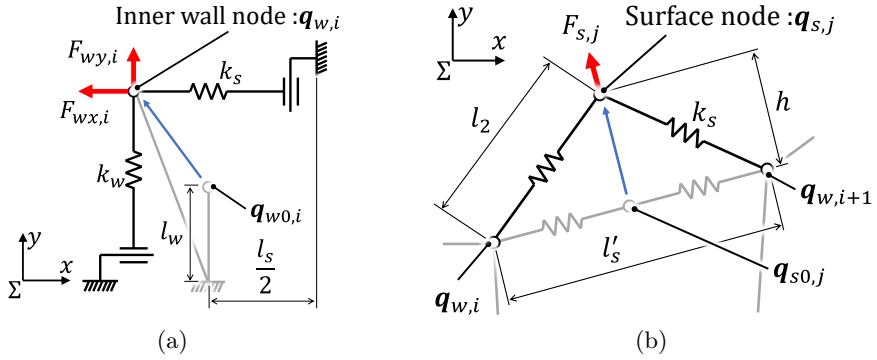


Figure 3.4: Proposal surface shape model. (a) Chamber inner wall unit. (b) Chamber surface unit.

linear pressures P_i and P_{i+1} in the two adjacent chambers, respectively:

$$\boldsymbol{F}_{w,i} = l_d \begin{bmatrix} F_{wx,i} \\ F_{wy,i} \end{bmatrix} = l_d \begin{bmatrix} l_w(P_{i+1} - P_i) \\ \dfrac{l_s}{2}(P_{i+1} + P_i) \end{bmatrix} \tag{3.2}$$

The position vector $\boldsymbol{q}_{w,i}$ of the ith inner wall node in the model is given by the following equation:

$$\boldsymbol{q}_{w,i} = \beta \begin{bmatrix} \dfrac{F_{wx,i}}{k_s} \\ \dfrac{F_{wy,i}}{k_w} \end{bmatrix} + \boldsymbol{q}_{w0,i} \tag{3.3}$$

where $\boldsymbol{q}_{w0,i}$ is the position of the inner wall node before deformation, and β is the displacement correction factor. Note that β varies depending on the depth length l_d, which is cancelled out when calculating equation (3.3).

3.2.2 Chamber Surface Unit

Fig. 3.4(b) shows the surface unit of the chamber, which consists of two linear elastic elements of natural length $l_s/2$ and spring constant k_s, connected at both ends by rotating pairs. These linear elastic elements are pre-stretched to length $l'_{s,j}$ and placed between the inner wall nodes $\boldsymbol{q}_{w,i}$ and $\boldsymbol{q}_{w,i+1}$ calculated according to equation (3.3). Assume that the virtual force $F_{s,j}$ perpendicular to the line connecting $\boldsymbol{q}_{w,i}$ and $\boldsymbol{q}_{w,i+1}$ is the input to the surface unit. If the length of the elastic element when the virtual force is applied to the jth surface node is $l_{2,j}$ and the displacement in the direction parallel to the converted force is h_j, then the force equilibrium at the center of the

chamber surface coordinate $\boldsymbol{q}_{s,j}$ can be expressed as follows.

$$F_{s,j} = P_j l_s l_d \tag{3.4}$$

$$F_{s,j} = 2k_s\Big(l_{2,j} - \frac{l_s}{2}\Big)\frac{h_j}{l_{2,j}} \tag{3.5}$$

$$h_j = \sqrt{l_{2,j}^2 - \Big(\frac{l_{s,j}^{'}}{2}\Big)^2} \tag{3.6}$$

Obtaining h_j in equation (3.6) through analysis is difficult, hence a numerical solution must be obtained using iterative calculations. However, the computation time of the model increases each time h_j is calculated numerically and it becomes difficult to apply the mathematical optimization methods. Therefore, both sides of equations (3.5) and (3.6) are divided by $l_s/2$ and k_s. The equations become nondimensional as follows:

$$\zeta = 2(\xi - 1)\frac{\kappa}{\xi} \tag{3.7}$$

$$\kappa = \sqrt{\xi^2 - \nu^2} \tag{3.8}$$

where $\zeta = P/k_s$, $\xi = 2l_2/l_s$, $\nu = l_s^{'}/l_s$,and $\kappa = 2h/l_s$ are the dimensionless quantities represented by the following equations (3.7) and (3.8). Note that P_i is a line pressure, and therefore has the dimension MT^{-2}. The approximate value of κ is obtained by sampling the numerical solutions of κ within practical limits and surface-fitting them with the bi-variate polynomial $g(\zeta, \nu)$, which $g(\zeta, \nu)$ will be referred to as the surface unit characteristic function. Using the surface unit characteristic function, the approximate value of $h_j^{'}$ for h_j is given by the following equation:

$$h_j' = g\Big(\zeta_i, \nu_j\Big)l_s = \kappa' l_s \tag{3.9}$$

Using h_j' obtained from equation (3.6), the position vector $\boldsymbol{q}_{s,j}$ of the center of the chamber surface is given as follows:

$$\boldsymbol{q}_{s,j} = \beta \begin{bmatrix} q_{sx0,j} - 2h_j' \dfrac{q_{sy0,j}}{l_{s,j}'} \\ q_{sy0,j} + 2h_j' \dfrac{q_{sx0,j}}{l_{s,j}'} \\ \end{bmatrix} \tag{3.10}$$

where $\boldsymbol{q}_{s0,j}$ is the position vector of the surface node before adding $F_{s,j}$.

3.2.3 Fitting of the Surface Unit Characteristic Function.

To determine the surface unit characteristic function $g(\zeta, \nu)$, the numerical solution of κ is sampled and fitted with a bivariate polynomial. Numerical solutions were obtained via iteration using calculations using *Matlab*'s *vpasolve* with a sampling range of $0 \leq \nu \leq 10$, $0 \leq \zeta \leq 10$. In addition, a bivariate cubic polynomial was used for the surface unit characteristic function and fitted using the least-squares method.

Table 3.1: Parameters of the surface unit characteristic function

a_{mn}	value	a_{mn}	value	a_{mn}	value
a_{00}	0.98	a_{12}	-2.71E-2	a_{30}	-6.66E-3
a_{01}	0.59	a_{13}	1.14E-3	a_{31}	3.52E-3
a_{02}	-2.11E-2	a_{20}	0.12	a_{32}	-5.28E-4
a_{03}	1.27E-3	a_{21}	-5.71E-2	a_{33}	2.52E-5
a_{10}	-0.66	a_{22}	8.08E-3		
a_{11}	0.22	a_{23}	-3.73E-4		

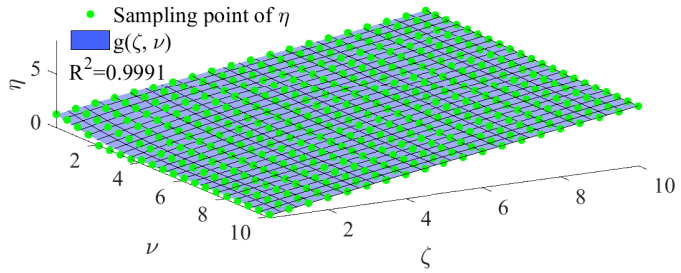


Figure 3.5: Dimensionless approximation κ of h_j for dimensionless quantities ν and ζ.

$$g(\zeta, \nu) = \sum_{m=0}^{3} \sum_{n=0}^{3} a_{mn} \nu^m \zeta^n \tag{3.11}$$

Table 3.1 and Fig. 3.5 show the results of fitting the surface unit characteristic functions. Fig. 3.5 shows that ζ increases monotonically with increasing ζ and decreases nonlinearly with increasing ν.

3.2.4 Model Considering Contact Forces

When using a PSA-AC for manipulation tasks, it is necessary to consider the influence of contact forces acting on its surface. By adding contact force terms to each node of the surface shape model, the internal pressure required to compensate for passive deformation caused by these forces can be designed. Details are provided in Appendix A due to space limitations.

3.3 Solving For The Internal Pressure Pattern

Based on the PSA-AC surface shape model described in the previous chapter, a nonlinear optimization method is used to obtain the internal pressure patterns to achieve

the target shape. The internal pressure pattern is defined as the chamber's internal pressure vector in the following equation:

$$\boldsymbol{p} = \Big[P_1 \ , \ \cdots \ , \ P_N \Big]^T \tag{3.12}$$

First, the error of the model shape with considering the given target surface shape is calculated. The PSA-AC surface shape is represented by $2N-1$ position vectors, alternating between the chamber's inner wall node $\boldsymbol{q}_{w,i}$ calculated from equation (3.3) and the surface node $\boldsymbol{q}_{s,j}$ calculated from equation (3.10) in the chamber surface model. Vector $\boldsymbol{\theta}_{\mathrm{model}}$ is defined by arranging these position vectors as follows.

$$\boldsymbol{\theta}_{\mathrm{model}} = \Big[\boldsymbol{q}_{s,1}^T \ , \ \boldsymbol{q}_{w,1}^T \ , \ \cdots \ , \ \boldsymbol{q}_{s,N-1}^T \ , \ \boldsymbol{q}_{w,N-1}^T \ , \ \boldsymbol{q}_{s,N}^T \Big]^T \tag{3.13}$$

As shown in Fig. 3.6, the point where the distance between each point of the surface shape model and the target surface shape is the minimum is $\boldsymbol{q}_{\mathrm{target,k}}$. Furthermore, the vector of these x and y coordinates in order is $\boldsymbol{\theta}_{\mathrm{target}}$ and is defined as follows:

$$\boldsymbol{\theta}_{\mathrm{target}} = \Big[\boldsymbol{q}_{\mathrm{target},1}^T \ , \ \cdots \ , \ \boldsymbol{q}_{\mathrm{target},2N-1}^T \Big]^T \tag{3.14}$$

The error between the model and the target surface shape $\boldsymbol{\Theta}$ and its sum of squares S is given by the following equation:

$$\boldsymbol{\Theta} = \boldsymbol{\theta}_{\mathrm{target}} - \boldsymbol{\theta}_{\mathrm{model}} \tag{3.15}$$

$$S = \sum_{k=1}^{4N-2} r_k^2 \tag{3.16}$$

where r_k is the kth element of $\boldsymbol{\Theta}$. The internal pressure pattern is obtained by solving a nonlinear least-squares problem to minimize S. The Jacobi matrix $\boldsymbol{J}$ of $\boldsymbol{\Theta}$ is given as follows:

$$\boldsymbol{J} = \begin{bmatrix} \nabla \boldsymbol{\Theta}_1(\boldsymbol{p})^T \\ \vdots \\ \nabla \boldsymbol{\Theta}_{4N-2}(\boldsymbol{p})^T \end{bmatrix} = \begin{bmatrix} \dfrac{\partial r_1}{\partial P_1} & \cdots & \dfrac{\partial r_1}{\partial P_N} \\ \vdots & \ddots & \vdots \\ \dfrac{\partial r_{4N-2}}{\partial P_1} & \cdots & \dfrac{\partial r_{4N-2}}{\partial P_N} \end{bmatrix} \tag{3.17}$$

To update the pressure values from appropriate initial values p(0), the Levenberg-Marquardt method[86–88] is used to calculate the following equation iteratively.

$$\boldsymbol{p}^{(m+1)} = \boldsymbol{p}^{(m)} - \Big[\big(\boldsymbol{J}^{(m)}\big)^T \boldsymbol{J}^{(m)} + \delta^{(m)} \boldsymbol{I} \Big]^{-1} \big(\boldsymbol{J}^{(m)}\big)^T \boldsymbol{\Theta}^{(m)} \tag{3.18}$$

where $\boldsymbol{I}$ is the unit matrix and δ is the damping factor. m is the number of steps in the iterative calculation. $\boldsymbol{p}^{(m)}$, $\boldsymbol{J}^{(m)}$, $\delta^{(m)}$, and $\boldsymbol{\Theta}^{(m)}$ are $\boldsymbol{p}$, $\boldsymbol{J}$, δ, and $\boldsymbol{\Theta}$ at step m, respectively. In iterative calculations, the following steps are used to search for solutions.

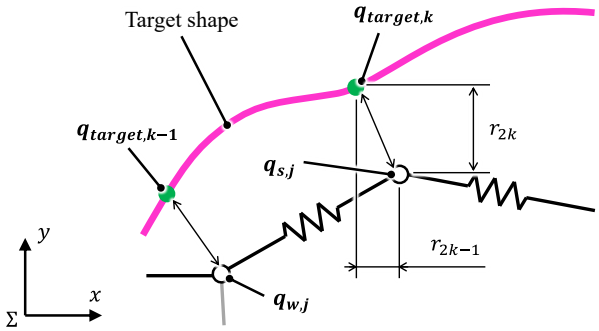


Figure 3.6: Deviation between the target surface shape and the proposed model. Obtain the minimum distance between the target surface shape and $\boldsymbol{q}_{w,i}, \boldsymbol{q}_{s,j}$ as the deviation and implement mathematical optimization for minimization.

1. Define the initial values $\boldsymbol{p}^{(0)}$, $\delta^{(0)}$, and scaling factor ($f > 1$).
2. Calculate the sum of squares from equation (3.16) at the current pressure value $\boldsymbol{p}^{(m)}$, which is $S^{(m)}$. Calculate the sum of squares $S(\delta^{(m-1)})$ in the same way for the pressure value $\boldsymbol{p}^{(m-1)}$ updated by $\delta^{(m-1)}$.
3. If $S^{(m)} < S(\delta^{(m-1)})$, then $\delta^{(m)} = f\delta^{(m-1)}$ and determine $\boldsymbol{p}^{(m+1)}$ according to equation (3.18).
4. If $S^{(m)} \geq S(\delta^{(m-1)})$, then $\delta^{(m)} = \delta^{(m-1)}/f$, and $\boldsymbol{p}^{(m+1)} = \boldsymbol{p}^{(m-1)}$. In addition, the pressure value is updated.
5. If the updated pressure value $\boldsymbol{p}^{(m+1)}$ contains a negative value, that element is set to 0, because in real machines the pressure control valve can only apply positive pressure.
6. Calculate the norm of the second term on the right-hand side of equation (3.18) and return to step 2. if it is larger than the convergence criterion. If it is smaller, it is considered to have converged, and the iterative calculation is terminated.

3.4 Experiment

3.4.1 Prototyped PSA-AC and Measurement Methods for Surface Shapes

Fig. 3.7(a) shows the PSA-AC used in the experiment, whereas Fig. 3.7(b) shows the corresponding cross-sectional dimensions. The PSA-AC consisted of 8 horizontally arranged chambers. In addition, the actuator was manufactured from silicone rubber (Dragon Skin 10 NV, Smooth-on, Inc., USA) which was cured by addition polymerization using platinum as a catalyst. The modulus of elasticity for the silicone rubber was

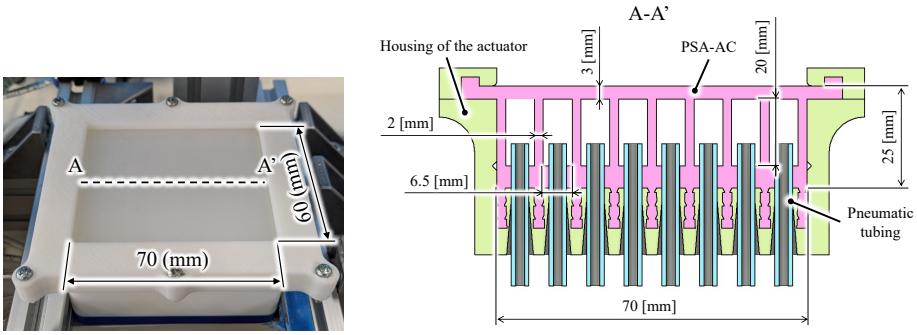


Figure 3.7: Prototyped PSA-AC. (a) Appearance of the PSA-AC. (b) Dimensions of each chamber. These are the same for all chambers except for the pressure values.

measured when the stress $E = 0.2015$ MPa at 100 % elongation, which was achieved a simple pure shear tensile test using the test method[89,90] proposed by Treloar. The outer circumference of the PSA-AC surface and the bottom of the PSA-AC are provided with tabs of length 8 mm and 10 mm, respectively, which were sandwiched and fixed to the housing.

The experimental and surface shape measurement environment is shown in Fig. 3.8. Pressure valves were connected to each chamber of the PSA-AC to control the pressure values individually. The surface shape was measured using a scanning laser displacement sensor(OPTEX FA Inc., repeatability accuracy 45 μm) mounted on a motorized slider in the horizontal direction.

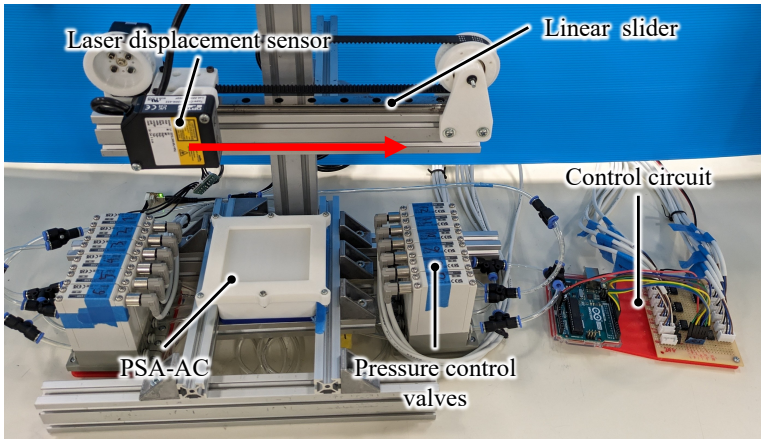
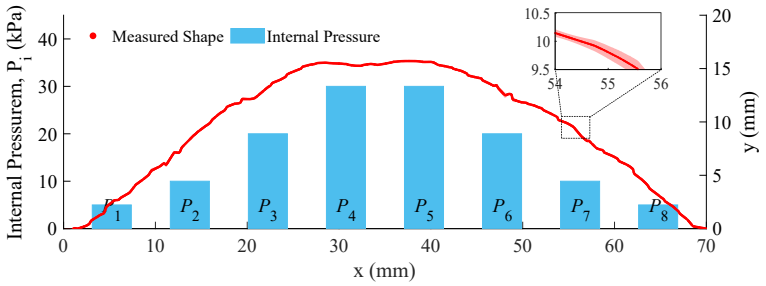
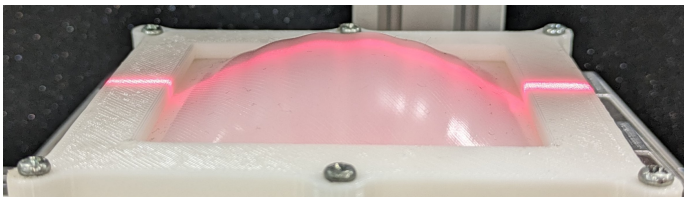


Figure 3.8: Experimental setup for measuring the surface shape of the PSA-AC. The surface shape is obtained by horizontally scanning laser displacement sensor with a linear slider.



(a)



(b)

Figure 3.9: Preliminary experimental result. (a) Applied internal pressure pattern and PSA-AC surface shape across ten pressurised trials. The light blue bars represent the pressure values applied to each chamber. The red dots and shaded pink regions indicate the mean values of the measured shape and twice the standard deviations (2σ), respectively. (b) Appearance of the actual PSA-AC.

3.4.2 Preliminary Experiment

To evaluate the characteristics of the prototyped PSA-AC, the surface shape was obtained when the 8-chamber PSA-AC was pressurized. In the experiment, the predetermined internal pressure pattern was applied for 3 s and then the pressure was reduced was repeated ten times.

Fig. 3.9 shows the applied internal pressure pattern, measured surface shape, and appearance of the actual PSA-AC. In Fig. 3.9(a), the light blue bars represent the pressure applied to each chamber, whereas the red dots represent the mean values of the measured shape over ten measurements. The pink area in Fig. 3.9(a) shows the standard deviation of 2σ. The experimental results show that the surface shape exhibited a symmetrical convex shape with a height of approximately 13 mm, with the highest vertical displacement near the P_3 and P_4 chambers, where the internal pressure was the highest at 30 kPa. The standard deviations over ten trials were approximately 0.5 mm, confirming sufficient reproducibility for repeated pressurisation. The displacement correction factor in the sections Ⅱ was set to $\beta = 2.5$ to ensure that the maximum displacement of the model under the internal pressure patterns shown in Fig. 3.9(a) is similar to that of the measured PSA-AC shape.

3.4.3 Surface Shape Reproduction Experiment

The internal pressure patterns obtained from the target surface shapes based on the proposed method are applied to the actual PSA-AC. The surface shapes obtained are compared and their reproducibility is evaluated.

Target Surface Shape and Optimization Parameters

The target surface shapes to be reproduced in this experiment were the concave, one-sided convex, ellipsoidal, and crevasse represented by the solid magenta lines in Fig. 3.10–3.13(b). These target shapes were determined with reference to previously measured dorsal tongue shapes[14,15,25], which exhibit up to two prominent peaks.

Furthermore, the parameters used in the nonlinear optimization were the initial values of the damping factor $\lambda^{(0)} = 0.001$, scaling factor $f = 10$, convergence decision value $\epsilon = 10^{-5}$, and initial pressure values $P_i^{(0)} = 10\ kPa$.

Experimental Result and Discussion

Fig. 3.10–3.13 show the results of the applied internal pressure pattern and the target elliptical, concave, one-sided convex, and crevasse shapes, as well as model shape, measured surface shape, and the appearance of the actual PSA-AC for each of the abovementioned shapes.

The target and model shapes of the ellipsoidal, concave, and one-sided convex shape in Fig. 3.10–3.12(b) were compared and it was shown that the qualitative shapes generally matched and the appropriate internal pressure pattern was obtained by nonlinear optimization on the model. The root mean square error between the target and model $RMSE_{\text{model-target}}$ shape was less than 1.0 mm for both shapes. However, for the crevasse shape in Fig. 3.13(b), the extreme convexity of the target surface shape had become a smooth shape in the model, and it can be confirmed that it had not been reproduced accurately. This could be because of the inappropriate structural parameters, such as chamber resolution for the target surface shape. Appropriate modifications of the structural parameters were essential in improving the reproducibility of the target surface shape on the model.

Comparing the measured and target surface shapes for the ellipsoidal, concave, and one-sided convex shapes in Fig. 3.10–3.13(b) shows that the root mean square error $RMSE_{\text{ex-target}}$ between the measured and target surface shapes was less than 1.3 mm. Therefore, it can be verified that the proposed method can be used to determine the appropriate internal pressure patterns to reproduce the target surface shape on the actual PSA-AC. However, for the crevasse shape in Fig. 3.12(b), although the $RMSE_{\text{ex-target}}$ was within 1.3 mm for the other shapes, the reproducibility of the concavity part was low. To improve the shape reproducibility, reviewing the structural parameters and implementing measures such as applying negative pressure to suck the chamber surface to improve the representation of concavity parts is necessary. Moreover, the qualitative crevasse shape between the measured and model was consistent. This suggests that

the proposed method could be used as a simulator to determine whether the structural parameters of the PSA-AC are appropriate for the target surface shape.

For comparison, a simple internal pressure pattern in which pressure value for each chamber was proportional to its target height was also tested. In this proportional internal pressure pattern, the pressure value $P_{\mathrm{prop},i}$ was determined as follows:

$$P_{\mathrm{prop},i} = P_{\max}\frac{H(q_{sx0,i})}{H_{\max}} \tag{3.19}$$

where $P_{\max}$ is the maximum pressure value, $H(q_{sx0})$ is the height in the target shape at q_{sx0}, and $H_{\max}$ is the maximum height in the target shape. $P_{\max}$ was set to 30.4 kPa, which is the average of the four highest pressure values obtained respectively for the four target shapes by using the proposed optimization method. In each of Fig. 3.10–3.13, (c) shows the result for the proportional internal pressure pattern. As can be observed in Fig. 3.10–3.13, comparing the measured shape for the internal pressure pattern determined by the proposed method (b) with that for the proportional internal pressure pattern (c), the former pattern reproduced the target shape qualitatively better. This result confirms the advantage of the proposed method considering the interaction between chambers in the PSA-AC.

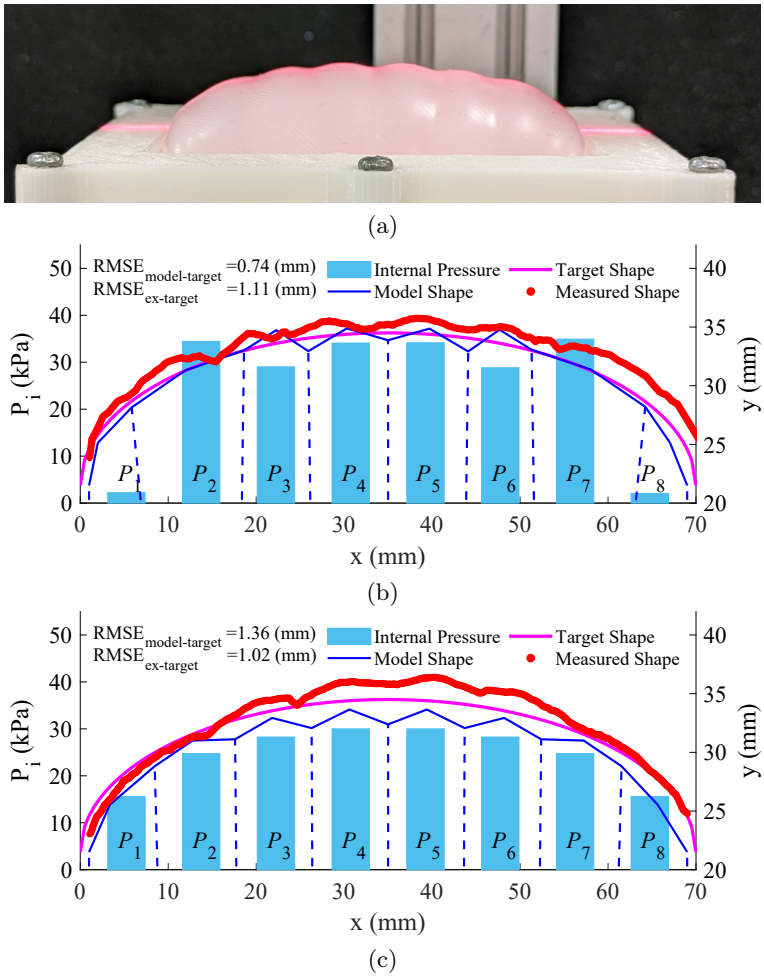


Figure 3.10: Experimental results of the ellipsoidal shape. (a) Appearance of the actual PSA-AC. (b) Applied internal pressure pattern determined by optimization and comparison of surface shapes. (c) Applied proportional internal pressure pattern and comparison of surface shapes.

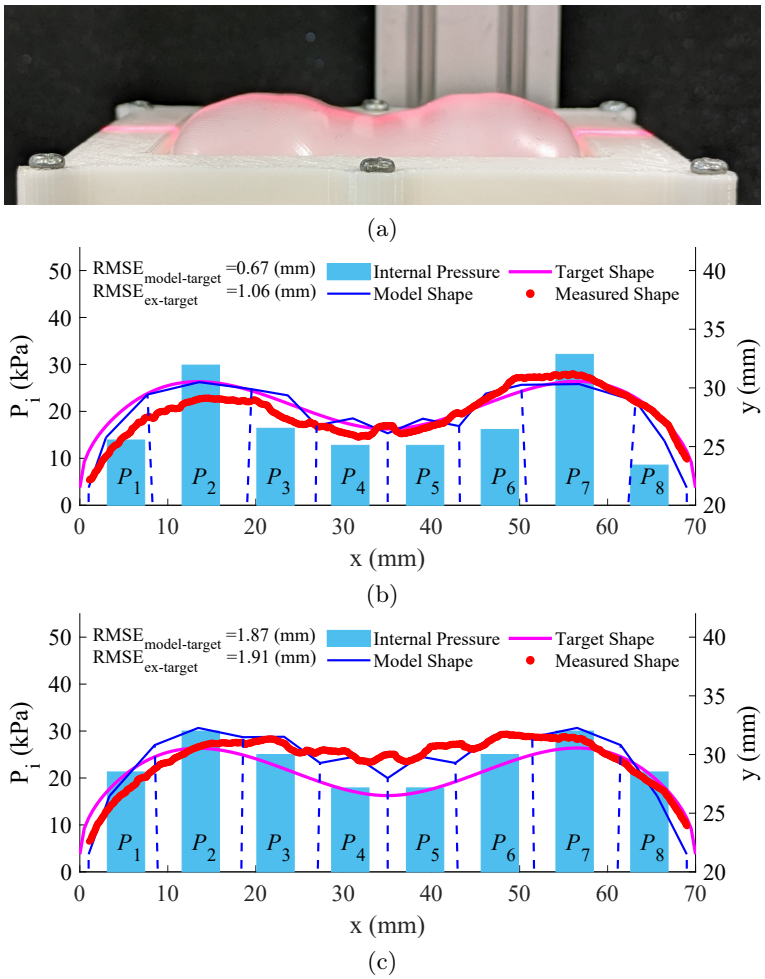


Figure 3.11: Experimental results of the concave shape. (a) Appearance of the actual PSA-AC. (b) Applied internal pressure pattern determined by optimization and comparison of surface shapes. (c) Applied proportional internal pressure pattern and comparison of surface shapes.

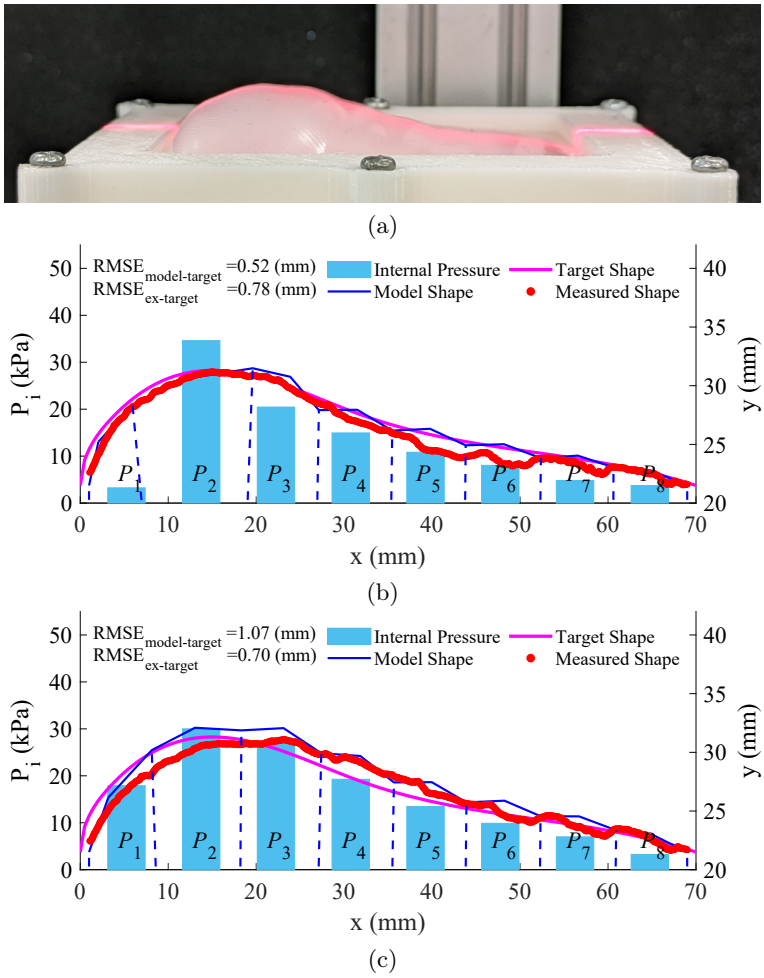


Figure 3.12: Experimental results of the one-sided convex shape. (a) Appearance of the actual PSA-AC. (b) Applied internal pressure pattern determined by optimization and comparison of surface shapes. (c) Applied proportional internal pressure pattern and comparison of surface shapes.

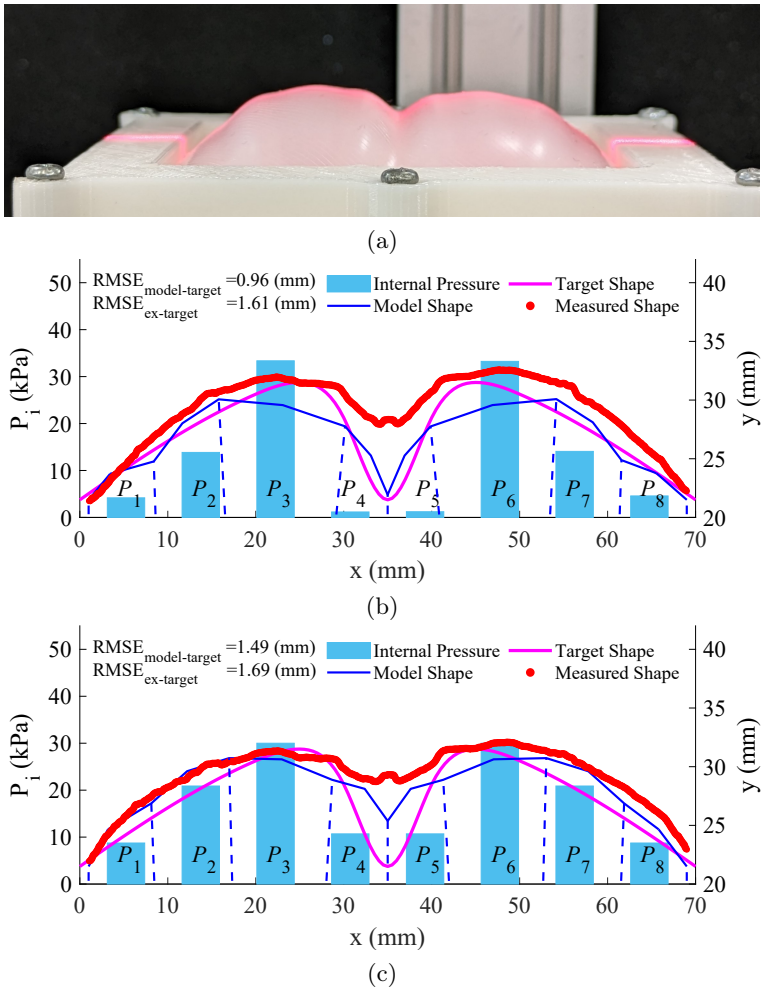


Figure 3.13: Experimental results of the crevasse shape. (a) Appearance of the actual PSA-AC. (b) Applied internal pressure pattern determined by optimization and comparison of surface shapes. (c) Applied proportional internal pressure pattern and comparison of surface shapes.

3.5 Conclusion

In this chapter, we discussed a pneumatic soft actuator with arrayed chambers and proposed a design method of internal pressure patterns to reproduce the target surface shape.

- An analytical PSA-AC surface shape model was presented for the internal pressure pattern. The model consisted of the upper endpoints of the inner wall of the chamber, the center of the surface, and the elastic elements connecting them.
- A method for determining the internal pressure pattern to minimize the difference between the target surface shape and the model shape using a nonlinear optimization technique was presented.
- The effectiveness of the proposed method was evaluated experimentally: four characteristic target surface shapes were considered for the eight-chamber PSA-AC, and internal pressure patterns were obtained. These internal pressure patterns were inputted to the PSA-AC, showing that the target surface shape could be reproduced qualitatively.

The results demonstrate the effectiveness of the PSA-AC as a PSA with variable surface shapes and validate the utility of the proposed inverse-problem-based pressure pattern design method. It was confirmed that optimal internal pressure patterns, which maximize the potential of the PSA-AC structure, can be determined through modeling and optimization. However, the proposed method addresses only the internal pressure pattern design with a predefined and uniform actuator structure. Thus, the approach represents only a partial implementation of inverse-problem-based design. Structural design continues to rely on empirical tuning and trial-and-error processes, offering no guarantee of optimality. The reproducibility of target shapes is constrained by the fixed structure. Establishing a comprehensive design framework that integrates both structural and pressure pattern design remains a key challenge for realizing tongue robots for *in vitro* mastication.

Chapter 4

Novel Pneumatic Soft Actuator Composed of Layered Membranes and Its Design for Structure and Pressure

4.1 Introduction

In the previous chapter, we examined a structure capable of realizing variable surface shapes, in which rectangular chambers were arranged in an array. This structure defined a single rectangular chamber as the minimum unit, yet its behavior presents several issues as shown in left side of Fig. 4.1(a). When a chamber is pressurized, the junction between the inner wall and the surface membrane moves in a coupled manner, and this deformation is simultaneously affected by the internal pressures of neighboring chambers. These mutual interactions complicates the behavior and makes it difficult to predict. Moreover, the inflation that occurs at the center of the inner wall develops internally within the chamber and does not contribute to surface shape generation, making this configuration inefficient as a fundamental structure for a pneumatic soft actuator (PSA) with variable surface shapes. Overall, a pneumatic soft actuator with arrayed chambers (PSA-AC) structure that adopts rectangular chambers as its minimum elements is not easy to handle, either from a structural design standpoint or in terms of achieving efficient surface shape deformation.

To address these issues, we redefine the minimum structural element of a variable-surface-shape PSA as a single membrane as shown in right side of Fig. 4.1(a). A membrane on its own has a relatively simple shape, and it can be described using only a small number of parameters. This feature is advantageous for computational handling of actuator shape and can serve as a key foundation for developing an inverse-problem-based structural design method. A rectangular chamber in PSA-AC can be interpreted as being composed of three membranes. In the inner wall membrane, only the extension

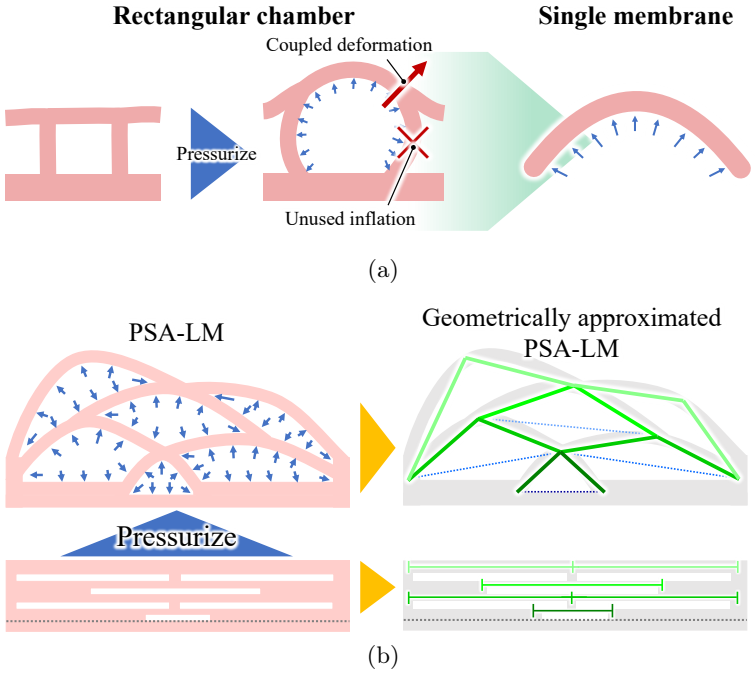


Figure 4.1: Basic concept of the structural feature. (a) Redefining the minimum element of the structure from a rectangular chamber to a membrane. (b) The PSA-LM proposed in this study is a type of soft actuator that can change its shape and easily approximate simple geometric shapes.

of the endpoints is utilized through its connections, whereas the central region is not connected to any other component. As a result, the inflation of this membrane does not contribute to surface shape generation. To effectively translate membrane inflation into surface deformation, it is essential to establish connection rules that specify how multiple membranes should be joined. Such rules can lead to identifying structural features that efficiently realize variable surfac shape functionality.

In this chapter, we present a novel soft actuator that combines high flexibility with rich shape diversity, similar to the human tongue, as well as a design method that systematically derives both structural parameters and internal pressure patterns from target shapes. To address these requirements, We propose a pneumatic soft actuator composed of layered membranes (PSA-LM). PSA-LM has a two-dimensional structure with layered elastic membranes and can achieve surface shape changes using only soft materials, as shown on the left side of Fig. 4.1(b). In PSA-LM, the membrane endpoints are connected to vertices of the membrane on the lower layer. When the membranes are inflated, the layer by layer stacked displacements result in a large displacement and smooth surface shape. Furthermore, as shown on the right side of Fig. 4.1(b), the membrane shape of PSA-LM can be approximated geometrically as stacked isosceles triangles when inflated and straight line segments when not pressurized. In other words, these geometric approximations allow us to easily handle the shape of PSA-LM

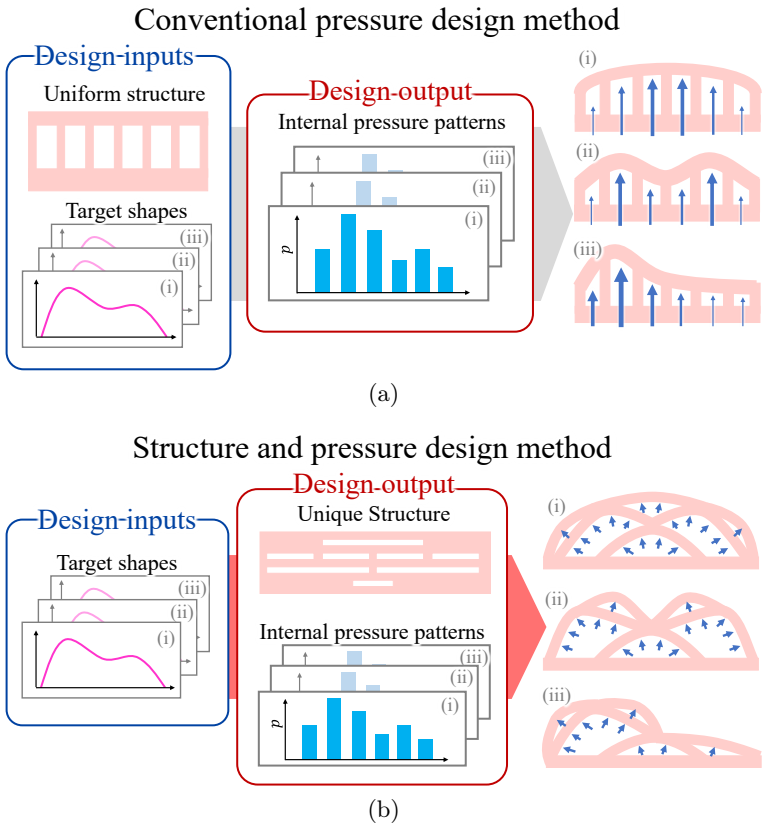


Figure 4.2: Basic concept. (a) PSA-AC design method can only design pressure and uses a uniform structure and target shapes. (b) PSA-LM uses only target shapes and can design both pressure and a unique structure.

mathematically without using computationally expensive methods such as FEA. This characteristic allows PSA-LM design problems to be converted into graph theory problems, opening up a new path for establishing inverse-problem-based design methods for surface-shape-variable soft actuators. The previous chapter demonstrated a partial inverse-problem-based method to design internal pressure patterns for a pneumatic soft actuator with arrayed chambers (PSA-AC) as shown in Fig. 4.2(a). In this chapter, a complete inverse-problem-based design method that outputs a single structure with multiple internal pressure patterns corresponding to each of multiple target shapes, as shown in Fig. 4.2(b), is proposed. A method for geometrically designing the membrane structure of PSA-LM is introduced by approximating the target shape using isosceles triangles. The internal pressures applied to each membrane are designed by applying an analytical model and optimization with FEA to the designed membrane structure. The effectiveness of the proposed method was evaluated by reproduction experiments for five types of target shapes using actual PSA-LM and by comparing it with conventional methods using FEA-based validation of tongue-like target shape reproduction.

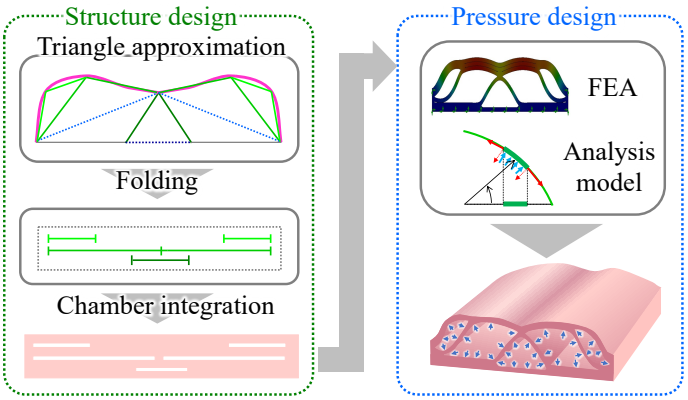


Figure 4.3: Overview of PSA-LM design. After the geometric structural design is complete, the internal pressure pattern design is performed using optimization and analysis models.

4.2 Design Process

Fig. 4.3 shows an overview of the proposed design process. First, the corresponding inflated membrane structures for each two-dimensional target shape are geometrically determined by approximating the shape with a stack of isosceles triangles. Then, a design algorithm is constructed to determine a single folded membrane structure by geometrically folding and integrating these approximated inflated membrane structures. Next, the internal pressure patterns for each target shape are determined using a membrane analysis model and Bayesian optimization with FEA for the designed membrane structure. This method produces a single actuator structure and control inputs that can be used for multiple target shape, thereby paving the way for a systematic design process for tongue robots.

4.3 Basic Behavior of Layered Membranes

The basic behavior of layered elastic membrane structures must be organized to establish the PSA-LM structural design method. As an example of the minimum configuration of PSA-LM, the left column of Fig. 4.4 shows five types of layerd membrane structures. FEA confirms the deformation of Structures 1 to 5 when internal pressure is applied. Structures 1 to 5 all have a double layered structure consisting of an upper membrane and lower membranes, each 3 mm thick, with a total width of 50 mm and a total thickness of 9 mm including the thickness of the base. The space under the membrane functions as a chamber. The conditions of FEA are the same as those described later in Section 4.7 Experiments.

The middle row of Fig. 4.4 shows the deformation behavior based on FEA analysis when 10 kPa is applied to all chambers of Structures 1 to 5. Structure 1 consists only of a single upper membrane, which inflates uniformly due to internal pressure. In Structures

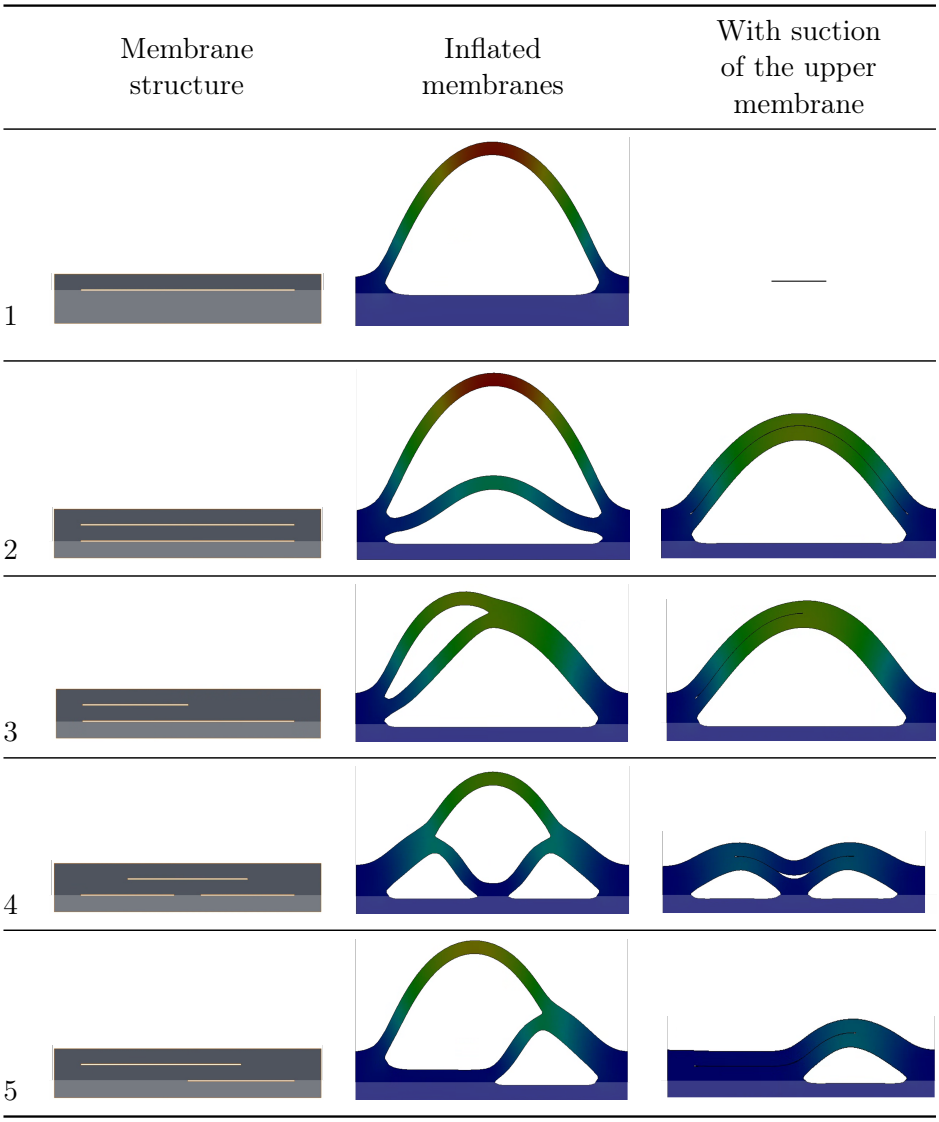


Figure 4.4: Bahavior of layerd membranes. Layered membranes exhibit different deformation behaviors depending on the endpoint connections and whether positive or negative pressure is applied.

2 through 4, the lower and upper membranes have two layers with different connection patterns. In Structure 2, the upper and lower membranes are connected at both ends. When Structure 2 inflates, only the deformation of the upper membrane appears on the surface, therefore, the outer shape is the same as that of Structure 1. Deformation of the lower membrane is covered and hidden by the upper membrane and does not contribute to surface shape changes. This indicates that a membrane structure such as Structure 2 that completely overlaps does not affect the surface shape of PSA-LM. In Structure 3, the upper membrane connects the endpoints and the center point of

the lower membrane. When Structure 3 inflates, displacement of the upper membrane is stacked on the left side of the large convex shape created by the lower membrane, forming a small convex shape that results in a shape in which the apex of the outer shape shifts to the left. In Structure 4, the upper membrane is connected between the center points of the lower membrane. During inflation, the displacement of the upper membrane is stacked between the two convexes formed by the lower membranes, resulting in an outer shape with a sharp convex shape at the center. In Structure 5, the upper membrane is connected to the left fixed end and the center of the lower membrane. During inflation, the upper membrane forms a large convex shape between the fixed end and apex of the inflated lower membrane. As a result, a convex shape is formed, with the apex of the outer shape shifted to the left. The deformation behaviors of the above structures confirms that when one or both ends of the upper membrane are connected to the apexes of the lower membrane, the displacement of the upper membrane is efficiently stacked to the displacement of the lower membrane.

The deformation behavior when negative pressure is applied to the upper membrane was also confirmed. The results are shown in the right column of Fig. 4.4. In Structure 2, positive pressure causes less inflation. In this case, the upper and lower membranes are in close contact with each other and behave as a single 6 mm thick membrane. In Structure 3, the convex shape on the left side caused by inflation of the upper membrane has disappeared obtaining a single membrane with a thickness of 6 mm, as in Structure 2. In Structures 4 and 5, the upper membranes are sucked in and adhere to the lower membranes. As a result, the unevenness of the inflated lower membranes appears on the surface when the convex shape in the upper membranes disappears. Based on the above results, switching the negative and positive pressures applied to the upper membrane can cause a mode switch, whereby the upper membrane transmits the deformation of the lower membrane, generating a mode in which the displacement of the upper membrane is stacked onto the lower membrane. When deforming the designed single structure into multiple target shapes, some membranes may be unnecessary depending on the target shape. In this case, by applying negative pressure to the unnecessary membranes, the deformation of the lower membranes can be controlled and transmitted to the surface.

4.4 Structural Design Method

4.4.1 Overview of Structural Design

Inflated PSA-LM membrane structures for each target shape are determined by filling the target shape with isosceles triangular elements that approximate the shape of a single inflated membrane. In this process, the physical properties of the membrane and internal pressure are not considered at all, and the membrane structure is determined based solely on the geometric shape.

The target shapes, defined as Ω_i, are shown in Fig. 4.5(a), where, i is the shape index. Isosceles triangular elements $\boldsymbol{m}_{i,j,k}$ which indicate a single inflated membrane are defined by the three points, as shown in Fig. 4.5(a), namely $\boldsymbol{m}_{\mathrm{left},i,j,k}$, $\boldsymbol{m}_{\mathrm{center},i,j,k}$,

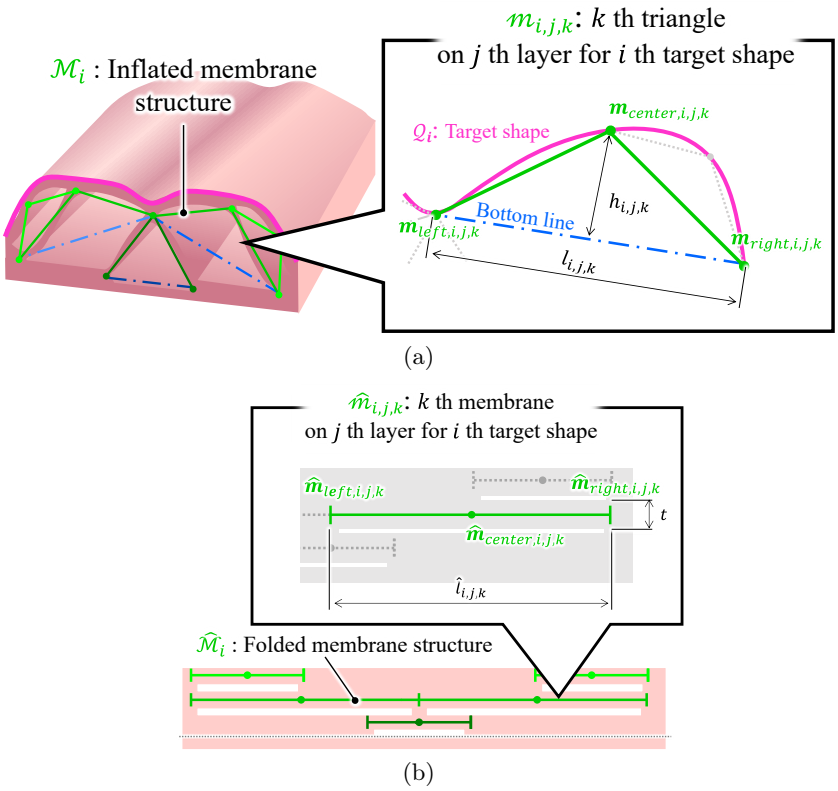


Figure 4.5: Geometrial elements that indicate PSA-LM membrane. (a) Isosceles triangle elements representing the inflated membrane. (b) Line segments representing the folded membrane.

and $\boldsymbol{m}_{\text{right},i,j,k}$, where, j is the layer index, and k is the triangular element index within the j th layer. These triangular elements are generated by first establishing the bottom line and then determining the height. By repeating triangular elements generation for each layer, the inflated PSA-LM membrane structure is represented by the triangular elements set $\mathcal{M}_i = \{\boldsymbol{m}_{i,j,k} \mid j = 1, \ldots, J,\ k = 1, \ldots, K\}$.

An overview of the structural design algorithm is shown in Fig. 4.6. First, bottom lines of triangular elements belonging to the first layer are determined, as shown in Fig. 4.6(a-1). The first layer is unique because it has a fixed lower end and restrains the displacement of the concave portion. Therefore, in determining the bottom line for the first layer a different algorithm must be used.

In the beyond steps, triangular elements are generated for each target shape. First, the triangle heights are determined, as shown in Fig. 4.6(b). Next, the bottom lines are determined, as shown in Fig. 4.6(a-2). The bottom lines are determined for the membrane displacement to stack effectively, based on the connection rules indicated in Fig. 4.4. These two processes, triangle height and bottom line determination, are repeated until the termination conditions are met. Then, the folding process required for

triangular shape approximation shape is performed, as shown in Fig. 4.6(c). In this process, the heights of the generated triangular elements are set to zero while maintaining the mutual connection between the endpoints. This allows the membrane to be folded into a flat shape, resulting in a folded membrane structure that corresponds to each shape. Finally, folded membrane structures obtained for each shape are integrated into a single folded membrane structure using the integration process shown in Fig. 4.6(d). In this process, the folded membrane structures are compared and the common parts are integrated. By completing all the above processes, a single folded membrane structure capable of reproducing multiple target shapes is obtained.

The details of each process are explained below. As an example, we also explain the structural design using the two target shapes shown in Figs. 4.7(a) and (b).

4.4.2 First Bottom Line Determination

The structure of the first layer is determined in this process, namely the membrane positioned at the lowest level. The PSA-LM is a structure that generates surface shapes by stacking inflated membranes. In the first layer, the bottom lines $\boldsymbol{m}_{\mathrm{right},i,1,k}-\boldsymbol{m}_{\mathrm{left},i,1,k}$ are determined so that the concave points of all target shapes are placed at the apex of right-angled triangles. Convex shapes are easy to reproduce, but concave points require appropriately constraining the deformation of the relevant area. Deformation is constrained by aligning the apex of the membrane at maximum inflation with each concave point, which improves the accuracy of reproducing the concave shape. The approximate shape of the membrane at maximum inflation is assumed to be a right-angled isosceles triangle. This is because when the height $h_{i,j,k}$ of the trianglular element is larger than half of the bottom line length $l_{i,j,k}$ ($h_{i,j,k} \geq l_{i,j,k}/2$), the membrane model used to determine the initial value of the internal pressure pattern (described in Section 4.5.2) cannot be applied. For concave points detection, the `find-peaks` function in `Scipy`[85] is used. The bottom line of the first layer corresponding to the detected concave point $\boldsymbol{q}_{concave,n}$ is determined by the following equation:

$$\boldsymbol{q}_{concave,n} = \begin{bmatrix} qx_{concave,n} \\ qy_{concave,n} \end{bmatrix} \tag{4.1}$$

$$\boldsymbol{m}_{\mathrm{left},i,1,k} = \begin{bmatrix} qx_{concave,n} - qy_{concave,n} \\ 0 \end{bmatrix} \tag{4.2}$$

$$\boldsymbol{m}_{\mathrm{right},i,1,k} = \begin{bmatrix} qx_{concave,n} + qy_{concave,n} \\ 0 \end{bmatrix} \tag{4.3}$$

If the generated bottom lines overlap, these line are discarded and the corresponding concave point coordinates are averaged and merged into a single representative concave point. The bottom line is regenerated based on this representative concave point. If there are no concave points in either target shape, the entire bottom edge of the target shape is used as the bottom line of the first layer.

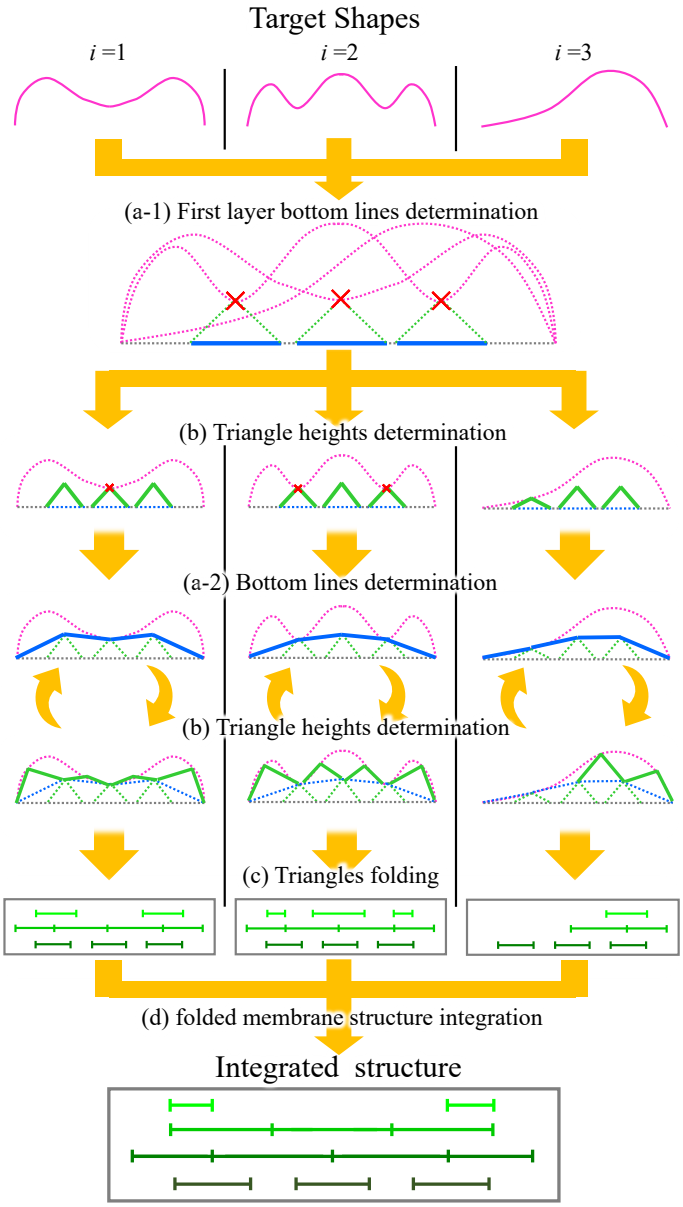


Figure 4.6: Structure design process. PSA-LM structure was geometrically designed using a triangular approximation of the target shape, folding, and integration.

The bottom lines thus obtained are used as the common initial layer for all target shapes. Subsequent layers are generated sequentially based on this layer to create a structure that appropriately constrains the concave displacement of all target shapes.

Figs. 4.7(c) and (d) show the results of triangle generation for the example shapes. In example shape 1, one concave point is detected, as shown in Fig. 4.7(a). In triangle

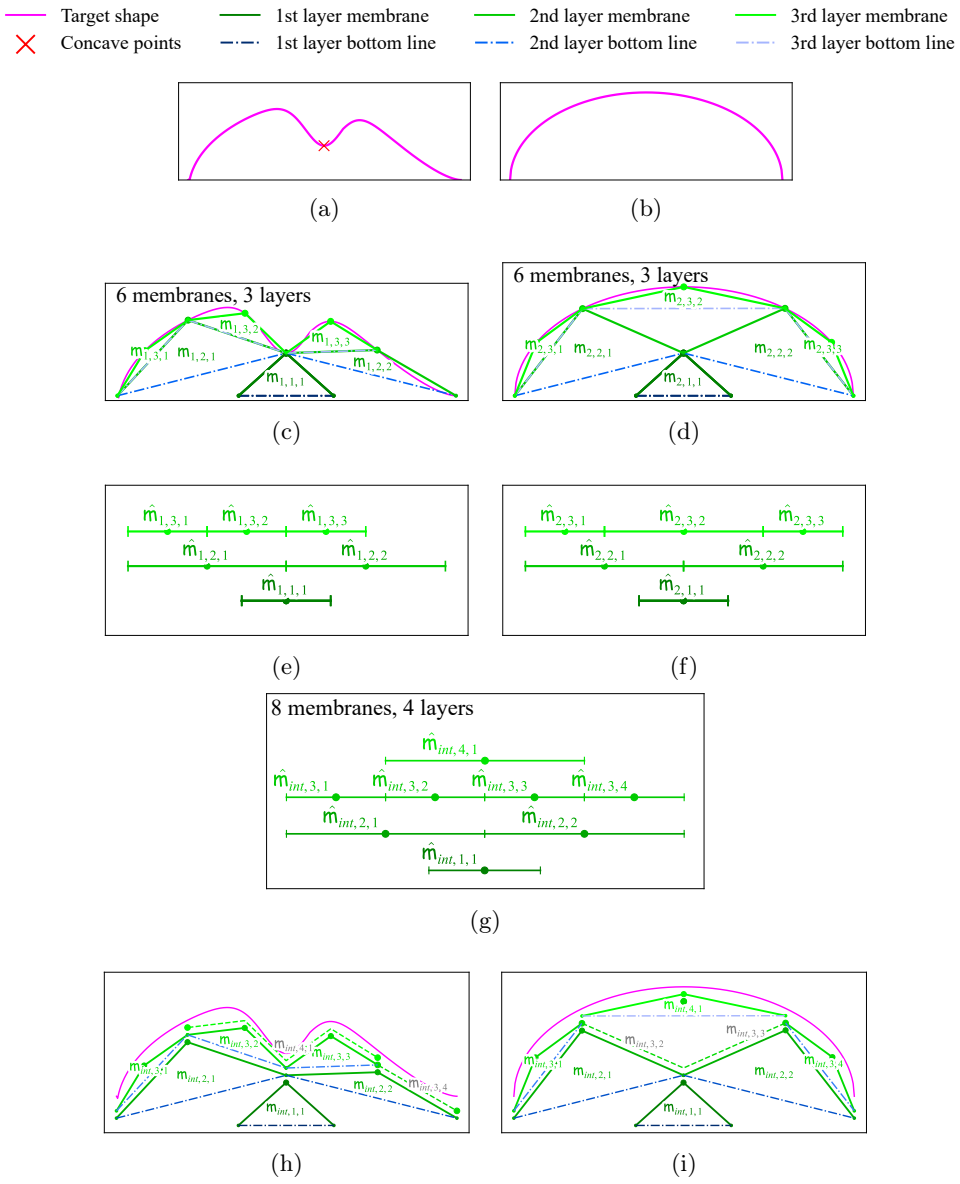


Figure 4.7: Structural design examples. (a)(b) Target shapes. (c)(b) Target shapes expressed as stacks of isosceles triangles. (e)(f) Designed folded membrane structures. (g) Integrated membrane structure. (h)(i) Inflated shapes of the integrated membrane structure.

generation process, the bottom line is determined so that $m_{1,1,1}$ is generated with this concave point as the apex. Example shape 2 does not have any concave points. However, since the first bottom line is common to all the target shapes, a triangle $m_{2,1,1}$ is generated from the same bottom line as that of example shape 1.

4.4.3 Other Bottom Line Determination

The structures of the layers from the second onward are determined in this process. The bottom lines of the j th layer in the second layer and beyond are determined using the polygon $\mathcal{R}_{i,j-1} = \{\boldsymbol{r}_{i,j-1,n} \mid n = 1, 2, \ldots, N\}$ representing the outer shape of the j-1 th layer.

The line segments connecting each vertices of $\mathcal{R}_{i,j}$ can be candidates for the bottom line. Of these candidates, those that do not meet the conditions shown in Fig. 4.8 were adopted as the bottom line.

- Condition 1:
  The case of line segment entering the region surrounded by $\mathcal{R}_{i,j-1}$. Line segments that satisfy this condition generate membrane elements that do not contribute to the formation of surface shapes, such as Structure 1 shown in Fig. 4.4, or structurally inappropriate membrane elements that intersect with existing layers are generated. Therefore, these are excluded from the bottom line candidates.

- Condition 2:
  The case of line segment extending beyond a certain amount outside the target shape. This bottom line is not necessary for reproducing the target shape and is therefore excluded from the candidates.

The bottom line candidates are scanned to check if they meet the above conditions through the following algorithm.

Algorithm 1 Bottom line determination algorithm

Require: $\mathcal{R}_{i,j-1} = \{\boldsymbol{r}_{i,j-1,n} \mid n = 1, 2, \ldots, N\}$, Condition 1,Condition 2
Ensure: Bottom lines: $\mathcal{B}_j$
Bottom line candidate: $\boldsymbol{b}$
$k \leftarrow 1$
$n_{\text{left}} \leftarrow 1$
for $n_{\text{right}} = 2$ **to** $N - 1$ **do**
  $\boldsymbol{b} = \boldsymbol{r}_{i,j-1,n_{\text{right}}} - \boldsymbol{r}_{i,j-1,n_{\text{left}}}$
  if $\boldsymbol{b}$ satisfies Contidion 1 $\vee$ Condition 2 **then**
    $\boldsymbol{m}_{\text{left},i,j,k} = \boldsymbol{r}_{i,j-1,n_{\text{left}}}$
    $\boldsymbol{m}_{\text{right},i,j,k} = \boldsymbol{r}_{i,j-1,n_{\text{right}}}$
    $\mathcal{B}$.append($[\boldsymbol{m}_{\text{left},i,j-1,k},\ \boldsymbol{m}_{\text{right},i,j-1,k}]$)
    $k = k + 1$
    $n_{\text{left}} \leftarrow n_{\text{right}}$
  end if
end for
$\mathcal{B}_j$.append($[\boldsymbol{m}_{\text{left},i,j,k},\ \boldsymbol{m}_{\text{right},i,j,k}]$)
return $\mathcal{B}_j$

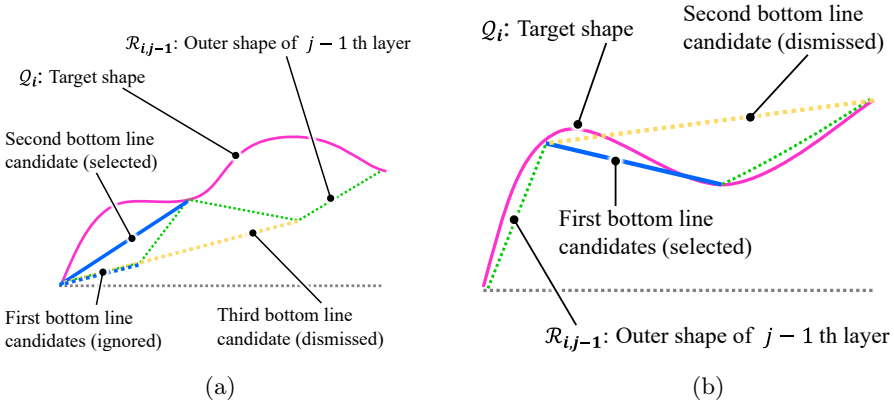


Figure 4.8: Bottom line determine process on jth layer. (a) Condition 1: Overlap inside the previous layer of the outer shape is prohibited. (b) Contidion 2: Protrusion outside the target shape is prohibited.

The blue dotted lines shown in Figs. 4.7(c) and (d) indicate the bottom lines generated for the example shapes. In both examples, the bottom lines of $m_{1,2,1}$, $m_{1,2,2}$, $m_{2,2,1}$, $m_{2,2,2}$ on the second layer are selected to connect the fixed end and the apex of the triangular element of the first layer. These structures are similar to Structure 5 shown in Fig. 4.4. Except for $m_{2,3,2}$, the edges of the triangular elements in the previous layer are selected as the bottom lines on the third layer. These structures are similar to Structure 3 in Fig. 4.4. The bottom line of $m_{2,3,2}$ is selected to connect the apexes of the membranes $m_{2,2,1}$ and $m_{2,2,2}$ on the previous layers. This structure is similar to Structure 4 in Fig. 4.4, indicates that the above algorithm selects the bottom lines that satisfy the connection rules in Fig. 4.4. The right equal sides of $m_{1,2,2}$ and $m_{1,3,2}$ and the left equal sides of $m_{1,3,3}$ extend partially beyond the target shape. Therefore, these were not selected as the bottom line, and no triangular elements were generated in the subsequent layers.

4.4.4 Triangle Height Determination

The heights of the triangles in all layers are determined according to the target shape. This represents an approximation of the shape of the membrane during inflation. This represents an approximation of the membrane shape during inflation. The height of the triangular elements $h_{i,j,k}$ is determined so that the generated isosceles triangular elements occupy as large an area as possible within the target shape region while satisfying the membrane inflation limits based on the bottom line determined in the previous process. The heights of the isosceles triangular elements were increased until the apex $\boldsymbol{m}_{\mathrm{center},i,j,k}$ intersected with the target shape or until it reached the right-angled isosceles triangle, which approximates the membrane shape at the inflation limit. The intersection point between the perpendicular line extending from the midpoint of the bottom line and target shape $\mathcal{Q}_i$ was defined as $\boldsymbol{q}_{cross,i,k}$: Let $hq_{i,n}$ be the distance between

the bottom line and $\boldsymbol{q}_{cross,i,k}$. The height $h_{i,j,k}$ from the bottom line to the vertex $\boldsymbol{m}_{\mathrm{center},i,j,k}$ is determined by the following equation.

$$h_{i,j,k} = min\Big(hq_{i,n},\ \frac{\|\boldsymbol{m}_{\mathrm{right},i,j,k} - \boldsymbol{m}_{\mathrm{left},i,j,k}\|}{2}\Big) \tag{4.4}$$

If the perpendicular distance between $\boldsymbol{m}_{\mathrm{center},i,j,k}$ and $\mathcal{R}_{j-1}$ is less than the threshold value h_s, no valid membrane triangular element is generated. The determination of the bottom lines and triangle heights are repeated until no more triangles are generated. Consequently, the inflated membrane structure for each shape is obtained as a set of triangular elements $\mathcal{M}_i$ that approximates the target shape $\mathcal{Q}_i$.

Figs. 4.7(c) and (d) show the results of triangle height determination for the example shapes. For each of the exsample shapes, two large triangular elements $\boldsymbol{m}_{1,2,1}$, $\boldsymbol{m}_{1,2,2}$, $\boldsymbol{m}_{2,2,1}$, $\boldsymbol{m}_{2,2,2}$ are generated in the second layer. In the third layer, small triangular elements are generated to fill the remaining gaps. The triangular element $\boldsymbol{m}_{2,1,1}$ on the first layer of example shape 2 is generated as a right-angled isosceles triangle because the distance from the bottom line to the target shape exceeds the membrane inflation limit.

4.4.5 Layer Folding

The triangles generated in the previous step are folded to determine the membrane shape in the non-inflated state. After obtaining the inflated membrane structures for each target shapes, the folding process is performed for all triangular elements of $\mathcal{M}_i$. In this process, the triangular element $\boldsymbol{m}_{i,j,k}$ is flattened and transformed into the line segment $\hat{\boldsymbol{m}}_{i,j,k} = [\hat{\boldsymbol{m}}_{\mathrm{left},i,j,k}, \hat{\boldsymbol{m}}_{\mathrm{center},i,j,k}, \hat{\boldsymbol{m}}_{\mathrm{right},i,j,k}]$ shown in Fig. 4.5(a). In the folding of the first layer, $\hat{\boldsymbol{m}}_{i,1,k}$ is determined by the following equation.

$$\hat{\boldsymbol{m}}_{\mathrm{left},i,1,k} = \boldsymbol{m}_{\mathrm{left},i,1,k} \tag{4.5}$$

$$\hat{\boldsymbol{m}}_{\mathrm{right},i,1,k} = \boldsymbol{m}_{\mathrm{right},i,1,k} \tag{4.6}$$

$$\hat{\boldsymbol{m}}_{\mathrm{center},i,1,k} = \frac{\boldsymbol{m}_{\mathrm{right},i,1,k} - \boldsymbol{m}_{\mathrm{left},i,1,k}}{2} \tag{4.7}$$

On the second layer and beyond, folding processes are performed based on the information from the previous folded layer. The polygon $\mathcal{R}_{i,j}$ indicates that the inflated j th layer outer shape is converted into a set of points $\hat{\mathcal{R}}_{i,j}$ arranged on the same straight line by folding. The polygon vertex $\boldsymbol{r}_{i,j-1,n}$, which is selected as $\boldsymbol{m}_{\mathrm{left},i,j,k}$ or $\boldsymbol{m}_{\mathrm{right},i,j,k}$ during bottom line determination, moves to $\hat{\boldsymbol{r}}_{i,j-1,n}$ after folding. The end points of membrane after folding $\hat{\boldsymbol{m}}_{\mathrm{left},i,j,k}$ or $\hat{\boldsymbol{m}}_{\mathrm{right},i,j,k}$ are also moved to $\hat{\boldsymbol{r}}_{i,j-1,n}$. By offsetting in the thickness direction according to the number of layers, the line segment $\hat{\boldsymbol{m}}_{i,j,k}$ that

indicates the folded membrane is determined, as expressed by the following equation:

$$\hat{\boldsymbol{m}}_{\mathrm{left},i,j,k} = \hat{\boldsymbol{r}}_{i,j-1,nl} + \begin{bmatrix} 0 \\ t_m(j-1) \end{bmatrix} \tag{4.8}$$

$$\hat{\boldsymbol{m}}_{\mathrm{right},i,j,k} = \hat{\boldsymbol{r}}_{i,j-1,nr} + \begin{bmatrix} 0 \\ t_m(j-1) \end{bmatrix} \tag{4.9}$$

$$\hat{\boldsymbol{m}}_{\mathrm{center},i,j,k} = \frac{\hat{\boldsymbol{m}}_{\mathrm{right},i,j,k} - \hat{\boldsymbol{m}}_{\mathrm{left},i,j,k}}{2} \tag{4.10}$$

where, t_m donates the membrane thickness; nl and nr are indexes of $\boldsymbol{r}_{i,j-1,n}$ selected as $\boldsymbol{m}_{\mathrm{left},i,j,k}$ and $\boldsymbol{m}_{\mathrm{right},i,j,k}$, respectively. By applying this process to all triangles, the folded membrane structures $\hat{\mathcal{M}}_i$ for each target shape $\mathcal{Q}_i$ are determined.

Figs. 4.7(e) and (f) show the membrane structures for the example shapes. Triangle elements shown in Figs. 4.7(c) and (d) are folded while maintaining the connections between their endpoints.

4.4.6 Layer Integration

The folded membrane structures generated for each shape are then integrated into a single structure. A single folded chamber structure $\hat{\mathcal{M}}_{\mathrm{int}} = \{\hat{\boldsymbol{m}}_{\mathrm{int},j,k} \mid j = 1, \ldots, J,\ k = 1, \ldots, K\}$ that can reproduce multiple target shapes is obtained through the integration process shown in algorithm 2 for folded chamber structures $\hat{\mathcal{M}}_i$, individually designed for target shapes in a previous process.

Algorithm 2 Layer integration algorythm

Require: $\hat{\mathcal{M}}_i$, $\mathcal{M}_i$
Ensure: Integrated structure: $\hat{\mathcal{M}}_{\mathrm{int}}$, Inflated Shape: $\mathcal{M}_{\mathrm{int}}$

```
M̂_int = M̂_1
for i = 2 to I do
  for j = 1 to J do
    for k = 1 to k do
      if m̂_int,j,k = m̂_i,j,k then
        m_int,j,k = m_i,j,k
      else if When m̂_int,j,k and m̂_i,j,k overlap partially then
        m̂_int,j+1,k = m̂_i,j,k
        m_int,i,j+1,k = m_i,j,k
      else
        M̂_int.append(m̂_i,j,k)
        M_int.append(m_i,j,k)
      end if
    end for
  end for
end for
return M̂_int, M_int
```

Among the line segments contained in $\hat{\mathcal{M}}_i$, those that have the same shape regardless of the target shape are added to $\hat{\mathcal{M}}_{\text{int}}$. The line segments with structure differing depending on their shape are added as a new line segment above the existing layer to $\hat{\mathcal{M}}_{\text{int}}$. The folded membrane structure after being integrated into $\hat{\mathcal{M}}_{\text{int}}$ inflates to $\mathcal{M}_{\text{int}} = \{\boldsymbol{m}_{\text{int}} \mid i = 1, \ldots, I,\ j = 1, \ldots, J,\ k = 1, \ldots, K\}$ in reference to the inflated shape before integration.

Fig. 4.7(g) shows an integrated folded membrane structure for reproducing the example shapes. Four pairs of line segments, $\hat{\boldsymbol{m}}_{1,1,1}$ and $\hat{\boldsymbol{m}}_{2,1,1}$, $\hat{\boldsymbol{m}}_{1,2,1}$ and $\hat{\boldsymbol{m}}_{2,2,1}$, $\hat{\boldsymbol{m}}_{1,2,2}$ and $\hat{\boldsymbol{m}}_{2,2,2}$, $\hat{\boldsymbol{m}}_{1,3,1}$ and $\hat{\boldsymbol{m}}_{2,3,1}$ are shown in Figs. 4.7(e) and (f), as the same structure. These are integrated as $\hat{\boldsymbol{m}}_{\text{int},1,1}$, $\hat{\boldsymbol{m}}_{\text{int},2,1}$, $\hat{\boldsymbol{m}}_{\text{int},2,2}$, and $\hat{\boldsymbol{m}}_{\text{int},3,1}$ through the layer integration process. $\hat{\boldsymbol{m}}_{1,3,2}$ and $\hat{\boldsymbol{m}}_{1,3,3}$ exist in the same layer as $\hat{\boldsymbol{m}}_{2,3,2}$ and at the same position, but have different structures. Therefore, the fourth layer is newly generated, and $\hat{\boldsymbol{m}}_{2,3,2}$ is added to it as $\hat{\boldsymbol{m}}_{\text{int},4,1}$. Note that $\hat{\boldsymbol{m}}_{2,3,3}$ is a line segment generated only for example shape 2; however there is no line segment in the corresponding location of the folded membrane structure for example shape 1. Therefore, it is added as a new line segment $\hat{\boldsymbol{m}}_{\text{int},3,4}$. The layer integration process confirmed that two folded membrane structures, each consisting of three layers and six membranes individually designed for example shapes, were integrated into a single folded membrane structure with eight membranes and four layers.

Figs. 4.7(h) and (i) show the shapes of the integrated membrane structure when inflated. To conveniently illustrate, each layer is offset vertically by the thickness of the membrane. $\boldsymbol{m}_{\text{int},4,1}$, which is not used in example shape 1, and $\boldsymbol{m}_{\text{int},3,2}$ and $\boldsymbol{m}_{\text{int},3,3}$, which are not used in example shape 2, are subjected to a negative pressure. As a result, following the behavior shown in Fig. 4.4 when negative pressure is applied, the upper layer adheres to the lower layer and transmits the deformation of the lower layer to the surface.

In this study, the actuator is assumed to be two-dimensional and extends indefinitely in the depth direction. When converting a designed two-dimensional structure into a three-dimensional structure, sufficient depth should be ensured in the actual PSA-LM during design so that pseudo-two-dimensionality can be maintained.

4.5 Internal Pressure Design

4.5.1 Overview of Pressure Design

The internal pressure pattern was designed according to two processes. In the first process, the initial internal pressure pattern $\boldsymbol{p}_{\text{init}}$ is calculated using an analysis model of membrane displacement that does not consider the interaction between other membranes. In the second process, FEA optimization using $\boldsymbol{p}_{\text{init}}$ as the initial value is performed, and the optimized internal pressure pattern $\boldsymbol{p}_{\text{opt}}$ that can reproduce the target shape is determined. Each step is detailed below.

4.5.2 Initial Internal Pressure Pattern Calculation

Fig. 4.9 shows the membrane displacement-pressure model. This model indicates the inflated membrane shape as an arc. The radius of the arc ρ_1 and the center displacement υ are expressed by the following equations:

$$\rho_1 = \frac{\rho_0\,\varepsilon_0}{\sin\phi} \tag{4.11}$$

$$\upsilon = \rho_1\big(1-\cos\phi\big) \tag{4.12}$$

where ρ_0 is half the initial membrane width; ε_0 is prestretch ratio; ϕ is the angle of the arc. The entire elongation ratio of the membrane ε_1 is defined by the following equation:

$$\varepsilon_1 = \frac{\rho_1\,\phi}{\rho_0} = \frac{\varepsilon_0\,\phi}{\sin\phi} \tag{4.13}$$

The nonlinear stress σ that inflates the membrane is expressed by the uniaxial tensile stress of the Ogden model[91], as shown in the following equation:

$$\sigma = \sum_{i=1}^{N} \mu_i\big(\lambda_1^{\gamma_i} - \lambda_1^{-\gamma_i}\big) \tag{4.14}$$

where μ_i and γ_i are material constants in the Ogden model and λ_1 is the uniaxial stretch ratio. Assuming equal volume, τ_1 varies directly with the initial membrane thickness τ_0 and inversely with elongation ratio ε_1, as expressed by the following equation:

$$\tau_1 = \frac{\tau_0}{\varepsilon_1} \tag{4.15}$$

The internal pressure is determined by the following equation based on a geometric relationship and Laplace's law for thin membranes.

$$p = \frac{\sigma\tau_1}{\rho_1} = \frac{\sigma\tau_0 sin^2\phi}{\rho_0\varepsilon_0^2\phi} \tag{4.16}$$

Although ϕ can be found by solving a set of nonlinear equations consisting of (4.12) and (4.16), obtaining an analytical solution is difficult. Therefore, ϕ must be determined iteratively using a numerical solution method.

The initial pressure pattern $\boldsymbol{p}_{\text{init}}$ is calculated by applying the above model to all the designed triangular elements. The initial elongation ratio ε_0 is expressed as follows:

$$\varepsilon_0 = \frac{l_{i,j,k}}{\hat{l}_{i,j,k}} \tag{4.17}$$

where, $l_{i,j,k}$ is the length of the membrane when not inflated and $\hat{l}_{i,j,k}$ is the bottom line length when inflated, as shown in Fig. 4.5. The membrane thickness τ_0 is given as

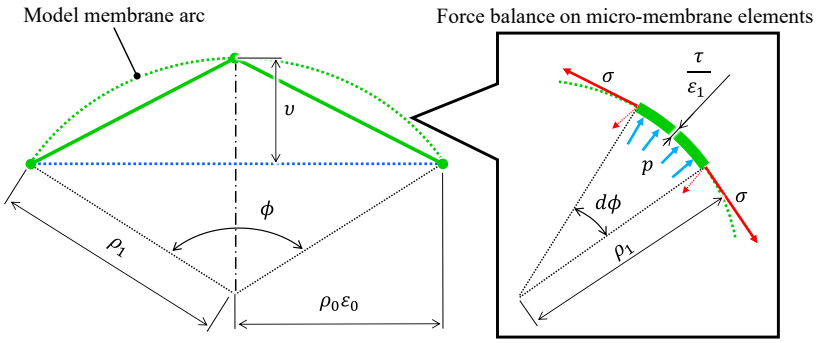


Figure 4.9: Membrane analysis model. The membrane shape is represented with arcs based on Laplace's law.

the sum of its own membrane thickness and that of the layer stacked on top of it, by the following equation:

$$\tau_0 = t(J - j) \tag{4.18}$$

where J is the maximum layer number of the designed structure, and j is the layer number index of the observed membrane. The center displacement υ is given by the height of the triangle $h_{i,j,k}$. Substituting these values, the internal pressure for the triangular element is obtained.

4.5.3 Bayesian Optimization

The initial internal pressure pattern $\boldsymbol{p}_{\text{init}}$, calculated using the membrane model, does not consider factors such as membrane-to-membrane interactions that occur in the actual PSA-LM. To correct the errors caused by these factors, the internal pressure pattern was optimized using FEA; however, FEA evaluations are computationally expensive. Therefore, Bayesian optimization[92] which can converge with a small number of trials was used.

In this study, Bayesian optimization was implemented using the `gp_minimize` function of the scikit-optimize library (`skopt`)[93] in Python. The internal pressure pattern $\boldsymbol{p}_i$ which is optimized for each target shape Ω_i is defined as follows:

$$\boldsymbol{p}_i = [p_{i,1}, p_{i,2}, \ldots, p_{i,m}]^T \tag{4.19}$$

The similarity between the target and FEA shapes was evaluated using Intersection over Union (IoU). IoU is an indicator that represents the degree of overlap between the FEA shape $\Omega_{\text{FEA}}(\boldsymbol{p}_i)$ and the target shape Ω_i and is defined as follows:

$$\text{IoU}(\boldsymbol{p}_i) = \frac{\left|\Omega_i \cap \Omega_{\text{FEA}}(\boldsymbol{p}_i)\right|}{\left|\Omega_i \cup \Omega_{\text{FEA}}(\boldsymbol{p}_i)\right|} \leq 1 \tag{4.20}$$

During the optimization process, the internal pressure pattern $\boldsymbol{p}_i$ that maximizes IoU is searched for within a specified number of evaluations. To improve the search efficiency,

ten initial pressure patterns that randomized $\boldsymbol{p}_{\text{init}}$ by 10 % were used. The internal pressure design process was completed when the internal pressure pattern $\boldsymbol{p}_{\text{opt}}$ was obtained through Bayesian optimization.

4.6 PSA-LM Fabrication

Fig. 4.10 shows the fabrication processes of PSA-LM. Fig. 4.10(a) depicts the silicone rubber curing process. First, sheet fixing parts are attached to both ends of the housing. The uncured silicone rubber is poured onto the stacked chamber molding sheet and sheet fixing parts, following which, it is placed in a temperature-controlled chamber and maintained at an internal temperature of 50 ° C for one hour to cure the rubber. Fig. 4.10(b) shows the process for removing the chamber molding sheet. First, the sheet fixing parts are removed. Next, the ribs used to fix the chamber molding sheets are disconnected. Finally, the remaining sheets from the silicone rubber. The space left under the membrane functions as a chamber. Fig. 4.10(c) shows the process for sealing both ends. First, the side cover with the air tubing is attached to one end of the housing. At which point, uncured silicone rubber is poured into the side cover to seal the open membrane end. After the silicone rubber is cured, the other side cover is attached to the other end using the same procedure. The PSA-LM fabrication process is complete once the silicone rubber is cured and both ends are sealed.

4.7 Experiment

4.7.1 Overview of the Experiment

To confirm the effectiveness of the proposed method, it was applied to the five asymmetrical target shapes shown in Fig. 4.11. These target shapes include not only the dorsal tongue shapes with up to two peaks observed in previous studies[14,15,25], but also shapes with three to four peaks that were defined to accommodate more complex manipulations in the future. Membrane structures and internal pressure patterns were designed to reproduce each target shape. The design results were evaluated through FEA simulation and an actual PSA-LM. The material constants of the Ogden model used in FEA and $\boldsymbol{p}_{\text{init}}$ calculations are described in Appendix B, along with the methods used for estimating them. The actual PSA-LM was manufactured from silicone rubber (Dragon Skin 10 NV, Smooth-on, Inc., USA) which was cured by additional polymerization using platinum as a catalyst. The membrane thickness t was set to 1.5 mm, and the threshold value h_s for the termination of triangule generation was set to 1.5 mm.

4.7.2 Result of Structural Design for Five Shapes

The designed inflated membrane structures are shown in Fig. 4.12. The root mean square errors (RMSEs) of each target shape and the designed outer shapes of inflated membrane structure were within 1 mm, confirming that the target shapes were accurately reproduced. The designed folded membrane structure is shown in Fig. 4.13. In

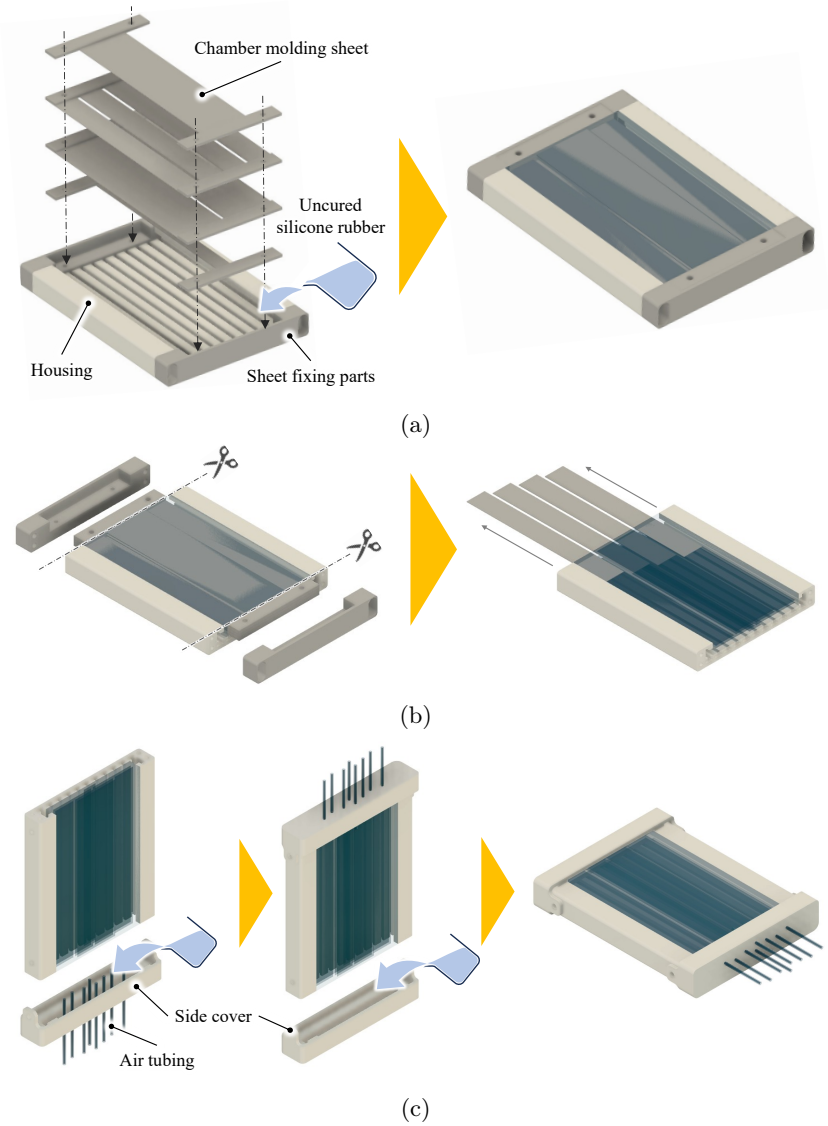


Figure 4.10: PSA-LM fabrication processes (a) Step 1: Curing the silicone rubber. (b) Step 2: Remove the chamber mold sheet. (c) Step 3: Seal the ends.

this experiment, a structure consisting of three layers and eleven membranes was designed. Fig. 4.13(a) shows the line segments that indicate a folded membrane structure. Fig. 4.13(b) shows the actual structure of the designed PSA-LM. Fig. 4.13(c) shows the appearance of the actual PSA-LM.

4.7.3 Result of the Internal Pressure Design for Five Shapes

Table 4.1 lists the initial internal pressure $\boldsymbol{p}_{\text{init}}$ calculated through the process described in Section 4.5.2. A negative pressure of -20 kPa was uniformly applied to the unused

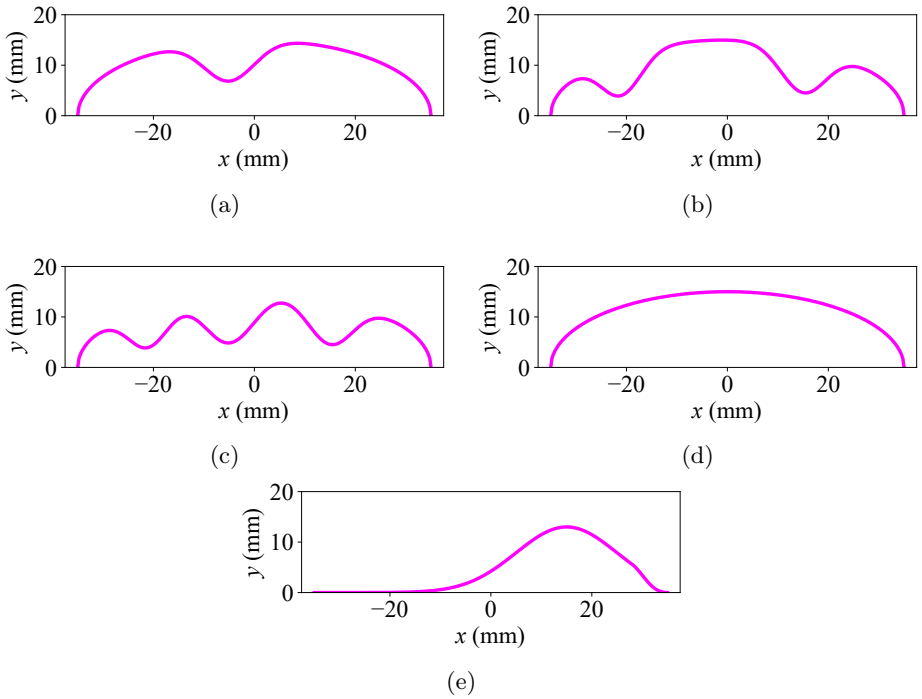


Figure 4.11: Five target shapes with one to four peaks were selected. (a) Shape i-i. (b) Shape i-ii. (c) Shape i-iii. (d) Shape i-iv. (e) Shape i-v.

membranes.

Fig. 4.14 shows the FEA results when $\boldsymbol{p}_{\text{init}}$ was applied. The position and number of peaks in the target shape were mostly reproduced, but the displacements were approximately twice those in the target shapes.

Table 4.2 lists the optimized internal pressure pattern $\boldsymbol{p}_{\text{opt}}$. Overall, the internal pressure values $\boldsymbol{p}_{\text{opt}}$ are lower than $\boldsymbol{p}_{\text{init}}$. The maximum internal pressure value of $\boldsymbol{p}_{\text{init}}$ is 55.8 kPa, whereas the maximum value of $\boldsymbol{p}_{\text{opt}}$ has decreased to 23.7 kPa. In particular, the decrease in internal pressure values in the first layer is significant. Internal pressure values $\boldsymbol{p}_{\text{init},1,k}$ range from 40 to 55 kPa, whereas $\boldsymbol{p}_{\text{opt},1,k}$ values range from 0 to 11 kPa. This indicates that less pressure was required because the reaction force associated with inflating the upper membrane pulled up the lower membrane at the membrane-to-membrane connection point.

Fig. 4.15 shows the FEA shape when $\boldsymbol{p}_{\text{opt}}$ was applied. The displacement of the FEA shape is suppressed due to the reduction in internal pressure that occurred during optimization, which improved the reproducibility of the target shape. The FEA shapes qualitatively match the target shapes, and the $RSME_{target-FEA}$ between the two are within the range of 0.89-1.71 mm. The side peaks of the three-peak shape and all the peaks of the four-peak shape became flatter, as shown in Figs. 4.15(b) and (c). This is attributed to the structural design process not considering the bending moments. The

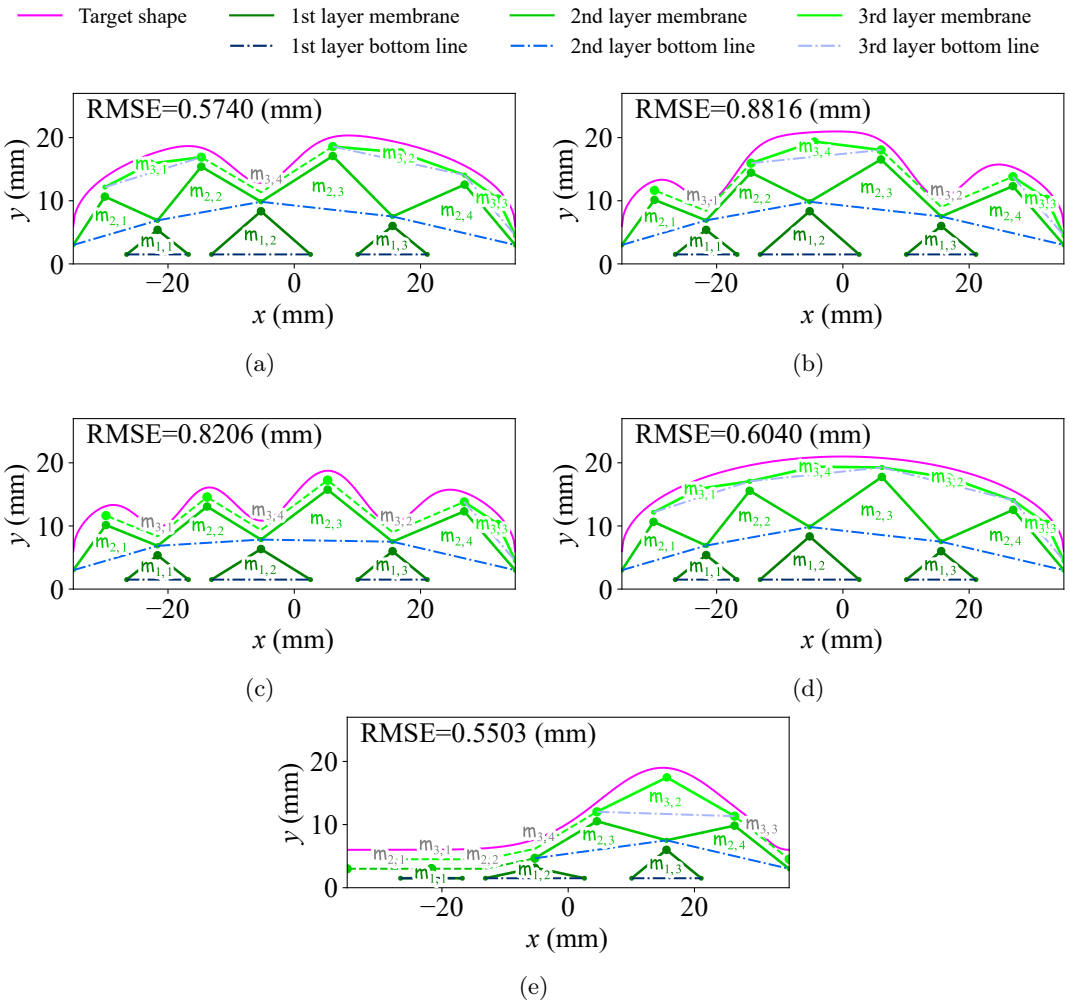


Figure 4.12: Target shapes expressed as triangles. (a) Shape i-i. (b) Shape i-ii. (c) Shape i-iii. (d) Shape i-iv. (e) Shape i-v.

bending moment effect was significant when the membrane thickness was large compared to its width. This can be seen in the convex part of Shape i-iii in Fig. 4.15(c). Designing an inflated structure that accounts for bending moments and imposing restrictions on the thickness-to-width ratio of the membrane may mitigate this. At present, the height of the triangles generated during the structural design process is constrained solely by the expansion limit of the analytical model for the membrane. In addition to this constraint, further limitations based on the angles between adjacent edges and the aspect ratio of the membrane could be introduced. By approximating the blunting of angles caused by bending moments, this approach may enable the designed inflated membrane structures to replicate the actual deformation behavior more closely. Modifying the method to allow negative pressure to be applied during optimization would increase

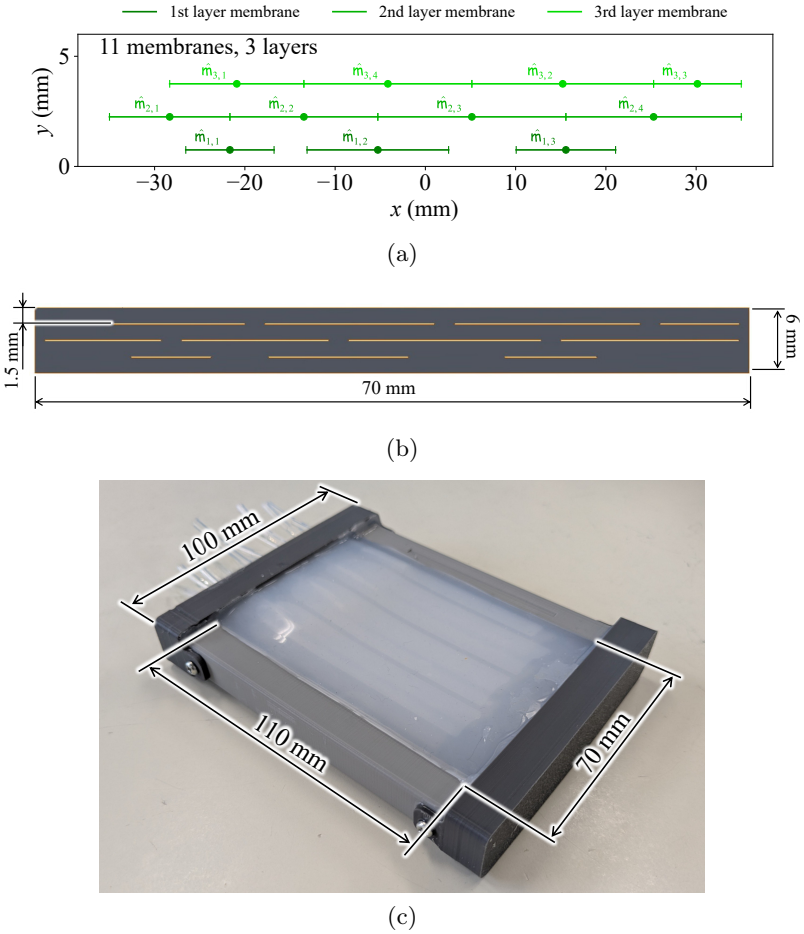


Figure 4.13: Designed structure. (a) Line segments of folded membrane structure. (b) Actual PSA-LM structure. (c) Appearance of actual PSA-LM.

the traction force at the concave point, potentially improving the reproducibility of the target shape.

The red dots in Fig. 4.15 show the measurement results of the actual PSA-LM shape when $\boldsymbol{p}_{\text{opt}}$ was applied. Fig. 4.16 shows the actual appearance of the actual PSA-LM. These surface shapes were obtained by horizontally scanning laser displacement sensor (OPTEX FA Inc., repeatability accuracy 45 μm) using a motorized linear slider. These two figures show that the shape of the actual PSA-LM qualitatively reproduces the target shapes, which suggests that the proposed method can design structures and internal pressures that can reproduce the target shape to a certain extent, even in an actual PSA-LM. However, as shown in Figs. 4.15(b) and (c), the unevenness of Shapes i-ii and i-iii became even less pronounced. This resulted in a decrease in the reproducibility of the target shape. This error possibly occurred because the Ogden model parameters were estimated based only on the results of uniaxial tensile and pure shear

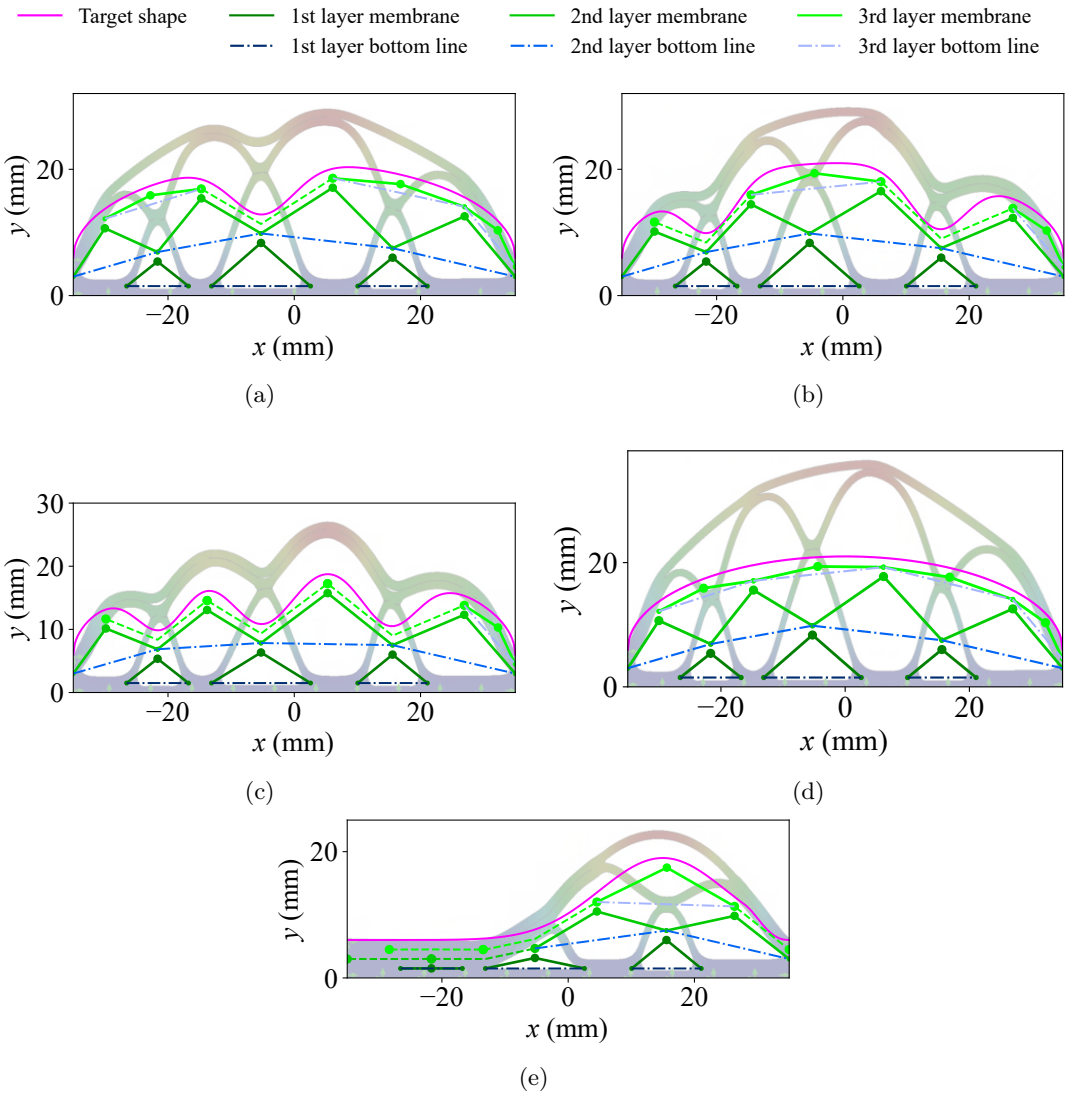


Figure 4.14: FEA results with $\boldsymbol{p}_{\text{init}}$ applied. (a) Shape i-i. (b) Shape i-ii. (c) Shape i-iii. (d) Shape i-iv. (e) Shape i-v.

tests. In general, parameter estimation for the Ogden model employs uniaxial tensile, pure shear, and equi-biaxial tensile tests. However, because equi-biaxial tensile testing requires specialized experimental equipment, it was omitted in this study. As a result, errors in the material model ' s behavior under deformation modes close to equi-biaxial tensile may have arisen, potentially leading to increased inaccuracies or even divergence in the computations. Conducting additional equi-biaxial tensile tests and incorporating the obtained data into the parameter estimation is expected to improve the shape consistency between FEA and actual PSA-LM and target shape reproducibility in the actual PSA-LM.

Table 4.1: Initial internal pressure pattern $\boldsymbol{p}_{\text{init}}$ values.

$\boldsymbol{p}_{\text{init}}$ (kPa)	Shape				
	i-i	i-ii	i-iii	i-iv	i-v
$p_{\text{init},1,1}$	55.8	55.8	54.8	55.8	0.00
$p_{\text{init},1,2}$	41.0	41.0	21.4	41.0	1.50
$p_{\text{init},1,3}$	52.2	52.2	52.1	52.2	52.2
$p_{\text{init},2,1}$	33.5	28.6	28.8	33.5	-20.0
$p_{\text{init},2,2}$	26.2	20.3	17.5	27.3	-20.0
$p_{\text{init},2,3}$	18.2	16.1	16.7	20.8	5.03
$p_{\text{init},2,4}$	17.9	16.9	16.9	17.9	7.37
$p_{\text{init},3,1}$	1.24	-20.0	-20.0	1.16	-20.0
$p_{\text{init},3,2}$	0.52	-20.0	-20.0	0.39	5.43
$p_{\text{init},3,3}$	6.74	7.12	7.12	6.74	-20.0
$p_{\text{init},3,4}$	-20.0	1.80	-20.0	0.87	-20.0

Table 4.2: Optimized internal pressure pattern $\boldsymbol{p}_{\text{opt}}$ values.

$\boldsymbol{p}_{\text{opt}}$ (kPa)	Shape				
	i-i	i-ii	i-iii	i-iv	i-v
$p_{\text{opt},1,1}$	10.9	1.97	5.97	13.3	6.95
$p_{\text{opt},1,2}$	0.00	4.70	2.64	7.68	0.43
$p_{\text{opt},1,3}$	20.0	0.00	4.07	11.3	12.9
$p_{\text{opt},2,1}$	17.4	14.2	23.7	12.7	-20.0
$p_{\text{opt},2,2}$	13.3	10.7	6.19	9.94	-20.0
$p_{\text{opt},2,3}$	5.97	11.1	8.39	7.13	1.57
$p_{\text{opt},2,4}$	7.17	7.56	9.22	6.46	5.63
$p_{\text{opt},3,1}$	0.00	-20.0	-20.0	0.97	-20.0
$p_{\text{opt},3,2}$	1.40	-20.0	-20.0	0.07	3.53
$p_{\text{opt},3,3}$	5.52	0.00	11.2	3.08	-20.0
$p_{\text{opt},3,4}$	-20.0	0.00	-20.0	0.00	-20.0

4.8 Reproduction of Tongue-like Shapes and Comparison with PSA-AC

To apply this design method to tongue robots, the method in this chapter was used to reproduce tongue-like target shapes, which were compared with those of the method in Chapter 3.

As shown in Fig. 4.17, eight target shapes were used, comprising four basic forms: ellipsoidal, concave, one-sided convex, and crevasse. Each form had two variants, with maximum heights of 15 and 30 mm.

Previous studies have reported that the width of the palatal crown is 42 $\pm$ 0.92 mm, and the maximum distance between the tongue and palate is 16.5 mm[94]. In this experiment, the width and maximum height of the target shape were set to 70 and 30

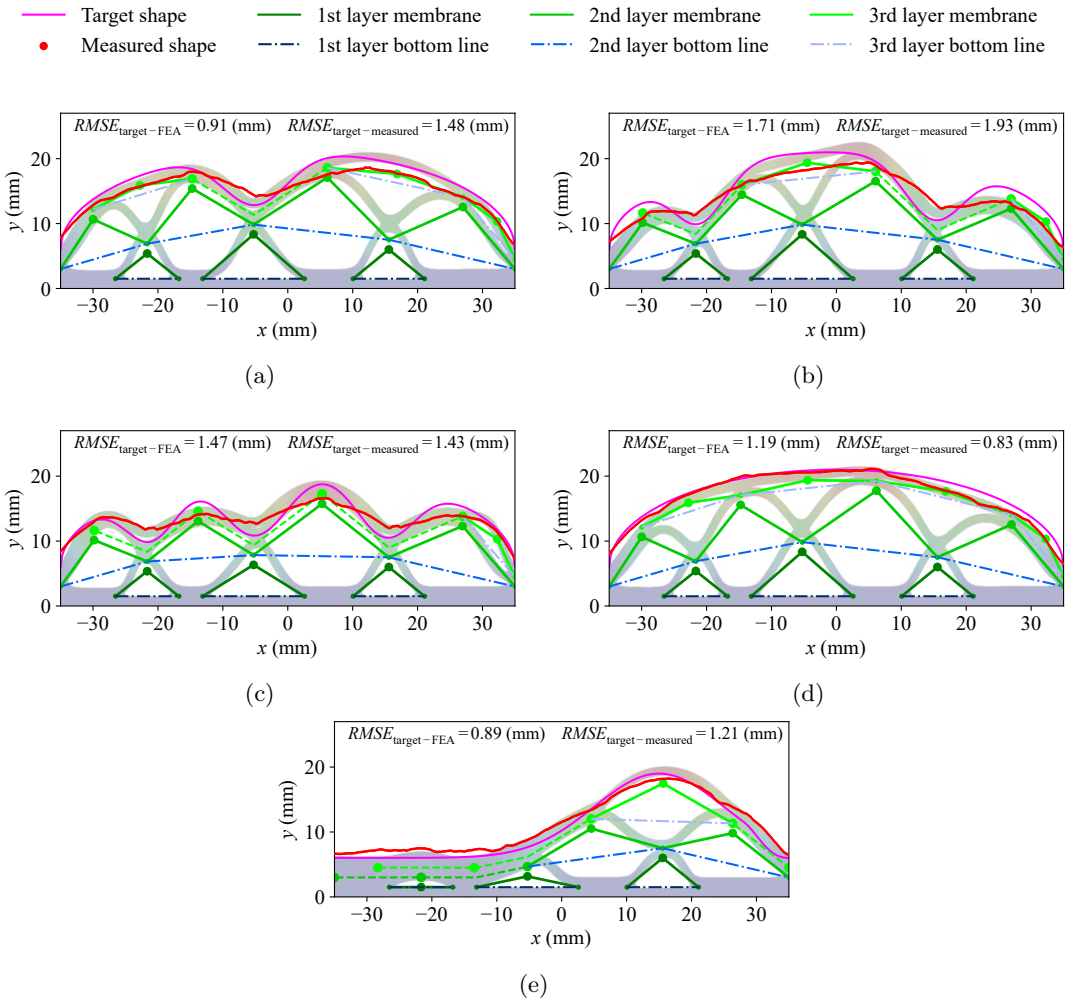
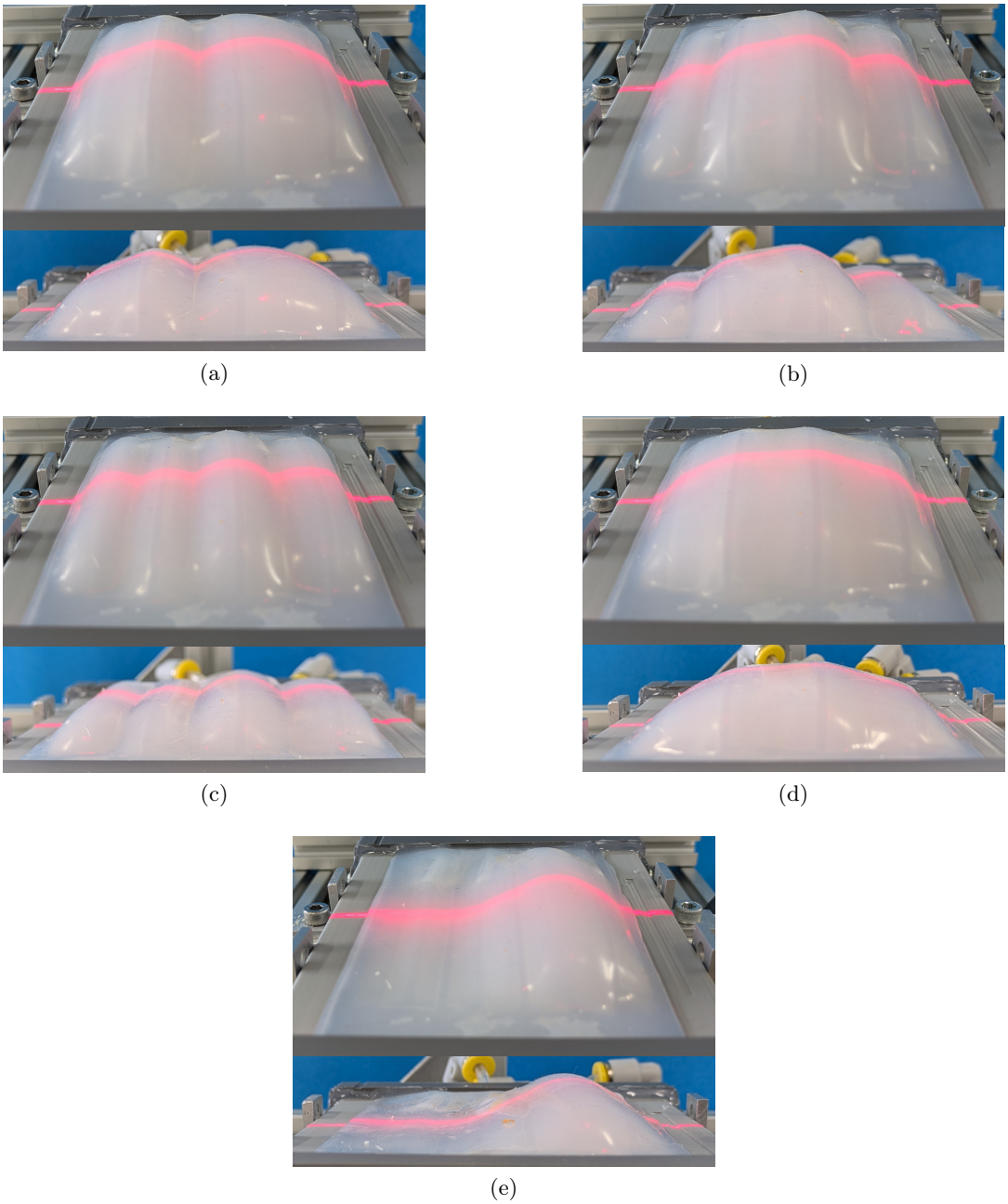


Figure 4.15: FEA shapes and actual PSA-LM surface shapes when $\boldsymbol{p}_{\text{opt}}$ is applied. (a) Shape i-i. (b) Shape i-ii. (c) Shape i-iii. (d) Shape i-iv. (e) Shape i-v.

mm, respectively. These dimensions were based on a model twice the size of a human tongue. For comparison, the internal pressure patterns that produce the same target shapes were determined using in Chapter 3 with PSA-AC, which has a predetermined, uniform structure. The differences between the methods described in Chapter 3 and 4 were evaluated through FEA simulations.

Fig. 4.18(a) shows the structure of the PSA-AC used. This structure is identical to that used in Chapter 3 method and was predetermined based on designer rules of thumb. Fig. 4.18(b) shows the structure of the four layers with eight membranes the PSA-LM designed using the proposed method. In the PSA-LM design, the membrane thickness was set to $t = 1.5$ mm, and the threshold value for triangular generation termination h_s was set to 2 mm. h_s was adjusted to make the number of chambers the



(a) (b) (c) (d) (e)

Figure 4.16: Appearance of the actual PSA-LM shape when $\boldsymbol{p}_{\text{opt}}$ is applied. (a) Shape i-i. (b) Shape i-ii. (c) Shape i-iii. (d) Shape i-iv. (e) Shape i-v.

same as that of PSA-AC, that is eight chambers. The pressure values for PSA-AC and PSA-LM are presented in Table 4.3 and Table 4.4, respectively.

Fig. 4.19 shows the RMSE for each shape. The method in this chapter achieved

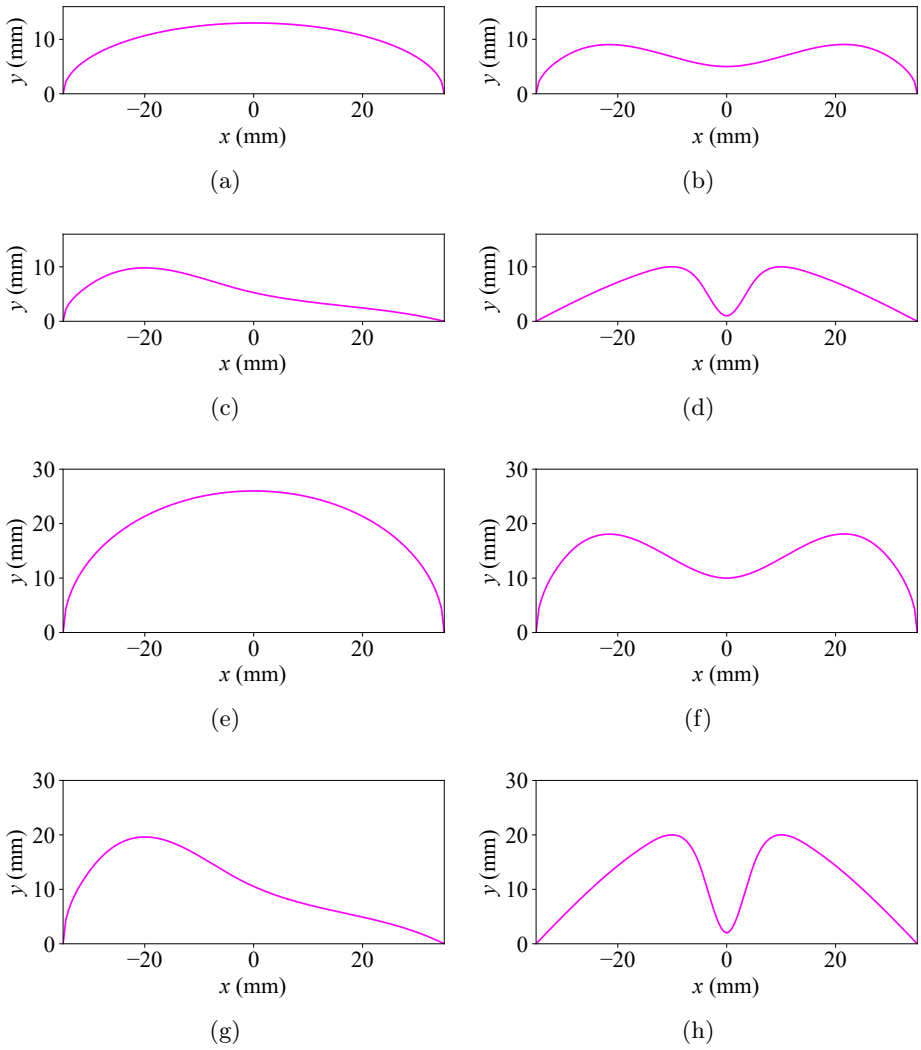


Figure 4.17: Target shapes for the human tongue. (a) Shape ii-i: ellipsoidal shape. (b) Shape ii-ii: concave shape. (c) Shape ii-iii: one-sided convex shape. (d) Shape ii-iv: crevasse shape. (e-h) Shape ii-v, ii-vi, ii-vii , ii-viii: shapes with twice the maximum height of the previous four shapes.

higher accuracy than the method in Chapter 3 for most target shapes. The RMSE of the method in this chapter ranges from 0.9 to 3.5 mm, whereas that of the method in Chapter 3 ranges from 1.1 to 4.5 mm. This result confirms that the method in this chapter consistently suppresses shape reproduction errors more effectively than the method in Chapter 3.

Fig. 4.20 shows individual comparisons for each target shape. The PSA-LM designed using the method in this chapter reproduced all target shapes qualitatively. PSA-AC also mostly reproduced the target shape, but the reproduction accuracy was significantly

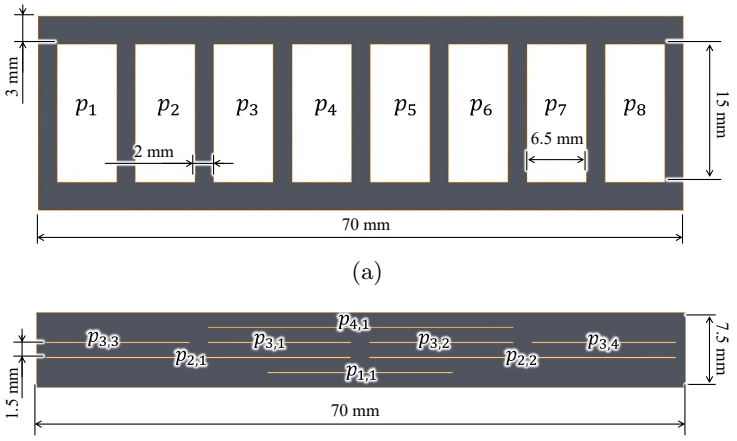


Figure 4.18: Actuator structures and chamber/membrane indices for reproducing tongue-like shapes. (a) PSA-AC structure used in Chapter 3. (b) PSA-LM structure that automatically designed by the method in this chapter.

Table 4.3: Internal pressure values for PSA-AC.

p_i	Shape							
(kPa)	ii-i	ii-ii	ii-iii	ii-iv	ii-v	ii-vi	ii-vii	ii-viii
p_1	6.34	12.1	11.9	13.6	1.38	25.1	22.2	7.27
p_2	25.5	21.5	23.2	2.89	50.6	40.6	44.3	20.7
p_3	20.4	12.5	14.6	30.1	42.2	27.0	31.9	49.6
p_4	25.7	9.33	12.7	1.28	51.2	18.3	23.8	3.90
p_5	25.9	9.54	0.67	2.21	52.3	19.6	15.1	10.3
p_6	20.1	12.2	0.69	28.5	40.8	25.3	12.2	47.5
p_7	25.9	22.0	0.30	5.95	51.8	42.8	8.51	21.2
p_8	6.27	12.0	0.30	10.7	2.61	21.9	4.53	6.68

Table 4.4: Internal pressure values for PSA-LM.

$p_{i,j}$	Shape							
(kPa)	ii-i	ii-ii	ii-iii	ii-iv	ii-v	ii-vi	ii-vii	ii-viii
$p_{1,1}$	15.0	0.00	2.92	0.05	24.4	0.00	18.0	25.0
$p_{2,1}$	2.04	2.01	1.98	17.4	30.0	20.1	30.6	14.6
$p_{2,2}$	2.01	2.01	0.00	17.3	30.0	19.7	0.23	14.0
$p_{3,1}$	-20.0	-20.0	-20.0	5.15	-20.0	-20.0	-20.0	25.0
$p_{3,2}$	-20.0	-20.0	-20.0	4.87	-20.0	-20.0	-20.0	25.0
$p_{3,3}$	2.59	5.31	9.35	-20.0	-20.0	35.0	-20.0	-20.0
$p_{3,4}$	2.56	5.54	-20.0	-20.0	-20.0	35.0	-20.0	-20.0
$p_{4,1}$	0.21	-20.0	-20.0	-20.0	14.0	-20.0	-20.0	-20.0

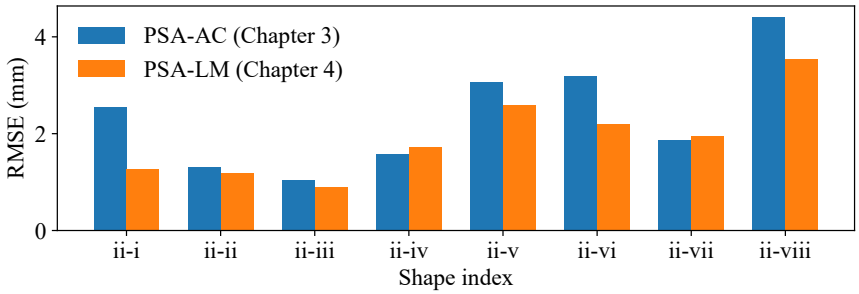


Figure 4.19: RMSEs of the methods in Chapter 3 and 4.

reduced for shapes with extreme concavities, such as Shapes ii-iv and ii-viii shown in Figs. 4.20(d) and (h), respectively. PSA-LM was not good at reproducing the central concavity although it clearly improved reproduction accuracy in other areas compared to the method in Chapter 3.

As shown in Fig. 4.20(g), the RMSE of the method in this chapter was higher than that of the method in Chapter 3. This is believed to be due to slight over-expansion at the vertex. No significant differences exist in other areas. Therefore, it can be concluded that the error falls within the acceptable range. Furthermore, PSA-AC exhibited local convex deformation in all target shapes due to the inflation of its surface membrane. In contrast, the PSA-LM achieved a smoother surface shape owing to its relatively wide membrane width. These results demonstrate the superiority of the method presented in this chapter, which designs both the structure and the internal pressure patterns through an inverse-problem-based approach, over the method in Chapter 3 that designs only the internal pressure patterns.

The detailed behavior during deformation can be observed in Figs. 4.21(a) and (b), which respectively show the strain distribution of the FEM results of PSA-AC and PSA-LM when reproducing Shape ii-v, which was the example with the highest average internal pressure. As shown in the figure, the PSA-AC exhibited significant strain concentration on the inner wall, with values exceeding 1 in many areas. In contrast, PSA-LM suppressed the strain to approximately 0.4, which prevented localized deformation. These results indicate that PSA-LM poses a lower burst risk than PSA-AC. Furthermore, the structure composed of layered membranes has a structural advantage that enables more efficient surface-shape generation than a structure that uses rectangular chambers as its minimum elements.

4.9 Conclusion

In this chapter, a novel pneumatic soft actuator for generating diverse surface shapes and its structural and internal pressure pattern design methods were presented. In summary,

- A type of soft actuator called PSA-LM, which can express various surface shapes

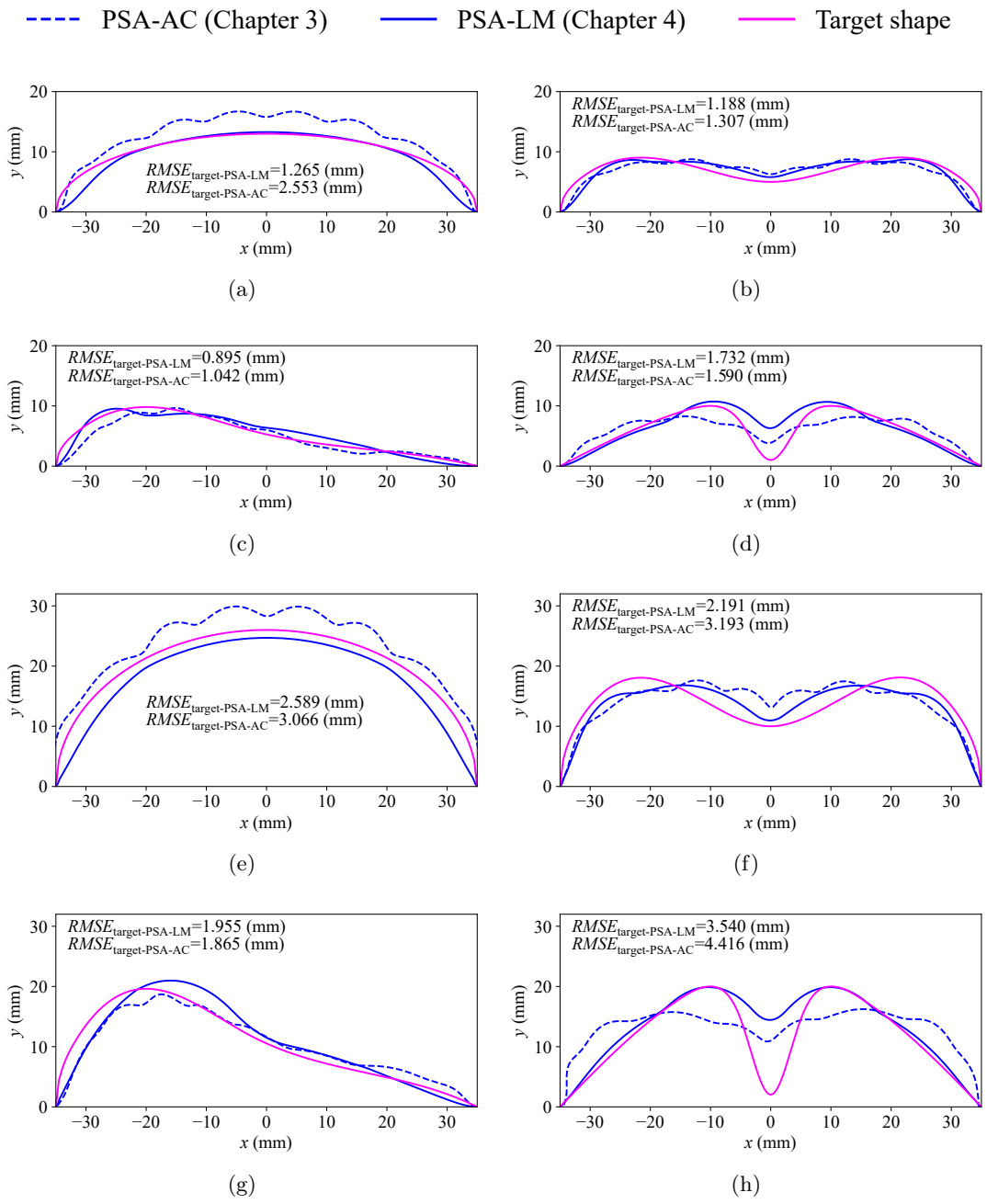
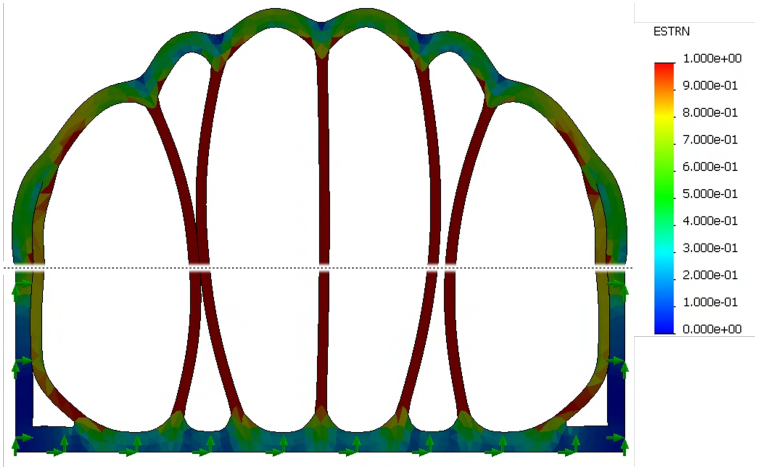
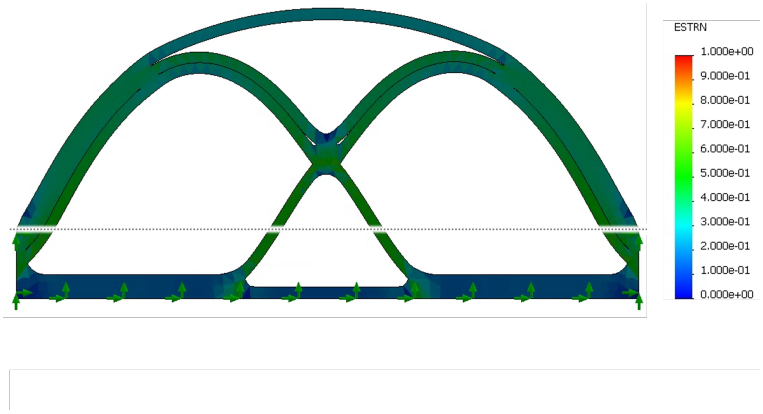


Figure 4.20: Comparison of target and FEA shapes. (a) Shape ii-i. (b) Shape ii-ii. (c) Shape ii-iii. (d) Shape ii-iv. (e) Shape ii-v. (f) Shape ii-vi. (g) Shape ii-vii. (h) Shape ii-viii.



(a)



(b)

Figure 4.21: Strain distribution of (a) PSA-AC and (b) PSA-LM in Shape ii-v.

using layered elastic membranes, was proposed. Its structure can be easily approximated geometrically, which enables systematic and comprehensive design to achieve given multiple target shapes using simple algorithms.

- A design method was proposed for PSA-LM structures, using a geometric approximation to express the shape of the membranes during inflation as stacked isosceles triangles.
- A method was proposed for the design of internal pressure patterns, using Bayesian optimization with FEA for the designed structure. An elastic membrane inflation analysis model was used to improve the search efficiency of the optimization by setting the initial internal pressures.
- The proposed method was applied to five shapes with one to four peaks, successfully producing a structure and internal pressure patterns that reproduced the target shapes with RMSEs of approximately 1 mm.

- The results of using the proposed and conventional methods were compared in reproducing eight tongue-like target shapes. The average RMSEs for the proposed and conventional methods were 1.91 mm and 2.38 mm, respectively, confirming that the proposed method demonstrated higher accuracy.

Chapter 5

Conclusion

5.1 Summary

This dissertation aimed to realize a pneumatic soft actuator(PSA) with variable surface shapes through the proposal of a novel structure and the establishment of a inverse-problem-based design framework. Conventional PSAs primarily perform simple active deformations such as bending or contraction. However, developing new PSAs capable of producing more complex surface deformations can significantly enhance the performance and broaden the applicability of soft robotic system. Because PSAs with variable surface shapes possess a high degree of design freedom, a forward-problem-based approach that relies on empirical adjustments to existing structures is not suitable. In addition, the structural requirements that fundamentally enable variable surface shapes have not yet been clarified. To address this, we prototyped several PSAs with different structures and compared their behaviors to identify the essential design features for realizing PSAs with variable surface shapes. At the same time, an inverse-problem-based design framework was adopted, which derives both structural and internal pressure parameters from target surface shapes and enables the systematic determination of optimal structural parameters and control inputs. Such design methodology and actuator concept are particularly effective for tongue robots for *in vitro* mastication, which must generate diverse surface shapes that vary among individuals. In this dissertation, the development of PSAs with variable surface shapes and the corresponding design framework were carried out with the tongue robot as the primary application case.

Chapter 1 described the background and objectives of this dissertation and clarified the position of the present study relative to conventional tongue robots and related design methodologies.

Chapter 2 presented a single-chamber PSA capable of pressing deformable objects against a rigid palate as an example of a forward-problem-based design for a tongue robot. Its surface shape was estimated in real time using camera-captured concentric patterns, achieving sufficient accuracy except for highly curved objects. Forming and pressing experiments confirmed its ability to manipulate viscoelastic materials and estimate their mechanical parameters. These results demonstrated the feasibility of tongue

robots for *in vitro* mastication and highlighted both the integration of sensing functions and the limitations of simple forward-problem-based designs for tongue-type PSA.

Chapter 3 introduced a inverse-problem-based method to design internal pressure patterns for a pneumatic soft actuator with arrayed chambers (PSA-AC). An analytical model linking pressure and surface deformation was formulated, and optimization techniques were applied to reproduce target shapes. Experiments with an eight-chamber PSA-AC validated that multiple tongue-like shapes could be realized using the designed pressure patterns.

Chapter 4 proposed a pneumatic soft actuator composed of layered membranes (PSA-LM) to enable both structural and pressure design. A geometric algorithm based on stacked triangles and Bayesian optimization and finite element analysis (FEA) were used to determine both structure and pressure patterns. Experiments demonstrated the reproduction of complex surface shapes with a RMSE of approximately 1 mm, confirming the effectiveness of a fully inverse-problem-based design approach for PSAs with variable surface shapes. The results demonstrate that structural features of the PSA with variable surface shapes that both make effective use of elastic-membrane inflation for generating surface deformation and are readily applicable to computational design methods were identified. Based on these structural insights, it became possible to apply a fully inverse-problem-based design approach that systematically determines both the actuator's structure and its internal pressure patterns.

5.2 Future Works

Several future directions are considered for the proposed methods. These are discussed from two perspectives: challenges in improving the actuator as a PSA with variable surface shapes, and challenges related to the realization of a tongue robot for *in vitro* mastication.

From the standpoint of actuator development, several challenges can be made to enhance the performance of PSAs with variable surface shape. First, further increasing the diversity of achievable surface shapes is an important task. The actuators developed in this study primarily deform through inflation. While they convex shapes effectively, they face challenges in replicating concave surfaces. In both PSA-AC and PSA-LM, unintended deformations caused by the characteristics of flexible elastic—materials such as coupled motion and resistance generated by bending moments—tend to degrade the actuator's capability to reproduce concave surface shapes. To address this issue, introducing additional components, such as rotational spring elements, could approximate these effects within the model, enabling the design of structures and internal pressure patterns that compensate for them. Another effective approach is to conduct a more comprehensive investigation of the material properties used in the actuators and impose constraints on design parameters to prevent undesired deformation. Furthermore, applying negative pressure to chambers located in concave regions to generate suction-based deformations may be effective. However, negative pressure may induce alternative deformation modes, such as buckling of membranes or inner walls. Developing a model

capable of representing these mode transitions remains a key challenge for future work.

For feedback-controlled manipulation applications, it is necessary to integrate the sensing capability presented in Chapter 2 into PSAs with variable surface shapes, such as the PSA-AC and PSA-LM proposed in Chapters 3 and 4. However, in these actuators, the presence of inner walls and layered membranes makes it difficult to embed conventional visuo–tactile sensors. One possible solution is to fabricate the inner walls from transparent materials, enabling external cameras to observe the actuator's shape. Nevertheless, transparent elastic materials[95–98] generally exhibit lower elongation and higher brittleness than standard silicone rubbers, requiring design guidelines that account for these mechanical characteristics. Such constraints may also limit the range of achievable surface shapes. Another potential approach is to embed non-contact markers, such as magnetic markers[99], inside the actuator and estimate their positions for sensing. This method preserves a mechanical structure similar to that of visuo–tactile sensors while allowing integration of sensing capabilities. Future work should focus on developing algorithms for accurately estimating marker positions and establishing optimal design guidelines for marker resolution and placement.

In both Chapter 3 and Chapter 4, the proposed PSA-AC and PSA-LM were limited to reproducing two-dimensional surface shapes. Extending these methods to three-dimensional configurations remains an important future task. Enabling the reproduction of complex three-dimensional shapes would further enhance actuator functionality. For such extension, in addition to expanding the modeling approaches used in each method, interference between air tubes and inner walls or membranes will become a new issue, requiring innovations in fabrication. One possible solution is to integrate the tubes and inner walls by forming grooves within the internal structure, thereby securing flow paths to chambers while preventing interference. Future work will involve establishing reliable fabrication techniques for producing fine internal channels and developing flow-path designs that minimize their influence on deformation behavior.

Toward the realization of an tongue robot for *in vitro* mastication, one of the key challenges is the establishment of food manipulation principles. This dissertation has primarily focused on the design methodologies of tongue-type PSAs. However, reproducing actual mastication requires defining manipulation principles that specify how the robot should move. During mastication, the tongue undergoes rapid and continuous deformations, making it necessary to consider dynamic effects in both modeling and control. Additionally, design and control methods must account for the nonuniform external contact pressures generated through interactions with food. In manipulation scenarios such as mastication, both the actuator and the target object are deformable, leading to "soft-to-soft" manipulation in which relative stiffness changes over time. It is therefore essential to clarify the relationship between active deformation, in which the actuator intentionally reshapes the target, and passive deformation, in which the actuator adapts to and holds the target. Developing systematic control strategies for each case will be an important task for future research.

Another important future direction is the utilization of *in vivo* experimental data. Measured biological data of the human tongue provide valuable insights for the design

of tongue robots. Reconstructing tongue shapes and movements from limited biological samples will enable the development of shape-generation models based on actual masticatory behavior. Applying statistical methods to time-series data can extract principal features and reveal essential patterns of biological motion. Integrating these approaches will make it possible to establish a stronger connection between tongue robots for *in vitro* mastication and real biological functions. The PSAs with variable surface shapes, whose applicability is enhanced through the above developments, can be applied to *in vitro* tongue and other flexible organ simulators. Such applications are expected to contribute to rehabilitation support and the development of nursing care foods in an aging society.

As a further direction for future development, this research is considered to have a wide range of potential applications beyond those described above. In particular, the structural features and design framework presented in Chapter 4 possess high generality, enabling possible extensions into various domains. For example, by constructing the membrane elements from transparent materials and using a transparent working fluid whose refractive index is close to that of the membrane, the structure could be applied as a variable-focus lens whose surface shape changes through hydraulic pressure. Moreover, forming the wings of aircraft or drones using a structure composed of layered membrane and appropriately distributing dynamic pressure among multiple membranes during flight may lead to variable-section wings that adapt their shape to the prevailing flight speed. In addition, the concept could be utilized for three-dimensional displays or shape-changing objects, and, when scaled up and embedded beneath the ground surface, could enable spatial interactions for rehabilitation or entertainment by dynamically altering terrain geometry.

This study has opened a new pathway for the further development of PSAs with variable surface shapes and their advanced applications. Furthermore, these achievements are anticipated to promote the establishment of new design technologies in soft robotics, providing a foundation for expanding both the functional and application range of soft robotic systems.

Appendix A

Pressure Design for PSA-AC Considering Contact Forces

A.1 Introduction

Designing internal pressure patterns that account not only for the unloaded shape but also for the contact pressure exerted by target objects and the resulting deformation is essential to manipulate objects using pneumatic soft actuators. This appendix discusses the design of internal pressure patterns for manipulation applications using PSA-ACs under contact conditions. We proposed a method to determine internal pressure patterns capable of reproducing target surface shapes while considering contact between the PSA-AC and an object. Contact pressure terms are incorporated into the surface shape model introduced in Chapter 3, enabling the construction of an analytical model that describes deformation under contact pressure distributions. Experiments were conducted using a 12-chamber PSA-AC to verify the effectiveness of the proposed method.

A.2 PSA-AC Surface Shape Model with Contact Pressure

A.2.1 Modeling of PSA-AC with Contact Pressure

Fig. A.1 shows the surface-shape model of the PSA-AC used in this study. For each node of the PSA-AC surface shape model described in Chapter 3, passive deformation is taken into account by adding terms calculated from the contact pressure distribution.

A.2.2 Chamber Inner Wall Unit

Fig. A.2(a) shows the inner wall unit of the chamber. The virtual forces $F_{wx,i}, F_{wy,i}$ acting on each linear elastic element are given by the following equations, taking into

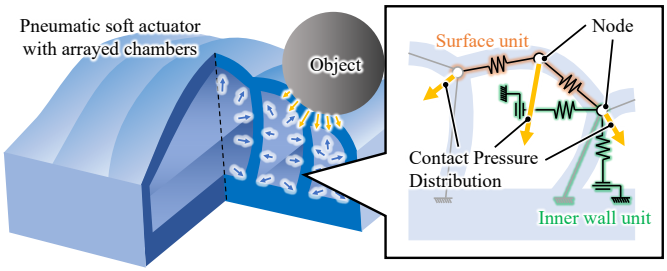
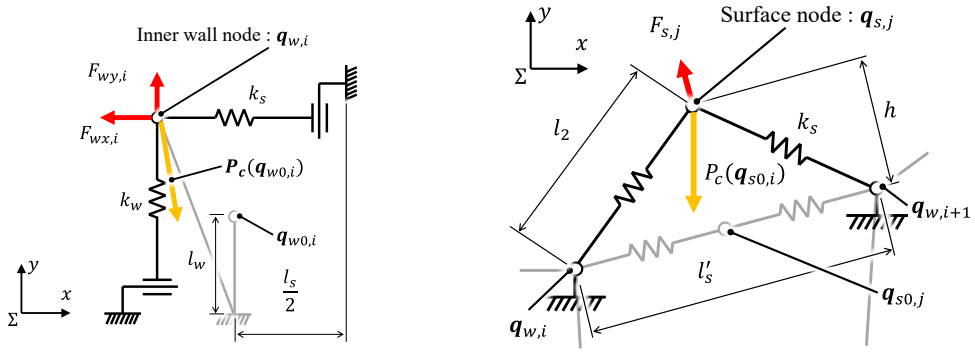


Figure A.1: Configuration of the surface shape model. The model consists of the surface unit and the inner wall unit. The pressure distribution is applied to the model assuming contact with the objects.



(a) (b)

Figure A.2: Proposal surface shape model. (a) Chamber inner wall displacement unit. (b) Chamber surface displacement unit.

account both the internal chamber pressure and the contact pressure.

$$\boldsymbol{F}_{w,i} = \begin{bmatrix} F_{wx,i} \\ F_{wy,i} \end{bmatrix} = \begin{bmatrix} l_w \Big(P_{i+1} - P_i - P_{cx}(\boldsymbol{q}_{w0,i}) \Big) \\ \dfrac{l_s}{2} \Big(P_{i+1} + P_i - P_{cy}(\boldsymbol{q}_{w0,i}) \Big) \end{bmatrix} \tag{A.1}$$

Here, $\boldsymbol{q}_{w0,i}$ denotes the position of the inner wall node before deformation, P_i, P_{i+1} represent the line pressures in the two adjacent chambers, and $\boldsymbol{P}_c = [P_{cx}, P_{cy}]^T$ is the contact pressure distribution. By calculating virtual forces from the difference between the contact pressure and the internal pressure, the model explicitly considers the contact pressure. The contact pressure distribution is a function of the position vector $\boldsymbol{q}_w$ of each node. Although the contact pressure strictly changes with deformation, for simplicity, the contact pressure $\boldsymbol{q}_{w0}$ at the initial position of the equivalent force $\boldsymbol{P}_c(\boldsymbol{q}_{w0,i})$ is used here. The position vector $\boldsymbol{q}_{w,i}$ of the ith inner wall node in the model is given by the following equation:

$$\boldsymbol{q}_{w,i} = \beta \begin{bmatrix} \dfrac{F_{wx,i}}{k_s} \\ \dfrac{F_{wy,i}}{k_w} \end{bmatrix} + \boldsymbol{q}_{w0,i} \tag{A.2}$$

A.2.3 Chamber Surface Unit

Fig. A.2(b) shows the surface unit of the chamber The contact pressure $P_{cs,j}$ at each surface node is obtained from the contact pressure distribution using the following equation.

$$P_{cs,j}(\boldsymbol{q}_{s0,j}) = P_{cx}(\boldsymbol{q}_{s0,j})\frac{q_{wx,j} - q_{s0x,j}}{l'_{s,j}} + P_{cy}(\boldsymbol{q}_{s0,j})\frac{q_{wy,j} - q_{s0y,j}}{l'_{s,j}} \tag{A.3}$$

where $\boldsymbol{q}_{s0,j}$ is the position vector of the surface node before adding $F_{s,j}$. Assuming an virtual force $F_{s,j}$ acting in the direction perpendicular to the line segment connecting $\boldsymbol{q}_{w,i}, \boldsymbol{q}_{w,i+1}$, which is derived from the chamber pressure P_j and the contact pressure P_{cs}, let $l_{2,j}$ denote the length of the elastic element when this force is applied to the j th surface node, and let h_j represent the displacement in the direction parallel to the virtual force. Then, the force balance at the coordinate $\boldsymbol{q}_{s,j}$ located at the center of the chamber surface can be expressed as follows.

$$F_{s,j} = (P_j - P_{cs,j})l_s = 2k_s\Big(l_{2,j} - \frac{l_s}{2}\Big)\frac{h_j}{l_{2,j}} \tag{A.4}$$

$$h_j = \sqrt{l_{2,j}^2 - \Big(\frac{l'_{s,j}}{2}\Big)^2} \tag{A.5}$$

Since the analytical value of h_j is difficult to obtain directly, an approximate value h'_j is used, which is calculated using the bivariate polynomial derived in Section 3.2.3. The position vector $\boldsymbol{q}_{s,j}$ of the center of the chamber surface is given as follows:

$$\boldsymbol{q}_{s,j} = \beta \begin{bmatrix} q_{sx0,j} - 2h'_j\dfrac{q_{sy0,j}}{l'_{s,j}} \\ q_{sy0,j} + 2h'_j\dfrac{q_{sx0,j}}{l'_{s,j}} \\ \end{bmatrix} \tag{A.6}$$

A.3 Solving Chamber Internal Pressure Pattern

Based on the above model, the nonlinear optimization method described in Section 3.3 is applied while taking into account the passive deformation caused by contact pressure. According to equations (3.15) and (3.16), the error vector $\boldsymbol{\Theta}$ and its sum of squares S are calculated, and the internal pressure conditions are determined using the Levenberg–Marquardt method[86–88] in accordance with equation (3.18). This enables the determination of internal pressure patterns that compensates for deformations caused by external contact forces.

A.4 Experiments

To verify the effectiveness of the proposed method, experiments were conducted using a 12 chambers PSA-AC. In the experiment, the PSA-AC was deformed into an inclined

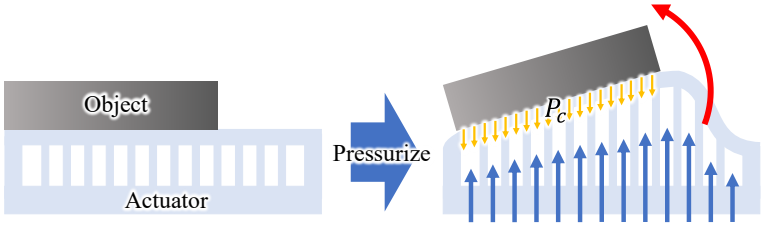


Figure A.3: Overview of the tilting task.

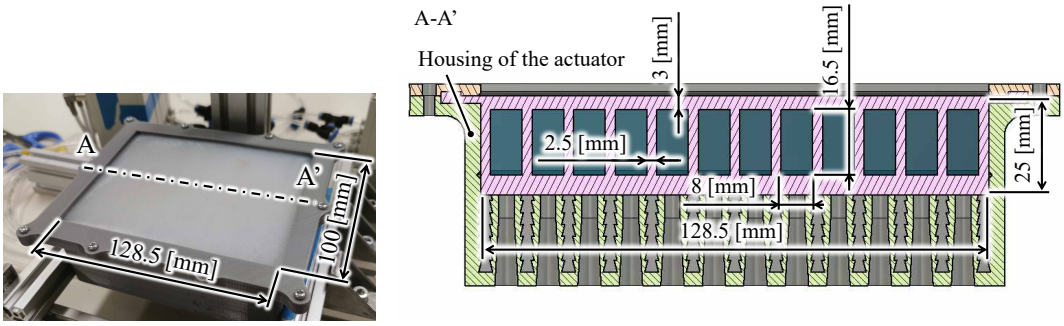


Figure A.4: Dimensions of each chamber. These are the same for all chambers except for the pressure values.

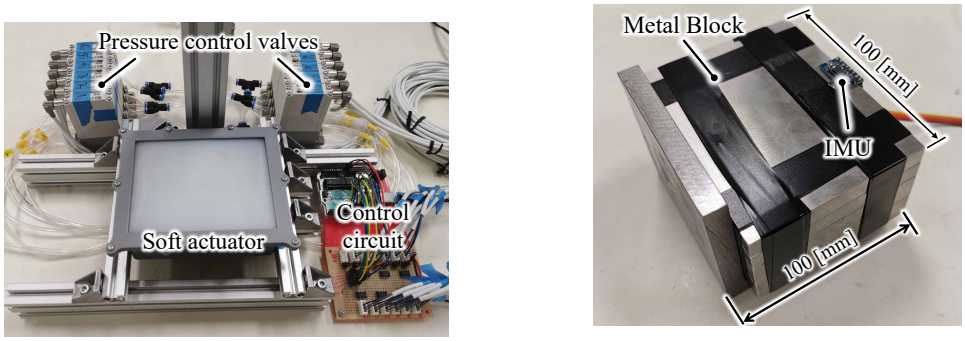
shape to tilt a pre-placed object to a specified angle, performing an object tilting task as shown in Fig. A.3.

A.4.1 Experimental Setup

Fig. A.4 shows the PSA-AC used in the experiment. The PSA-AC consisted of 12 horizontally arranged chambers. In addition, the actuator was manufactured from silicone rubber (Dragon Skin 10 NV, Smooth-on, Inc., USA) which was cured by addition polymerization using platinum as a catalyst. The modulus of elasticity for the silicone rubber was measured when the stress $E = 0.1154$ MPa. The displacement correction factor was set to $\beta = 2.5$ determined by the preliminary experiment described in Section 3.4.2. As the experimental setup, Fig. A.5(a) shows the pneumatic system used to drive the PSA-AC, and Fig. A.5(b) shows the object to be manipulated. Pressure valves were connected to each chamber of the PSA-AC to control the pressure values individually. The object is a metal block with a total weight of 5 kg. A 6-axis inertial measurement unit(IMU) is attached to the block for angle measurement.

A.4.2 Object Tilting Task

Fig. A.6 shows the target shape and corresponding contact pressure distribution. The target shape is designed so that the inclined section on the left side tilts the 5 kg object



(a) (b)

Figure A.5: Experimental setup. (a) Pneumatic system for the actuator drive. (b) Object to be manipulated.

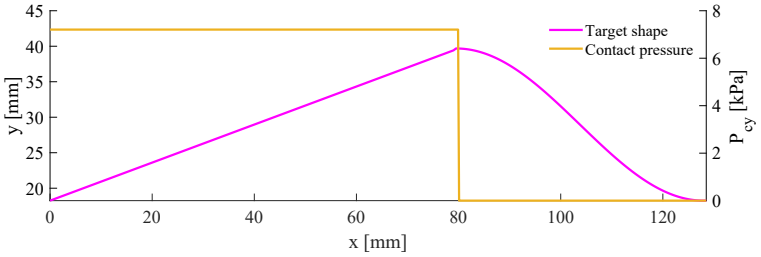


Figure A.6: The target shape and applied pressure distribution for the tilting task.

by 15 deg. For this target shape, the internal pressure patterns are determined under two conditions: with and without considering the contact pressure. In the condition considering contact pressure, it is assumed that no slip occurs between the object and the PSA-AC, and that they are in full contact along the inclined section. A uniform contact pressure distribution of $\boldsymbol{P_c} = [0, 7.2]^T$ kPa is applied within the inclined region of $0 \leq x \leq 80$ mm. In the unloaded condition without considering contact pressure, the internal pressure pattern is calculated by setting $\boldsymbol{P_c} = 0$ kPa. The two types of internal pressure patterns are applied to the actual 12 chambers PSA-AC, and the resulting inclination angles of the object are measured and compared for evaluation.

A.4.3 Actual Internal Pressure Patterns

Figure A.7 shows the internal pressure patterns and corresponding model shapes obtained using the proposed method. The pressures obtained under the contact-pressure condition in Fig. A.7(b) are higher than the internal pressure pattern in Fig. A.7(a) obtained under the unloaded condition, . However, deformation is suppressed by the contact pressure, and as a result, the model shape is confirmed to match the target shape. The RMSE remains below 0.8 mm in both cases. This indicating that internal pressure patterns capable of matching the model shape to the target shape are obtained regardless of whether contact pressure is considered.

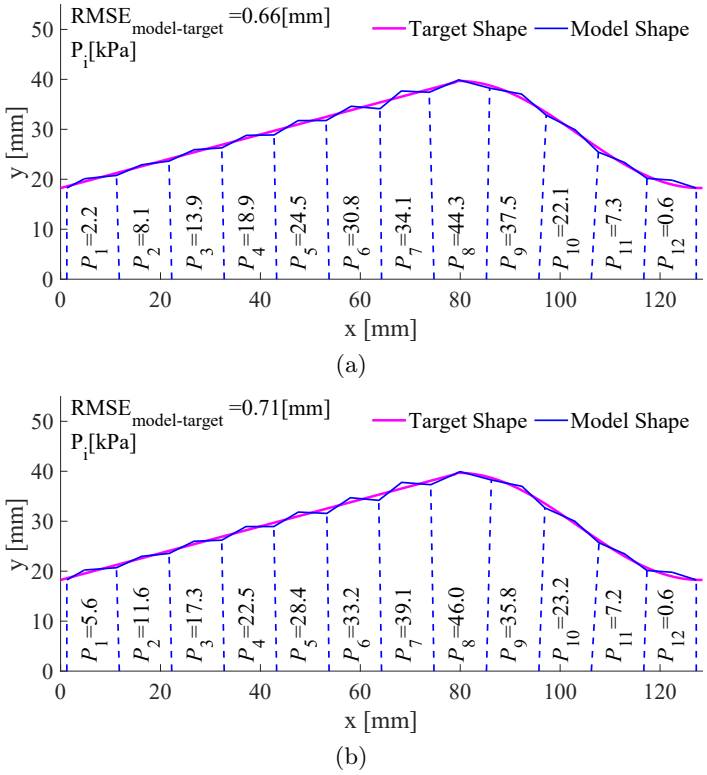


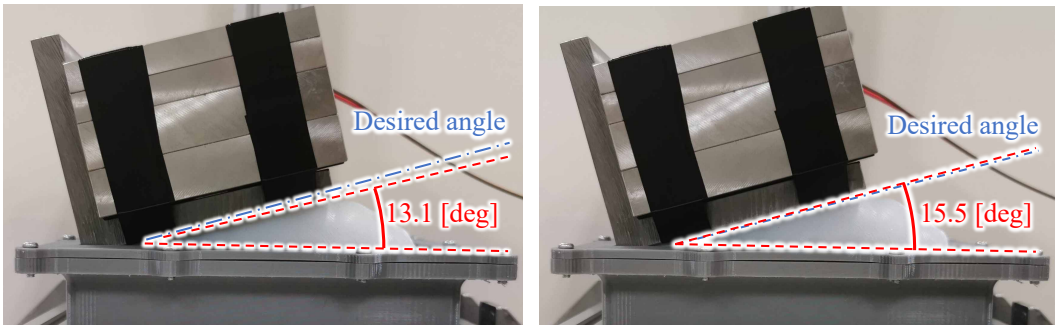
Figure A.7: Pressure conditions and model shapes. (a) Without contact pressure consideration. (b) With contact pressure consideration.

A.4.4 Experimental Results

Fig. A.8 shows the experimental results. The angles indicated in the figure represent the average values of IMU measurements obtained over five repetitions of the tilting task for each internal pressure pattern. In Fig. A.8(a), when the internal pressure pattern obtained under the unloaded condition is applied. The inclination angle reaches 13.1 deg, which does not achieve the target angle of 15 deg. Fig. A.8(b) shows the result when the internal pressure pattern obtained under the contact pressure condition is applied. In contrast, the inclination angle reaches 15.5 deg, indicating that the target angle is more closely achieved. The experimental results demonstrate that more accurate object manipulation can be achieved by introducing a contact pressure term into the surface shape model for explicitly considering object interference during internal pressure pattern design.

A.5 Conclusion

In this appendix, a method for designing internal pressure patterns considering interactions with target objects aiming toward object manipulation using the PSA-AC was



(a) (b)

Figure A.8: Experimental results. (a) Without contact pressure consideration. (b) With contact pressure consideration.

proposed. The main results obtained are summarized as follows.

- An analytical model of PSA-AC surface deformation was introduced to account for both contact pressure distribution and internal pressure patterns. This model enables the design of internal pressure patterns capable of generating the desired surface shape under the contact pressure exerted by the target object.
- The effectiveness of the proposed method was verified through an experiment assuming an object tilting task using a 12 chambers PSA-AC. Internal pressure patterns were designed under both conditions with and without considering contact pressure to reproduce the target shape. By applying these two pressure patterns to the actual actuator, it was confirmed that under the contact pressure condition, the reproducibility of the target angle improved compared with the unloaded condition.

Appendix B

Estimate Ogden model paremeters

The material parameters of the Ogden model[91], which is widely used as a superelastic material model, must be estimated for internal pressure design. The parameters are estimated by fitting the model to the experimental data obtained from the tensile test, following the general procedure for identifying material constants[100]. In this study, the third-order Ogden strain energy function W shown below is used.

$$W = \sum_{n=1}^{3} \mu_n \left(\frac{\lambda_1^{\gamma_n} + \lambda_2^{\gamma_n} + \lambda_3^{\gamma_n} - 3}{\gamma_n} \right) \tag{B.1}$$

The material used for PSA-LM was silicone rubber (Dragon Skin 10 NV, Smooth-On, Inc., USA). The material constants were determined using the following procedure. First, test specimens of the target material were prepared and subjected to uniaxial tensile and pure shear tests. This yielded stress-strain ratio data, according to:

$$\{\lambda_j, \sigma_j^{\exp}\}_{j=1}^{N_u} \tag{B.2}$$

$$\{\lambda_k, \tau_k^{\exp}\}_{k=1}^{N_s} \tag{B.3}$$

The uniaxial tensile test was conducted using a No. 1 dumbbell-shaped test piece, as specified in JIS K6251, in accordance with the methods in previous research[89,90]. The pure shear test was conducted using rectangular test pieces measuring 150 mm × 12 mm × 2 mm, as described in the same literature, with a tensile load applied to the short side. The residual r_j, r_k between the model and experimental values during optimization was defined by the following equation.

$$r_j^{\mathrm{uni}} = \sigma_{\mathrm{uni}}(\lambda_j; \{\mu_i, \gamma_i\}) - \sigma_j^{\exp} \tag{B.4}$$

$$r_k^{\mathrm{shear}} = \tau(\lambda_k; \{\mu_i, \gamma_i\}) - \tau_k^{\exp} \tag{B.5}$$

The objective function was defined as follows:

$$S(\{\mu_i, \gamma_i\}) = \sum_{j=1}^{N_{\mathrm{u}}} (r_j^{\mathrm{uni}})^2 + \sum_{k=1}^{N_{\mathrm{s}}} (r_k^{\mathrm{shear}})^2 \tag{B.6}$$

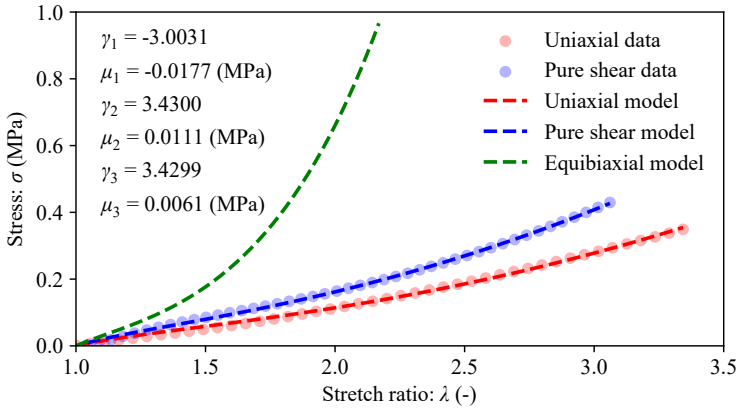


Figure B.1: Ogden model plot for DragonSkin 10 NV.

The parameters $\{\mu_i, \gamma_i\}$ of the Ogden model are determined by performing optimization using the Levenberg–Marquardt method[86–88] to minimize the objective function S.

The tensile test results and parameter estimation results are shown in Fig. B.1. In both the uniaxial tensile and pure shear tests, the model response and experimental values matched well, confirming the validity of the fitting. The equibiaxial tensile model is indicated with the green dotted line, exhibiting a rapid increase in stress compared to single-axis tension and pure shear, which confirms its ability to accurately reproduce the nonlinearity of typical superelastic materials.

References

1) C. Lee, M. Kim, Y. J. Kim, N. Hong, S. Ryu, H. J. Kim, and S. Kim, "Soft robot review," *International Journal of Control, Automation and Systems*, vol. 15, no. 1, pp. 3–15, 2017.

2) D. Rus and M. T. Tolley, "Design, fabrication and control of soft robots," *Nature*, vol. 521, no. 7553, pp. 467–475, 2015.

3) S. Kim, C. Laschi, and B. Trimmer, "Soft robotics: a bioinspired evolution in robotics," *Trends in biotechnology*, vol. 31, no. 5, pp. 287–294, 2013.

4) J. Pinskier and D. Howard, "From bioinspiration to computer generation: Developments in autonomous soft robot design," *Advanced Intelligent Systems*, vol. 4, no. 1, p. 2100086, 2022.

5) M. S. Xavier, C. D. Tawk, A. Zolfagharian, J. Pinskier, D. Howard, T. Young, J. Lai, S. M. Harrison, Y. K. Yong, M. Bodaghi, and A. J. Fleming, "Soft pneumatic actuators: A review of design, fabrication, modeling, sensing, control and applications," *IEEE Access*, vol. 10, pp. 59 442–59 485, 2022.

6) J. Walker, T. Zidek, C. Harbel, S. Yoon, F. S. Strickland, S. Kumar, and M. Shin, "Soft robotics: A review of recent developments of pneumatic soft actuators," *Actuators*, vol. 9, no. 1, 2020.

7) H. Su, X. Hou, X. Zhang, W. Qi, S. Cai, X. Xiong, and J. Guo, "Pneumatic soft robots: Challenges and benefits," *Actuators*, vol. 11, no. 3, 2022.

8) D. Loda and M. Tiboni, "Pneunets soft actuators: characterization and deformation conditioning," in *The International Conference of IFToMM ITALY*. Springer, 2024, pp. 466–473.

9) Y. Wu, M. Lu, L. Ding, N. Lu, C. Yu, and X. Ye, "Modeling analysis of soft pneu-net actuators from low to high pressure in free space," *Proceedings of the Institution of Mechanical Engineers, Part C: Journal of Mechanical Engineering Science*, vol. 239, no. 13, pp. 5034–5049, 2025.

10) G. Klute, J. Czerniecki, and B. Hannaford, "Mckibben artificial muscles: pneumatic actuators with biomechanical intelligence," in *1999 IEEE/ASME International Conference on Advanced Intelligent Mechatronics (Cat. No.99TH8399)*, 1999, pp. 221–226.

11) G. Andrikopoulos, G. Nikolakopoulos, and S. Manesis, "A survey on applications of pneumatic artificial muscles," in *2011 19th Mediterranean Conference on Control & Automation (MED)*, 2011, pp. 1439–1446.

12) F. Daerden, D. Lefeber, B. Verrelst, and R. Van Ham, "Pleated pneumatic artificial muscles: actuators for automation and robotics," in *2001 IEEE/ASME International Conference on Advanced Intelligent Mechatronics. Proceedings (Cat. No.01TH8556)*, vol. 2, 2001, pp. 738–743 vol.2.

13) S. Kurumaya, H. Nabae, G. Endo, and K. Suzumori, "Design of thin mckibben muscle and multifilament structure," *Sensors and Actuators A: Physical*, vol. 261, pp. 66–74, 2017.

14) S. Abd-El-Malek, "The part played by the tongue in mastication and deglutition," *Journal of anatomy*, vol. 89, no. Pt 2, p. 250, 1955.

15) J. B. Palmer, K. M. Hiiemae, and J. Liu, "Tongue-jaw linkages in human feeding: A preliminary videofluorographic study," *Archives of Oral Biology*, vol. 42, no. 6, pp. 429–441, 1997.

16) T. Fukuoka, K. Hori, and T. Ono, "Quantitative evaluation of swallowing function in parkinson ' s disease using tongue pressure measurement: a mini-review," *Frontiers in Neurology*, vol. 15, p. 1355627, 2024.

17) K. Hori, H. Taniguchi, H. Hayashi, J. Magara, Y. Minagi, Q. Li, T. Ono, and M. Inoue, "Role of tongue pressure production in oropharyngeal swallow biomechanics," *Physiological reports*, vol. 1, no. 6, p. e00167, 2013.

18) K. Hori, T. Ono, H. Iwata, T. Nokubi, and I. Kumakura, "Tongue pressure against hard palate during swallowing in post-stroke patients," *Gerodontology*, vol. 22, no. 4, pp. 227–233, 2005.

19) T. Ono, K. Hori, and T. Nokubi, "Pattern of tongue pressure on hard palate during swallowing," *Dysphagia*, vol. 19, no. 4, pp. 259–264, 2004.

20) K. Murakami, Y. Tokuda, K. Hori, Y. Minagi, F. Uehara, J. Okawa, S. Ishihara, M. Nakauma, T. Funami, Y. Maeda, K. Ikebe, and T. Ono, "Effect of fracture properties of gels on tongue pressure during different phases of squeezing and swallowing." *Journal of texture studies*, vol. 52, no. 3, pp. 303–313, 2 2021.

21) K. Hori, H. Hayashi, S. Yokoyama, T. Ono, S. Ishihara, J. Magara, H. Taniguchi, T. Funami, Y. Maeda, and M. Inoue, "Comparison of mechanical analyses and

tongue pressure analyses during squeezing and swallowing of gels," *Food Hydrocolloids*, vol. 44, pp. 145–155, 2015.

22) G. Álvarez, F. J. Dias, M. F. Lezcano, A. Arias, and R. Fuentes, "A novel three-dimensional analysis of tongue movement during water and saliva deglutition: a preliminary study on swallowing patterns," *Dysphagia*, vol. 34, no. 3, pp. 397–406, 2019.

23) S. Kodama, S. Fujiwara, J. Okawa, S. Shitara, K. Hori, and T. Ono, "Modulation of tongue motion and tongue pressure during liquid swallowing with different bolus volumes," *Journal of Oral Rehabilitation*, vol. 48, no. 11, pp. 1243–1251, 2021.

24) S. Shitara, S. Fujiwara, J. Okawa, S. Kodama, K. Hori, and T. Ono, "Coordination between lingual motion and pressure production during dipper/tipper type swallows," *Journal of Oral Rehabilitation*, vol. 47, no. 12, pp. 1479–1488, 2020.

25) A. Imai, M. Tanaka, M. Tatsuta, and T. Kawazoe, "Ultrasonographic images of tongue movement during mastication," *Journal of Osaka Dental University*, vol. 29, no. 2, pp. 61–69, 1995.

26) R. Hashem, S. Kazemi, M. Stommel, L. K. Cheng, and W. Xu, "SoRSS: A soft robot for bio-mimicking stomach anatomy and motility," *Soft Robotics*, vol. 10, no. 3, pp. 504–516, 2023, pMID: 36346277.

27) Y. Dang, Y. Liu, R. Hashem, D. Bhattacharya, J. Allen, M. Stommel, L. K. Cheng, and W. Xu, "SoGut: A soft robotic gastric simulator," *Soft Robotics*, vol. 8, no. 3, pp. 273–283, 2021, pMID: 32559391.

28) T. Nakamura, "Peristaltic mixing pump based on bowel peristalsis using pneumatic artificial rubber muscles and prospects for practical applications," *Journal of Robotics and Mechatronics*, vol. 34, no. 2, pp. 276–278, 2022.

29) S. Dirven, J. Allen, W. P. Xu, and L. K. Cheng, "Soft-robotic esophageal swallowing as a clinically-inspired bolus rheometry technique," *Measurement Science and Technology*, vol. 28, no. 3, p. 035701, 2017.

30) S. Zhang, Q. Wang, Z. Li, Y. Xu, and B. Su, "An esophagus-inspired magnetic-driven soft robot for directional transport of objects," *Journal of Materials Chemistry C*, vol. 13, no. 1, pp. 250–259, 2025.

31) D. Bhattacharya, S. J. Ali, L. K. Cheng, and W. Xu, "RoSE: A robotic soft esophagus for endoprosthetic stent testing," *Soft Robotics*, vol. 8, no. 4, pp. 397–415, 2021, pMID: 32758017.

32) T. Kawamura, T. Tandai, and H. Takanobu, "Mechanism and control of tongue robot," in *2005 IEEE/RSJ International Conference on Intelligent Robots and Systems*, 2005, pp. 1041–1046.

33) K. Fukui, Y. Ishikawa, K. Ohno, N. Sakakibara, M. Honda, and A. Takanishi, "Three dimensional tongue with liquid sealing mechanism for improving resonance on an anthropomorphic talking robot," in *2009 IEEE/RSJ International Conference on Intelligent Robots and Systems*, 2009, pp. 5456–5462.

34) K. Fukui, E. Shintaku, A. Shimomura, N. Sakakibara, Y. Ishikawa, M. Honda, and A. Takanishi, "Control methods based on neural network forward and inverse models for a biomechanical structured vocal cord model on an anthropomorphic talking robot," in *2008 IEEE International Conference on Robotics and Automation*, 2008, pp. 3648–3653.

35) K. Fukui, Y. Ishikawa, T. Sawa, E. Shintaku, M. Honda, and A. Takanishi, "New anthropomorphic talking robot having a three-dimensional articulation mechanism and improved pitch range," in *Proceedings 2007 IEEE International Conference on Robotics and Automation*, 2007, pp. 2922–2927.

36) M. Bando and K. Osuka, "Mechanism design of elements for artificial tongue taking triangle element division imitated arrangement of lingual muscle," in *2004 IEEE International Conference on Robotics and Biomimetics*, 2004, pp. 867–872.

37) R. Shijo, M. Nagano, I. Mizoguchi, T. Ando, K. Tamura, K. Hiki, S. Sakurai, K. Hirota, and T. Nojima, "Licker: A tongue robot for representing realistic tongue motions," in *SIGGRAPH Asia 2019 Emerging Technologies*, ser. SA '19. New York, NY, USA: Association for Computing Machinery, 2019, p. 27–28.

38) N. Endo, Y. Kizaki, and N. Kamamichi, "Flexible pneumatic bending actuator for a robotic tongue," *Journal of Robotics and Mechatronics*, vol. 32, no. 5, pp. 894–902, 2020.

39) X. Lu, W. Xu, and X. Li, "Concepts and simulations of a soft robot mimicking human tongue," in *2015 6th International Conference on Automation, Robotics and Applications (ICARA)*, 2015, pp. 332–336.

40) ——, "A soft robotic tongue—mechatronic design and surface reconstruction," *IEEE/ASME Transactions on Mechatronics*, vol. 22, no. 5, pp. 2102–2110, 2017.

41) ——, "Modeling of a soft robotic tongue driven by compressed air," *IEEE Access*, vol. 11, pp. 61 901–61 913, 2023.

42) S. Rodriguez, R. Galvan, and D. Ganta, "Modelling and simulation of soft robotic human tongue with improved motion," *Engineering Research Express*, vol. 3, no. 4, p. 045027, 2021.

43) E. Krisdityawan, S. Yokota, A. Matsumoto, D. Chugo, S. Muramatsu, and H. Hashimoto, "Soft robotic tongue that mimicking english pronunciation movements," in *2023 IEEE International Conference on Mechatronics (ICM)*, 2023, pp. 1–5.

44) X. Gao, K. Okasaki, H. Ohashi, T. Sakurai, and Y. Morimoto, "Tongue-like bioactuator with multiple skeletal muscle tissues," in *2025 IEEE 38th International Conference on Micro Electro Mechanical Systems (MEMS)*, 2025, pp. 535–537.

45) K. Sawada, K. Osuka, and T. Ono, "On soft machine-toward the realization of mechanical speech synthesizer," in *IEEE SMC'99 Conference Proceedings. 1999 IEEE International Conference on Systems, Man, and Cybernetics (Cat. No.99CH37028)*, vol. 4, 1999, pp. 978–983 vol.4.

46) Y. Ishikawa, H. Nabae, G. Endo, and K. Suzumori, "Prototype of tongue muscle mimicking soft robot," *The 7th Jc-IFToMM International Symposium*, vol. 7, pp. 232–235, 2024.

47) A. Avila-Sierra, Y. Bugarin-Castillo, M. Glumac, J. Bussiere, A. Saint-Eve, V. Mathieu, Y. Kobayashi, and M. Ramaioli, "A first-of-its-kind 3d biomimetic artificial mouth capable of reproducing the oral processing of soft foods," *Scientific Reports*, vol. 14, no. 1, p. 22908, 2024.

48) M. Marconati, S. Pani, J. Engmann, A. Burbidge, and M. Ramaioli, "A soft robotic tongue to develop solutions to manage swallowing disorders," 2020. [Online]. Available: https://arxiv.org/abs/2003.01194

49) A. Lavoisier, A. Avila-Sierra, C. Timpe, P. Kuehl, L. Wagner, C. Tournier, and M. Ramaioli, "A novel soft robotic pediatric in vitro swallowing device to gain insights into the swallowability of mini-tablets," *International Journal of Pharmaceutics*, vol. 629, p. 122369, 2022.

50) B. Dai, M. Devezeaux de Lavergne, C. Moccand, F. Dionisi, and J. Hughes, "Babybot: Robot with infant-like feeding behaviours and developmental oral skills," *npj Robotics*, vol. 3, no. 1, p. 10, 2025.

51) P. Moseley, J. M. Florez, H. A. Sonar, G. Agarwal, W. Curtin, and J. Paik, "Modeling, design, and development of soft pneumatic actuators with finite element method," *Advanced engineering materials*, vol. 18, no. 6, pp. 978–988, 2016.

52) H. Chen, M. A. Ali, Z. Wang, J. Chen, M. N. Ramadan, and M. Alkhedher, "Performance optimizing of pneumatic soft robotic hands using wave-shaped contour actuator," *Results in Engineering*, vol. 25, p. 103456, 2025.

53) G. Runge, J. Peters, and A. Raatz, "Design optimization of soft pneumatic actuators using genetic algorithms," in *2017 IEEE International Conference on Robotics and Biomimetics (ROBIO)*. IEEE, 2017, pp. 393–400.

54) K. G. Demir, Z. Zhang, J. Yang, and G. X. Gu, "Computational and experimental design exploration of 3d-printed soft pneumatic actuators," *Advanced Intelligent Systems*, vol. 2, no. 7, p. 2000013, 2020.

55) D. Wang, C. Jiang, and G. Gu, "Modeling and design of lattice-reinforced pneumatic soft robots," *IEEE Transactions on Robotics*, vol. 40, pp. 606–623, 2024.

56) Y. Pu, S. Zheng, X. Hu, S. Tang, and N. An, "Robotic skins inspired by auxetic metamaterials for programmable bending of soft actuators," *Materials & Design*, vol. 246, p. 113334, 2024.

57) L. Mosser, L. Barbé, L. Rubbert, and P. Renaud, "Towards automatic design of soft pneumatic actuators: Inner structure design using cnn model and bézier curve-based genetic algorithm," *IEEE Robotics and Automation Letters*, vol. 8, no. 10, pp. 6603–6610, 2023.

58) H. Zhang, A. S. Kumar, F. Chen, J. Y. H. Fuh, and M. Y. Wang, "Topology optimized multimaterial soft fingers for applications on grippers, rehabilitation, and artificial hands," *IEEE/ASME Transactions on Mechatronics*, vol. 24, no. 1, pp. 120–131, 2019.

59) S. Chen, F. Chen, Z. Cao, Y. Wang, Y. Miao, G. Gu, and X. Zhu, "Topology optimization of skeleton-reinforced soft pneumatic actuators for desired motions," *IEEE/ASME Transactions on Mechatronics*, vol. 26, no. 4, pp. 1745–1753, 2021.

60) Y. Chen, Z. Xia, and Q. Zhao, "Optimal design of soft pneumatic bending actuators subjected to design-dependent pressure loads," *IEEE/ASME Transactions on Mechatronics*, vol. 24, no. 6, pp. 2873–2884, 2019.

61) L. Ding, N. Dai, X. Mu, S. Xie, X. Fan, D. Li, and X. Cheng, "Design of soft multi-material pneumatic actuators based on principal strain field," *Materials & Design*, vol. 182, p. 108000, 2019.

62) L.-K. Ma, Y. Zhang, Y. Liu, K. Zhou, and X. Tong, "Computational design and fabrication of soft pneumatic objects with desired deformations," *ACM Trans. Graph.*, vol. 36, no. 6, Nov. 2017.

63) J. H. Pikul, S. Li, H. Bai, R. T. Hanlon, I. Cohen, and R. F. Shepherd, "Stretchable surfaces with programmable 3d texture morphing for synthetic camouflaging skins," *Science*, vol. 358, no. 6360, pp. 210–214, 2017.

64) S.-Y. Jang, M. Cho, H. Kim, M. Choi, S. Mun, J.-H. Youn, J. Park, G. Hwang, I. Hwang, S. Yun, and K.-U. Kyung, "Dynamically reconfigurable shape-morphing and tactile display via hydraulically coupled mergeable and splittable pvc gel actuator," *Science Advances*, vol. 10, no. 39, p. eadq2024, 2024.

65) J. Wang, M. Sotzing, M. Lee, and A. Chortos, "Passively addressed robotic morphing surface (parms) based on machine learning," *Science Advances*, vol. 9, no. 29, p. eadg8019, 2023.

66) Y. Bai, H. Wang, Y. Xue, Y. Pan, J.-T. Kim, X. Ni, T.-L. Liu, Y. Yang, M. Han, Y. Huang *et al.*, "A dynamically reprogrammable surface with self-evolving shape morphing," *Nature*, vol. 609, no. 7928, pp. 701–708, 2022.

67) X. Ni, H. Luan, J.-T. Kim, S. I. Rogge, Y. Bai, J. W. Kwak, S. Liu, D. S. Yang, S. Li, S. Li *et al.*, "Soft shape-programmable surfaces by fast electromagnetic actuation of liquid metal networks," *Nature communications*, vol. 13, no. 1, p. 5576, 2022.

68) M. A. Robertson, M. Murakami, W. Felt, and J. Paik, "A compact modular soft surface with reconfigurable shape and stiffness," *IEEE/ASME Transactions on Mechatronics*, vol. 24, no. 1, pp. 16–24, 2019.

69) H. Iwata, H. Yano, F. Nakaizumi, and R. Kawamura, "Project feelex: adding haptic surface to graphics," in *Proceedings of the 28th Annual Conference on Computer Graphics and Interactive Techniques*, ser. SIGGRAPH '01. New York, NY, USA: Association for Computing Machinery, 2001, p. 469–476.

70) S. Mollaee, A. HajiRassouliha, D. M. Budgett, A. J. Taberner, and P. M. Nielsen, "Model-based design of a pneumatic actuator for a dynamically reconfigurable socket for transtibial amputees," *Frontiers in Bioengineering and Biotechnology*, vol. 12, p. 1459056, 2024.

71) B. Mosadegh, A. D. Mazzeo, R. F. Shepherd, S. A. Morin, U. Gupta, I. Z. Sani, D. Lai, S. Takayama, and G. M. Whitesides, "Control of soft machines using actuators operated by a braille display," *Lab on a Chip*, vol. 14, no. 1, pp. 189–199, 2014.

72) R. Sakuma, Y. Sakai, Y. Kawahara, and T. Hiraki, "Demonstration of multi-layered inflatables: Asymmetric-shaped inflatable structures by stacked planar sheets," in *ACM SIGGRAPH 2025 Emerging Technologies*, ser. SIGGRAPH '25. New York, NY, USA: Association for Computing Machinery, 2025.

73) S. Bonfanti, R. Guerra, F. Font-Clos, D. Rayneau-Kirkhope, and S. Zapperi, "Automatic design of mechanical metamaterial actuators," *Nature communications*, vol. 11, no. 1, p. 4162, 2020.

74) G. Bordiga, E. Medina, S. Jafarzadeh, C. Bösch, R. P. Adams, V. Tournat, and K. Bertoldi, "Automated discovery of reprogrammable nonlinear dynamic metamaterials," *Nature Materials*, vol. 23, no. 11, pp. 1486–1494, 2024.

75) K. Hori, T. Ono, K. ichi Tamine, J. Kondo, S. Hamanaka, Y. Maeda, J. Dong, and M. Hatsuda, "Newly developed sensor sheet for measuring tongue pressure during swallowing," *Journal of Prosthodontic Research*, vol. 53, no. 1, pp. 28–32, 2009.

76) K. C. Galloway, Y. Chen, E. Templeton, B. Rife, I. S. Godage, and E. J. Barth, "Fiber optic shape sensing for soft robotics," *Soft Robotics*, vol. 6, no. 5, pp. 671–684, 2019, pMID: 31241408.

77) H. Choi, M. R. Cutkosky, and A. A. Stanley, "Integrated pneumatic sensing and actuation for soft haptic devices," *IEEE Robotics and Automation Letters*, vol. 8, no. 11, pp. 7591–7598, 2023.

78) J. Barreiros, I. Karakurt, P. Agarwal, T. Agcayazi, S. Reese, K. Healy, and Y. Menguc, "Self-sensing elastomeric membrane for haptic bubble arrray," in *2020 3rd IEEE International Conference on Soft Robotics (RoboSoft)*, 2020, pp. 229–236.

79) A. Yamaguchi and C. G. Atkeson, "Combining finger vision and optical tactile sensing: Reducing and handling errors while cutting vegetables," in *2016 IEEE-RAS 16th International Conference on Humanoid Robots (Humanoids)*, 2016, pp. 1045–1051.

80) W. Yuan, S. Dong, and E. H. Adelson, "Gelsight: High-resolution robot tactile sensors for estimating geometry and force," *Sensors*, vol. 17, no. 12, 2017.

81) N. Kuppuswamy, A. Castro, C. Phillips-Grafflin, A. Alspach, and R. Tedrake, "Fast model-based contact patch and pose estimation for highly deformable dense-geometry tactile sensors," *IEEE Robotics and Automation Letters*, vol. 5, no. 2, pp. 1811–1818, 2020.

82) R. Ambrus, V. Guizilini, N. Kuppuswamy, A. Beaulieu, A. Gaidon, and A. Alspach, "Monocular depth estimation for soft visuotactile sensors," in *2021 IEEE 4th International Conference on Soft Robotics (RoboSoft)*, 2021, pp. 643–649.

83) D. A. Forsyth and J. Ponce, *Computer Vision: A Modern Approach.* Prentice Hall Professional Technical Reference, 2002.

84) G. Bradski, "The OpenCV Library," *Dr. Dobb's Journal of Software Tools*, 2000.

85) P. Virtanen, R. Gommers, T. E. Oliphant, M. Haberland, T. Reddy, D. Cournapeau, E. Burovski, P. Peterson, W. Weckesser, J. Bright, S. J. van der Walt, M. Brett, J. Wilson, K. J. Millman, N. Mayorov, A. R. J. Nelson, E. Jones, R. Kern, E. Larson, C. J. Carey, İ. Polat, Y. Feng, E. W. Moore, J. VanderPlas, D. Laxalde, J. Perktold, R. Cimrman, I. Henriksen, E. A. Quintero, C. R. Harris, A. M. Archibald, A. H. Ribeiro, F. Pedregosa, P. van Mulbregt, and SciPy 1.0 Contributors, "SciPy 1.0: Fundamental Algorithms for Scientific Computing in Python," *Nature Methods*, vol. 17, pp. 261–272, 2020.

86) K. Levenberg, "A method for the solution of certain non – linear problems in least squares," *Quarterly of Applied Mathematics*, vol. 2, pp. 164–168, 1944.

87) D. W. Marquardt, "An algorithm for least-squares estimation of nonlinear parameters," *Journal of the Society for Industrial and Applied Mathematics*, vol. 11, no. 2, pp. 431–441, 1963.

88) A. Fischer, A. F. Izmailov, and M. V. Solodov, "The levenberg–marquardt method: an overview of modern convergence theories and more," *Computational Optimization and Applications*, vol. 89, no. 1, pp. 33–67, 2024.

89) L. R. G. Treloar, "Stress-strain data for vulcanized rubber under various types of deformation," *Rubber Chemistry and Technology*, vol. 17, no. 4, pp. 813–825, 12 1944.

90) L. Meunier, G. Chagnon, D. Favier, L. Orgéas, and P. Vacher, "Mechanical experimental characterisation and numerical modelling of an unfilled silicone rubber," *Polymer Testing*, vol. 27, no. 6, pp. 765–777, 2008.

91) R. W. Ogden, "Large deformation isotropic elasticity–on the correlation of theory and experiment for incompressible rubberlike solids," *Proceedings of the Royal Society of London. A. Mathematical and Physical Sciences*, vol. 326, no. 1567, pp. 565–584, 1972.

92) P. I. Frazier, *Bayesian Optimization.* INFORMS TutORials in Operations Research, 2018, ch. 11, pp. 255–278. [Online]. Available: https://pubsonline.informs.org/doi/abs/10.1287/educ.2018.0188

93) T. Head, M. Kumar, H. Nahrstaedt, G. Louppe, and I. Shcherbatyi, "scikit-optimize/scikit-optimize," Oct. 2021. [Online]. Available: https://doi.org/10.5281/zenodo.5565057

94) P. Bourdiol, A. Mishellany-Dutour, M.-A. Peyron, and A. Woda, "Contributory role of the tongue and mandible in modulating the in-mouth air cavity at rest," *Clinical oral investigations*, vol. 17, 12 2012.

95) C. Lothongkam, P. Rohwetter, W. Habel, and E. Gockenbach, "Dielectric strength behavior and mechanical properties of transparent silicone rubbers for hv cable accessories," in *Proceedings of 2014 International Symposium on Electrical Insulating Materials*, 2014, pp. 503–506.

96) X. Li, Y. Xue, D. Zhang, and Y. Chen, "Robust silicone rubber with high transparency by loading with porous hollow glass microsphere," *Journal of Polymer Research*, vol. 30, no. 11, p. 426, 2023.

97) Y. Wu, J. Liu, X. Jiao, F. Cheng, G. Lai, and X. Yang, "Uv-cured transparent flexible silicone materials with high tensile strength," *ACS omega*, vol. 5, no. 11, pp. 6199–6206, 2020.

98) H. Bao, Y. Wu, J. Liu, X. Hua, G. Lai, and X. Yang, "Polyester–polysiloxane hyperbranched block polymers for transparent flexible materials," *ACS omega*, vol. 5, no. 45, pp. 29 513–29 519, 2020.

99) T. Kawasetsu, T. Horii, H. Ishihara, and M. Asada, "Flexible tri-axis tactile sensor using spiral inductor and magnetorheological elastomer," *IEEE Sensors Journal*, vol. 18, no. 14, pp. 5834–5841, 2018.

100) L. Marechal, P. Balland, L. Lindenroth, F. Petrou, C. Kontovounisios, and F. Bello, "Toward a common framework and database of materials for soft robotics," *Soft Robotics*, vol. 8, no. 3, pp. 284–297, 2021.

Achievements

Journal Papers

1. K. Mizuno and M. Higashimori, "Internal pressure pattern design for variable surface shapes of tongue-type pneumatic soft actuator," *IEEE Robotics and Automation Letters (RA-L)*, vol. 9, no. 4, pp. 3491–3497, April 2024.
2. K. Mizuno and M. Higashimori, "Pressurization Patterns Determination Method of Pneumatic Soft Actuator with Arrayed Chambers under Interaction with Object," *Journal of the Robotics Society of Japan*, vol. 42, no. 8, pp. 805–808, October 2024.
3. K. Mizuno and M. Higashimori, "Novel pneumatic soft actuator with layered membranes and its structure and pressure design method," *IEEE Access*, vol. 13, pp. 180662–180677, October 2025.

Proceedings of International Conferences

Full-Paper Review

1. K. Mizuno, K. Yamada, H. Nakada, M. Thu Ya, K. Hori, and M. Higashimori, "Pneumatic soft actuator capable of visuo-tactile sensing toward an *in vitro* tongue simulator," in *Proceedings of 2025 47th Annual International Conference of the IEEE Engineering in Medicine and Biology Society*, Thursday July 17th M1-2-8, Copenhagen, Denmark, July 2025.

Domestic Conferences in Japan

1. K. Mizuno, K. Hirashima, A. Shibata, S. Kodama, R. Sato, J. Okawa, K. Hori, and M. Higashimori, "Robotic mastication simulator based on tongue characteristics measured in human: Prototyping of tongue type pneumatic soft actuator," *SICE Domestic Conferences of the System Integration Division 2021*, pp. 2780–2784, Online, December 2021.
2. K. Mizuno, S. Kodama, R. Sato, J. Okawa, K. Hori, and M. Higashimori, "Design of tongue-type pneumatic soft actuator with arrayed chambers," *SICE Domestic*

Conferences of the System Integration Division 2022, 1A2-B05, Chiba, Japan, December 2022.

3. K. Mizuno, K. Yamada, H. Nakada, M. Thu Ya, K. Hori, and M. Higashimori, "Pneumatic soft actuator capable of visuo-tactile sensing -Application to *in vitro* tongue simulator-," *The Robotics and Mechatronics Conference 2025*, 2P1-Q01, Yamagata, Japan, June 2025.

Awards

1. SI2021 Excellent Presentation Award to K. Mizuno, (Domestic Conferences in Japan no. 1)

2. SICE System Integration Division Young Encouragement Award to K. Mizuno, (Domestic Conferences in Japan no. 1)

3. SI2022 Excellent Presentation Award to K. Mizuno, (Domestic Conferences in Japan no. 2)

4. SICE System Integration Division Research Encouragement Award to K. Mizuno, (Domestic Conferences in Japan no. 2)

5. Miura Award from the Japan Society of Mechanical Engineers to K. Mizuno, (Domestic Conferences in Japan no. 1–2)

6. Osaka University Engineering Society Award to K. Mizuno, (Domestic Conferences in Japan no. 1–2)

7. IEEE Kansai Section Student Paper Award to K. Mizuno, (Journal Papers no. 1)

Magazine Contribution

1. K. Mizuno and M. Higashimori, "Input design for tongue-type pneumatic soft actuators," *Hydraulics and Pneumatics (Japan Industrial Publishing)*, vol. 64, No. 3, pp. 16–20, March 2025.

Research Aids

1. JST Support for Pioneering Research Initiated by the Next Generation, Osaka University, 2023–2025.

2. JSPS Research Fellowships for Young Scientists (DC2), Japan Society for the Promotion of Science, 2025–2026.

Other Achievements

1. K. Mizuno, K. Iida, S. Nakamura, K. Toui, and T. Nishimoto, "Development of hands-free trolley for supporting harvest," *The Robotics and Mechatronics Conference 2018*, 1D5-12, Osaka, Japan, June 2018.

2. K. Mizuno, T. Kawasetsu, H. Ishihara, T. Horii, and M.Asada, "Prototyping of a child-type android hand with tactile sensors and bones," *The Robotics and Mechatronics Conference 2019*, 1P1-T07, Hiroshima, Japan, June 2019.

3. K. Mizuno, T. Kawasetsu, T. Horii, Y. Yano, and H. Ishihara, "Improvement of bone and surface structures of a child-type android hand with tactile sensors," *The Robotics and Mechatronics Conference 2020*, 2A2-N12, Online, May 2020.

4. H. Nakahara, K. Mizuno, T. Kawasetsu, and K. Hosoda, "Compliant mechanism for converting shear force into normal force for robot gripper application," *The 41th Annual Conference of the Robotics Society of Japan*, 2B3-04, Sendai, Japan, September 2023.

5. A. Ohta, K. Mizuno, M. Kochi, and M. Higashimori, "Development of a dummy object with pneumatic variable stiffness system," *SICE Domestic Conferences of the System Integration Division 2023*, pp. 3459–3461, Niigata, Japan, December 2023.

6. S. Kondo, K. Mizuno, A. Shibata, K. Higashi, and M. Higashimori, "In-hand manipulation by pneumatic soft gripper using the rolling trajectory variability," *The Robotics and Mechatronics Conference 2025*, 1A2-M06, Yamagata, Japan, June 2025.